UNIVERSITY OF COPENHAGEN
NIELS BOHR INSTITUTE

PhD thesis by

Sissal Vágsheyg Erenbjerg

Oceanography of the Faroe Shelf and Sundalagið Norður

A modeling approach

Winter view from Fiskaaling; looking towards Sundalagið Norður

Supervisors: Eigil Kaas
Knud Simonsen
Bogi Hansen

Submitted on: 31st of August 2021

Name of department:	Niels Bohr Institute, University of Copenhagen and Department of Fjord Oceanography at Fiskaaling
Author:	Sissal Vágsheyg Erenbjerg
Title and subtitle:	Oceanography of the Faroe Shelf and Sundalagið Norður; A modeling approach
Topic description:	Numerical modeling and oceanography of the Faroe shelf, fjord circulation and physical oceanography
Supervisors:	Eigil Kaas, University of Copenhagen Knud Simonsen, University of Faroe Islands Bogi Hansen, Faroe Marine Research Institute
Submitted on:	31. August 2021

This thesis is dedicated to:

Ásmundur Vágsheyg Johannesen

** 04 09 1930*

† 26 07 2019

Thank you for inspiring me…

ACKNOWLEDGEMENTS

I would like to thank everyone at Fiskaaling, for being great colleagues and friends. In particular everyone on the loft: Erna, Birgitta, Ása, Johannes, Tróndur and Tróndur. Thanks to Jóhanna for believing in me. Thanks to Gunnvør for helping me with many formalities as well as the application for the National Research Council to continue my research.

I would also like to thank my office mates in my 6 months stay in Copenhagen, Andrea and Rasmus, as well as my Norwegian colleagues at IMR, Lars, Ingrid and Anne, as well as my office mates in Bergen, Håvard and Kristin. In particular I would like to thank Jon Albretsen at IMR for close collaborations on the modeling part and for setting up and running the FarCoast.

I would also like to thank my three supervisors Eigil Kaas, Bogi Hansen and Knud Simonsen that have been outstanding in helping me through this PhD project, by guiding me, discussing with me and securing the funding. I would especially like to thank Bogi for kicking me through the last couple of months, I couldn´t have done this without you.

I really appreciate the support from the sponsors of the project, the National Research Council (grant no. 0445), MOWI, Fiskaaling, Bakkafrost and Statoil.

Finally, I am really excited to continue the work with ROMS and FarCoast from this thesis together with Eigil, Bogi and Jon and other collaborators in the future project: *High Performance Computing and FarCoast,* funded by the Faroese National Research Council (grant no. 0464) and Fiskaaling, so luckily this is really only the beginning…

ABSTRACT

This thesis presents a Regional Ocean Model System (ROMS) model called FarCoast covering the Faroe shelf. The model contains triply nested (800 m →160 m → 32 m) grids covering the entire shelf. The 32 m grid domain covers the northern part of Sundalagið, which has been the particular focus of this PhD thesis. The emphasis of this PhD on Sundalagið Norður, is partly due to the existence of earlier and available observations, but also due to the location of a fish farm in this sound, operated by one of the sponsors of this project, with a particular interest in this sound. The 800 m model is validated in two separate papers concluding that the FarCoast800 m model is an excellent driver for the Faroe shelf high resolution model domains. The FarCoast32 m model is also validated in the second paper against observations in Sundalagið Norður. Furthermore, the model has shown that there is an important contribution of long-period tides, both for monthly and the fortnightly tides. The Faroe Islands are located in an amphidromic region. This has been demonstrated earlier for the M_2 tide, but there are also amphidromes for S_2, N_2, K_1 and O_1. Furthermore, we have found evidence that Sundalagið Norður, behaves as a combination between a fjord and a strait, where the long-period tides determine the switch between the two states.

RESUMÉ

Denne PhD omhandler et studie baseret på ROMS, en regional tredimensionel havmodel, oprindelig sat op for den nordlige del af det Atlantiske ocean. En nested grid (800 m → 160 m → 32 m) version er sat op for den Færøske shelf for denne PhD. Den inderste version med 32 m opløsning dækker den nordlige del af et sund, kaldet Sundalagið Norður, som har været af særlig interesse for denne PhD. Årsagen er, at denne PhD til dels er støttet af en Færøsk fiskeopdrætsvirksomhed med fiskefarme i Sundalagið Norður, samtidig med at dette sund har været undersøgt tidligere, og der var tilgængelige observationer, som vi kunne sammenligne vores model resultater med; og derfor er 32 m model versionen af FarCoast valideret i vores paper 2. Vores model med 800 m opløsning er valideret mod observationer fra Havstovan og Landsverk. Konklusionen fra det første paper er, at FarCoast800m kan være driver for højopløste model domæner på den Færøske shelf. Det første paper fokuserer på strømfelter fra shelfen, samt temperatur og salinitet. De næste to papers har fokus på vigtigheden af tidevand på den Færøske shelf. Paper 2 belyser vigtigheden af tidevand for Sundalagið Norður, som er stærkt påvirket af, at Færøerne ligger i et amfidromisk område. At Færøerne ligger i et amfidromisk område har været etableret siden 1970´erne for M_2. Men at også de andre dominerende halvdaglige (S_2 og N_2) og daglige (K_1 og O_1) tidevands konstituenter er beliggende i et amfidromi er præsenteret i denne PhD. Desuden viser modelsimuleringerne at Sundalagið Norður opfører sig som en kombination mellem en fjord og et sund, hvor de langperiodiske (halvmånedlige og månedlige) tidevandskonstituenter bestemmer, hvordan nettoudskiftningen med sundet syd for og det åbne hav nord for sundet sker.

PREFACE

On a personal note: Putting ocean modeling in a global perspective

The oceans are covering the earth. For this reason we call our planet, the blue planet. As 71 % of the earth is covered by the oceans and all of these are connected and coupled, it is rather obvious that one of the main reasons for the possibility of life on our planet is the large coverage of the world oceans. For the last hundred years or so, human kind has, however, had to learn that the oceans do not present unlimited resources to us, and pollution at one place in the ocean can travel anywhere as the oceans are united and interconnected across the entire globe.

Thus, even though this PhD project is on a very small region in the North Atlantic, the Faroe Islands, one must also consider the bigger picture. We are influenced by the entire world and what we do here also influences the rest of the world. Hopefully with the most recent Intergovernmental Panel on Climate Change (IPCC[1]) report we have all come to realize, that humankind is indeed changing the oceans. This calls for a better management of the oceans. Where we are at in the North Atlantic Ocean, the sea surface temperature has risen 1 °C, the sea level has risen 14 cm and the pH of the ocean has decreased by 0.1 (with a large spatial variation) only since 1890 (EASAC, 2021[2]). Future worst-case (business as usual) scenarios, which include high greenhouse gas emission, will result in additional increases of the sea surface temperature and sea level. Furthermore, we can expect that the Atlantic Meridional Ocean Circulation (AMOC) will weaken between 10 and 30 % during this century. A total collapse of the AMOC is not considered likely in this century, but is a possibility for high emission scenarios according to the latest IPCC report. Such a collapse would have severe consequences for the Faroese region, as our mild climate is dependent on the warm upper branch of the AMOC flowing past us on its way toward the Arctic.

One larger scope as well is the connection between all the different sciences. The ocean is complex and the ocean sciences combine the classical sciences of physics, biology, chemistry and geology. Furthermore, applied mathematics and computational physics can help us to connect the dots, helping us to understand the necessities for having a sustainable blue economy. Maybe reaching the ambition of a climate neutral Europe by year 2050 is possible, however, it will still be necessary to restore and rebuild the marine environment in the North Atlantic Ocean.

---

[1] *IPCC, 2021: Climate Change 2021, The Physical Science Basis. Contribution of Working Group I to the Sixth Assessment Report of the Intergovernmental Panel on Climate Change,Cambridge University Press. In Press.*

[2] EASAC, *2021: A sea of change: Europe's future in the Atlantic realm EASAC policy report 42 June 2021,The Clyvedon Press Ltd, Cardiff, United Kingdom, ISBN: 978-3-8047-4262-8*

This means that if we have any wish to continue to have aquaculture in the Faroe Islands, we need to sustain a good and healthy environment in our fjords. Furthermore, the Faroese aquaculture companies need to be able to adapt as climate will change the ocean on the Faroe Shelf and the fjords currently housing the fish farms. How the combination of changes in sea-temperature, salinity and currents as well as in the atmosphere will influence the Faroese region is best learned by using numerical ocean models. Hopefully, this PhD has contributed a little bit towards that goal.

Sissal Vágsheyg Erenbjerg

Tórshavn, Faroe Islands
August 2021

CONTENT

1 Introduction

1.1 Motivation

The main motivation for this PhD thesis was to provide a better understanding of the constraints on Faroese aquaculture by the physical environment. Prior to the COVID-19 pandemic, the demand of farmed fish for food was increasing globally. The world population is in need of food that is healthy such as fish. Furthermore the pressure on food production sectors to reduce methane and carbon dioxide emissions per produced kilo protein is also favoring fish consumption over other protein products.

This is an important perspective for Faroese economy, which to a large extent is dominated by fish export. Until the early part of this century, this export was mainly based on fisheries on the Faroe shelf and in Faroese waters but since then the amount of farmed fish, especially salmon has increased (Figure 1.1) to approximately 20% of the Faroese Gross National Product (GNP).

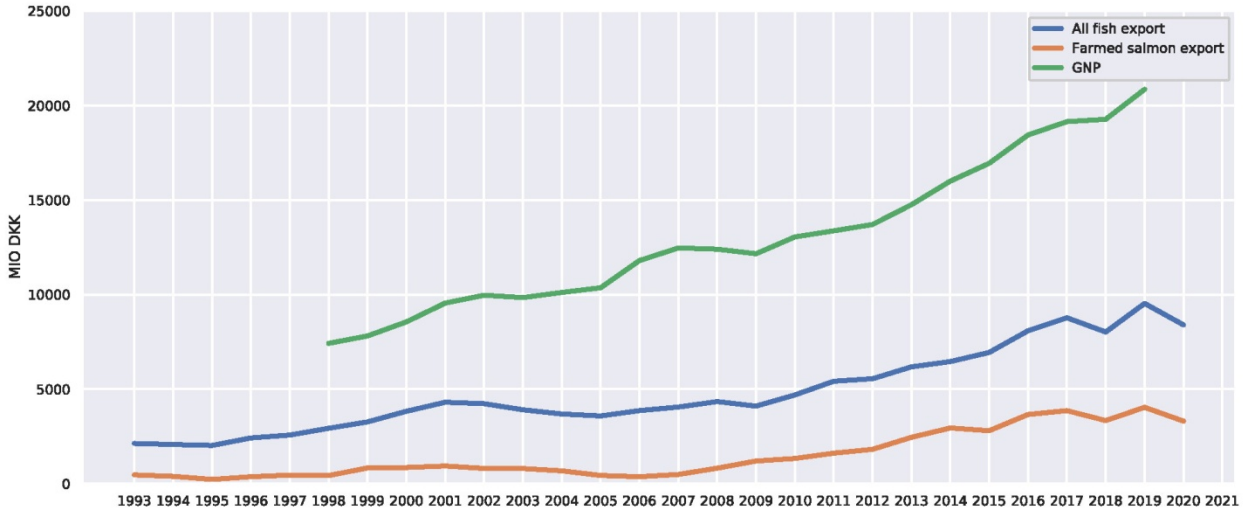

Figure 1.1. *Green: Faroese Gross National Product (GNP) from 1998 to 2019, Blue: Total Faroese fish export from 1993 to 2020, Orange: Value of exported salmon from 1993 to 2020. All values in million Danish Kroner (MIO DKK). Source: Hagstova Føroya.*

Fish farming started in the Faroe Islands more than 50 years ago (Jacobsen, 2020) and both trout and salmon have been farmed. In recent years, salmon has dominated totally (Figure 1.2). Due to the limited landmass on the Faroe Islands and rather complex landscape (high mountains), land-based (fish)-farming and agriculture in general will be limited. This means that Faroese fish farming is dependent on the availability of marine areas.

The production of farmed salmon increased rapidly from 1996 to 2012 but from 2012 the increase in production has slowed down (Figure 1.2), because many of the fjords are reaching their maximum capacities. This has stimulated attempts to increase the production by moving towards more open ocean and using large smolts to reduce the time in ocean water.

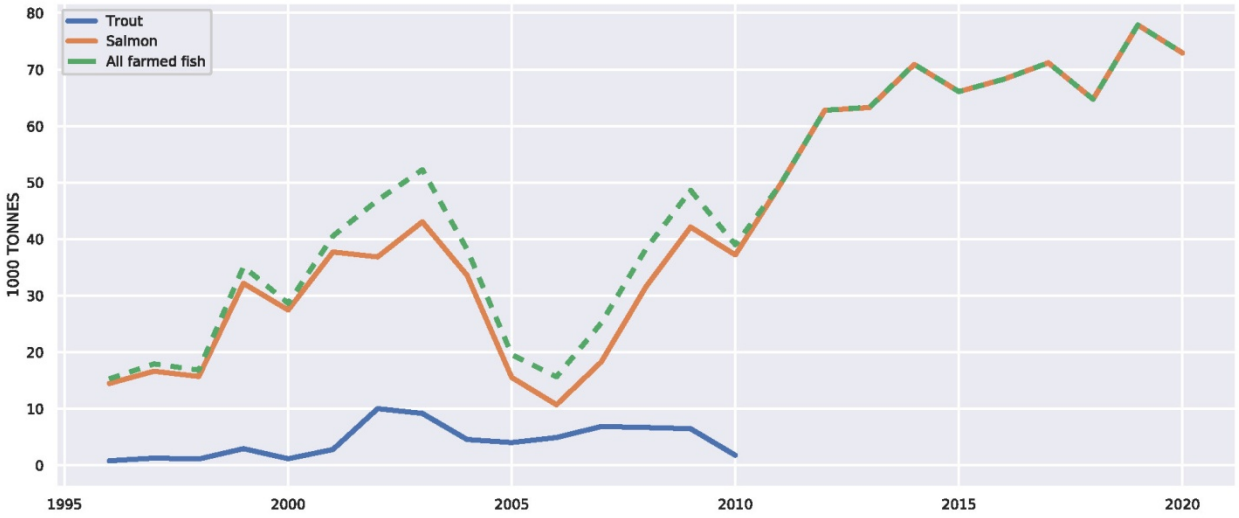

Figure 1.2. *Export of farmed salmon (orange line) and trout (blue line) from 1996 to 2020. The green broken line is the sum of the two. Source: Hagstova Føroya.*

With this in mind, a better understanding of the constraints that the physical environment has on fish farming potential is imperative. This is the case for the fjords with established farms where mixing and exchange processes may limit the carrying capacity, but also for the plans to go into more open and less protected areas. In both cases, detailed knowledge of currents and hydrodynamics are important. This was the motivation for this PhD project, which had the aim to develop a numerical three dimensional ocean model system of the Faroese fjords and shelf.

1.2 Project objectives and implementation

The main focus of the project has been on the largest fjord system in the Faroes, "Sundalagið", which is a narrow strait between the two main islands in the archipelago Streymoy and Eysturoy (Figure 4.6b). In particular the northern part of Sundalagið, "Sundalagið Norður", was studied. Sundalagið Norður has shallow sills in both ends with deeper water in-between (Figure 4.9). To study this system, the aim was to implement a high-resolution numerical 3D-model system, validate the simulations against available observations and analyze the results.

It was decided to use the ROMS (Regional Ocean Model System) model with a Norwegian adaption of the setup. On the boundaries the library from Lien et al. (2013) was used as forcing. This library is referred to here, as ROMS4KM, which has a horizontal resolution of 4 km × 4 km covering the area shown in Figure 4.1. To reach the high resolution required, it was therefore decided to implement a triply-nested system (800 m → 160 m → 32 m) (Figure 1.3) with horizontal resolution increasing by a factor of five for each nesting.

As a PhD student, I have been enrolled at the University of Copenhagen, but the main workplace has been at the Faroese Aquaculture Research Station "Fiskaaling" in the Faroe Islands. However, due to limited access to modeling resources the model system was run at the Institute of Marine Research (IMR) in Bergen. The logistical problems associated with this have made some of the original intentions unrealistic and the main results of the project are the three manuscripts listed at the end of this thesis:

- **Paper I:** *Erenbjerg, S. V., Albretsen, J., Simonsen, K., Sandvik, A. D., and Kaas, E. (2020): A step towards high resolution modeling of the central Faroe shelf circulation by FarCoast800. Regional Studies in Marine Science, 40, 101475. https://doi.org/https://doi.org/10.1016/j.rsma.2020.101475.* In this paper the setup of FarCoast800 (Figure 1.3) is presented as well as validated towards observations. We find a high correlation between simulated sea surface temperature and observations at three coastal stations, but the simulated salinity has a bias around 0.1 psu. Furthermore this paper contains a detailed hydrographic area description of the Faroe shelf. Among the results, this paper presents a description of how water enters the Faroe shelf from the larger ocean basins. For this thesis, an important conclusion from this paper is that FarCoast800 can drive a high-resolution nested area on the Faroe shelf.

- **Paper II:** *Erenbjerg, S. V., Albretsen, J., Simonsen, K., Olsen, E., Kaas, E., and Hansen, B. (2021): A tidally driven fjord-like strait close to an amphidromic region. Ocean Sci. Discuss., 1-23, https://doi.org/10.5194/os-2021-23, in review, Aug 2021*. In this paper the model setup FarCoast32 (Figure 1.3) is validated towards observations. The paper

describes the exchange of water through the strait of Sundalagið in the central part of the Faroese archipelago where this body of water according to the model shifts between behaving like a strait and a fjord on a fortnightly cycle. We conclude that this fortnightly variation is an effect of the long-period tides alongside the location of the Faroe Islands within an amphidromic region for the dominant semidiurnal constituents.

- **Paper III:** [Manuscript in preparation]: *Erenbjerg, S. V., Hansen, B. and others.: The effects of tidal mixing on stratification over the Faroe shelf*. This manuscript is in a fairly early stage of preparation. It will combine results from the FC800m simulation with existing observational data to analyze the effects of variable tidal mixing on stratification over the Faroe shelf, which is a parameter of critical importance for primary production on the shelf.

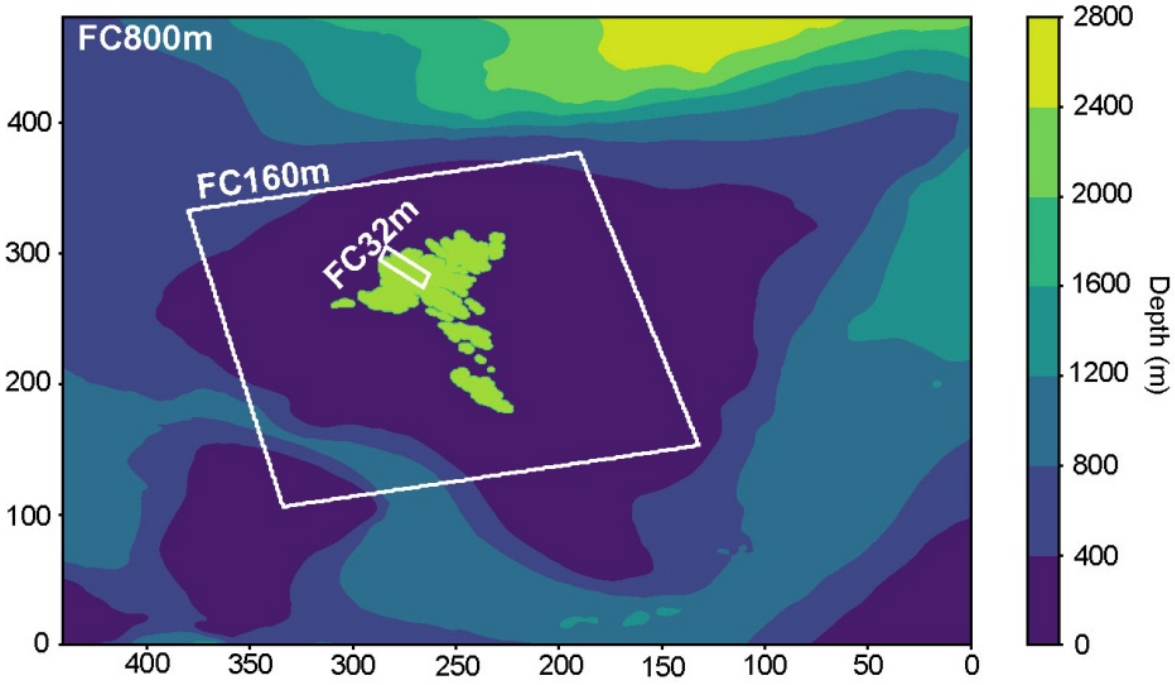

Figure 1.3. *The three model domains implemented in this project with bottom topography as the colored background, the FarCoast (FC) 800 m, 160 m, and 32 m. The FC800m model is forced along its four open boundaries by the ROMS4KM (4 km × 4 km) hindcast archive (Lien et al., 2013).*

2 Background

2.1 The fundamental equations of physical oceanography

From a mathematical point of view, the basis of physical oceanography is defined by a set of general equations, which are derived from fundamental laws of classical mechanics (Cushman-Roisin & Beckers, 2011). The first of these is based on the conservation of mass:

$$\frac{\partial \rho}{\partial t} + \frac{\partial (\rho u)}{\partial x} + \frac{\partial (\rho v)}{\partial y} + \frac{\partial (\rho w)}{\partial z} = 0 \quad (2.1)$$

where ρ is the density and u, v, and w are the three components of the velocity. For an incompressible fluid, this "continuity equation" reduces to:

$$\frac{\partial u}{\partial x} + \frac{\partial v}{\partial y} + \frac{\partial w}{\partial z} = 0 \quad (2.2)$$

The equations of motion are mainly based on Newtons 2nd law in a rotating system. With the Boussinesq approximation, the equations for the horizontal momentum balance are:

$$\frac{\partial u}{\partial t} + u\frac{\partial u}{\partial x} + v\frac{\partial u}{\partial y} + w\frac{\partial u}{\partial z} - fv = -\frac{1}{\rho_0}\frac{\partial p}{\partial x} + \vartheta\frac{\partial^2 u}{\partial x^2} + \vartheta\frac{\partial^2 u}{\partial y^2} + \vartheta\frac{\partial^2 u}{\partial z^2} \quad (2.3)$$

and

$$\frac{\partial v}{\partial t} + u\frac{\partial v}{\partial x} + v\frac{\partial v}{\partial y} + w\frac{\partial v}{\partial z} + fu = -\frac{1}{\rho_0}\frac{\partial p}{\partial y} + \vartheta\frac{\partial^2 v}{\partial x^2} + \vartheta\frac{\partial^2 v}{\partial y^2} + \vartheta\frac{\partial^2 v}{\partial z^2} \quad (2.4)$$

where f is the Coriolis parameter, p is the pressure and ϑ is the kinematic viscosity. For the problems studied in this work, the hydrostatic approximation can be assumed so that the equation for vertical momentum balance reduces to:

$$0 = -\frac{1}{\rho_0}\frac{\partial p}{\partial z} - \frac{g\rho}{\rho_0} \quad (2.5)$$

For a conservative property the concentration, Φ, (per unit mass) changes according to:

$$\frac{\partial(\rho\Phi)}{\partial t}+\frac{\partial(\rho\Phi u)}{\partial x}+\frac{\partial(\rho\Phi v)}{\partial y}+\frac{\partial(\rho\Phi w)}{\partial w}=-\left(\frac{\partial F_x}{\partial x}+\frac{\partial F_y}{\partial y}+\frac{\partial F_w}{\partial z}\right) \quad (2.6)$$

where the vector (F_x, F_y, F_z) represents the diffusion flux of the property, generally assumed to be proportional to the gradient (Fickian diffusion). For practical cases, other information will usually be needed, such as the equation of state, boundary conditions, external forcing, etc.

2.2 Tides in the ocean

As the term tide, can be used in different ways, we here take on the specific scientific term tide as in Pugh and Woodworth (2014), where tide means only the regular periodic variations of the sea level. Associated with sea level variations, there are the periodic variations of velocity, which are termed tidal currents. These motions are created from the gravitational force from the Moon and the Sun combined with the centrifugal force experienced on Earth as it revolves about the shared center of mass. If the Earth was covered entirely by a layer of ocean, which could respond instantaneously to gravitational attraction from the moon and sun, it would have two tidal bulges, with two maxima and two minima, on the line between the moon and earth centers. As the Earth is rotating this would result in two tides a day, the semidiurnal tides.

The tidal force and this “equilibrium tide” can be calculated very accurately from Newtonian mechanics. However, as the Earth is not covered entirely by water the tides are also controlled by coastal steering and water depth, which limits the speed with which a barotropic wave can travel. In addition, bottom friction and the Coriolis force also distort the motion from the ideal equilibrium tide.

In spite of this distortion, both sea level and current velocity in most places do include periodic components with the same periods as the forcing and the equilibrium tide, but with different amplitudes and phase-lags. Each of these periodic motions is usually termed a “constituent” and they are generally categorized as three different types: semidiurnal, diurnal and long-period, the last of which includes fortnightly, monthly and even longer periods. Each constituent is denoted by a capital letter and an index showing the type or by more complex combinations of letters and numbers. Some of the most important constituents are listed in Table 2.1.

Semidiurnal tides generally dominate in most places and their amplitudes vary in a fortnightly spring-neap cycle. Maximum in the spring-neap tidal cycles is usually seen a day or two after new and full moon. Minima are at first and last quarter when the tidal forces from the Sun and the Moon are opposing each other. From a mathematical point of view, these variations

may be seen as the interference between different semidiurnal constituents, especially between M_2 and S_2.

One of the departures from the equilibrium tide is the appearance of “amphidromic” regions. These are regions where the amplitudes of one or more tidal constituents for sea level more or less vanish at the same time as the phase-lags exhibit very high spatial variation. This is the case for the central parts Faroe shelf where sea level in Tórshavn has been found to have very small amplitudes for several semidiurnal components (Hansen, 1978). The small amplitudes for sea level do not imply that the tidal currents associated with the same constituents are small. On the contrary, the high spatial variations in amplitude and phase of sea level close to an amphidromic region may generate strong tidal currents as is the case on the Faroe shelf (Hansen, 2000).

Table 2.1. *Some principal tidal constituents.*

Name	Symbol	Period	type
Principal lunar	M_2	12.42 hours	Semidiurnal
Principal solar	S_2	12.00 hours	Semidiurnal
Larger lunar elliptic	N_2	12.66 hours	Semidiurnal
Luni-solar	K_2	11.97 hours	Semidiurnal
Luni-solar	K_1	23.93 hours	Diurnal
Principal lunar	O_1	25.82 hours	Diurnal
Principal solar	P_1	24.07 hours	Diurnal
Lunar Fortnightly	Mf	13.66 days	Fortnightly
Luni-solar Fortnightly	MSf	14.78 days	Fortnightly
Lunar Monthly	Mm	27.55 days	Monthly
Luni-solar Monthly	MSm	31,81 days	Monthly

2.2.1 Harmonic analysis of tides

The basic assumption in Harmonic analysis is that any tidal signal can be represented as a finite number of harmonic terms representing different constituents with frequencies that are derived

from the tidal forcing or as combinations of these. If $h(t)$ represents the height of the sea surface at a specific location at time t, then this implies that we can write:

$$h(t) = \sum_{n=1}^{N} H_n \cos(\omega_n t + \varphi_n - g_n) + R(t) \qquad (2.7)$$

where $\omega_{n,}$ is the angular frequency of the nth constituent. $\varphi_{n,}$ is the phase of this constituent at time, $t = 0$, at the location of Greenwich. $R(t)$ represents the non-tidal component of the sea level. The two values H_n and g_n for each constituent are assumed to be constant. If the actual tide was in phase with the forcing and the equilibrium tide for constituent n, then g_n would be zero on the longitude of Greenwich and this parameter is therefore termed the "Greenwich phase-lag". Similar expressions may be used for each of the two velocity components of the tidal current.

The constituents generally used were defined by A. T. Doodson (Doodson & Lamb, 1921). Doodson published his paper on the harmonic development on the tide-generating potential in 1921. This paper revealed how all tidal constituents have frequencies that can be seen as linear combinations of six different frequencies. These are lunar mean time and five astronomical variables that represent the positions of the Moon and the Sun at any time:

$$\omega_n = i_a\omega_1 + i_b\omega_2 + i_c\omega_3 + i_d\omega_4 + i_e\omega_5 + i_f\omega_6 \qquad (2.8)$$

Each constituent is defined by its "Doodson coefficients ($i_a, i_b, \ldots$) from which ω_n and φ_n may be calculated. In principle, it should be possible to calculate H_n and g_n from the equations in Sect. 2.1 with knowledge of the tidal forcing and bottom topography. In practice, they are usually derived from observations. Various methods have been developed for this purpose (e.g., Godin (1972)). In this project, the U_TIDE software package has been used. This is the Python adaption of the T_TIDE Matlab version developed by Pawlowicz from Foreman's initial analysis tool (Pawlowicz et al., 2002) (Foreman & Henry, 1989).

2.3 Fundamentals of fjord oceanography

A fjord is typically described as a long and narrow inlet caused by glacial carving during one of the previous ice-ages. Thus most fjords are located in high-latitude and mountainous coastal areas (Inall & Gillibrand, 2010). Similar to other estuaries, a fjord is a semi-enclosed body of water, with a free connection to the open ocean, where ocean water is measurably diluted by fresh water. Several studies of specific fjords and their oceanography exist in the literature (e.g., Inall & Gillibrand (2010); Stigebrandt (1981); Jackson & Straneo (2016); Arneborg (2004)) and

also a number of more general descriptions of fjord oceanography (e.g., Farmer & Freeland (1983)).

General for all estuaries is that fresh water from rivers meets ocean water on the way into the ocean. In the estuary the fresh water mixes into the saltier ocean water on its way to the open ocean. For a fjord the law of mass or volume conservation is maintained though a rather simple balance:

$$V_i + R + AP = V_o + AE \qquad (2.10)$$

where A is the area and P, E and R are the freshwater input/output as precipitation, evaporation and river runoff, respectively. V_i and V_o are the volume transports into and out of the fjord, respectively. Similarly, conservation of salt leads to a relationship between the salinity of the inflowing (ocean) water, S_i, and the outflowing (brackish) water, S_o:

$$V_i \cdot S_i = V_o \cdot S_o \qquad (2.11)$$

The general, so-called “estuarine”, circulation of a fjord (Figure 2.1) is that there will be a brackish layer in the surface with an outward flow and a flow of ocean water in the opposite direction below. Since the brackish water is less dense than the ocean water below it, a pycnocline will generally separate the two layers. In narrow fjords, variations of stratification induced by exchange of water and mixing processes can often be handled by regarding the fjord as a simple 1D (vertical) system.

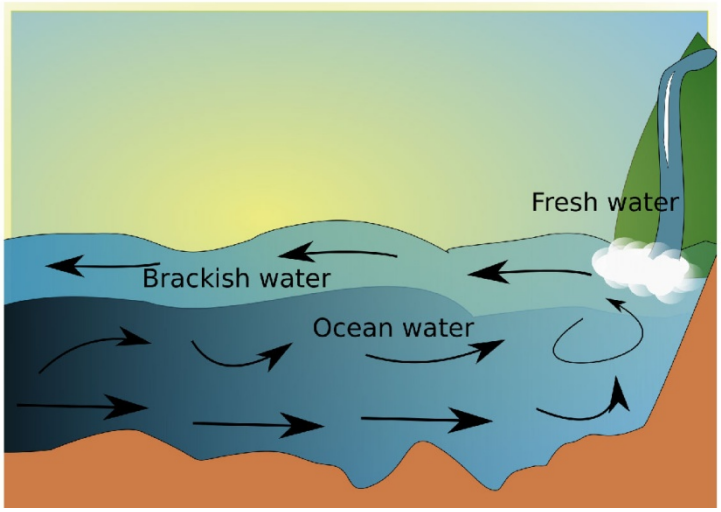

Figure 2.1. *The general, “estuarine”, circulation in a fjord. Drawn in InkScape.svg.*

A general feature of fjord dynamics is the dependence on the physical limitations, due to topographic constraints such as sills and narrowing near the outlet (Inall & Gillibrand, 2010). These constraints at the entrance reduce the cross-sectional area through which water can flow, thus inducing a local acceleration of the flow. In a sill fjord, a stagnant bottom layer can develop during spring and summer. In winter the storms and intense wind mixing will prevent this from occurring, but the warming of the ocean water outside the fjord during spring may reduce the density of the ocean water. Then the ocean water is less dense than the bottom water inside the fjord. This can make the bottom water in the fjord stagnant for long periods during which biological activity may reduce the oxygen concentration substantially (Figure 2.2).

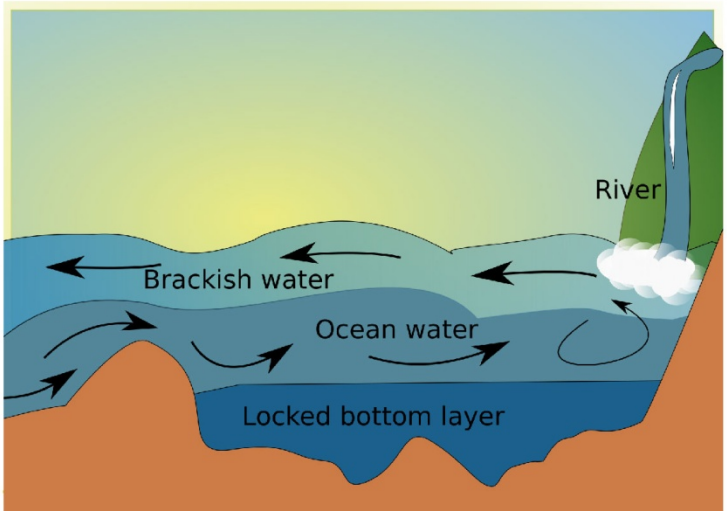

Figure 2.2. *Typical circulation in a sill fjord during periods with a locked (stagnant) bottom layer. Drawn in InkScape.svg.*

The flows in a fjord are in general forced from both inside and outside of the fjord. In addition to freshwater (estuarine) forcing, wind stress acting on the surface layer can generate flow as well as induce vertical mixing. Tidal sea level variations outside a fjord will also generate periodic variations in the net transport into and out of the fjord.

2.4 The Faroe shelf and fjords

The water masses around the Faroe Islands have different origins and properties, but almost all the water on the shelf originally derives from the relatively warm and saline flows of Atlantic water, especially Modified North Atlantic Water (MNAW) (Figure 2.3), although it may have been modified by local processes.

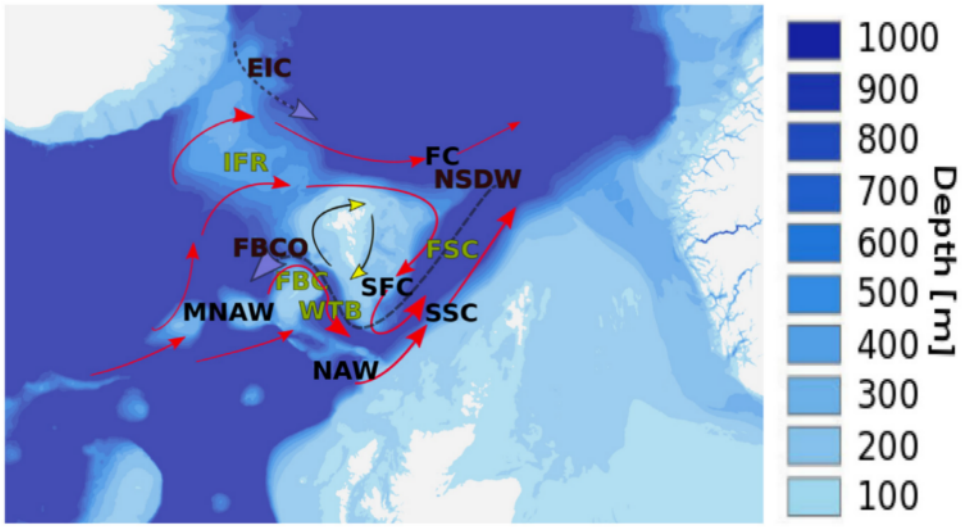

Figure 2.3. *Bathymetry and main flow pathways for the waters surrounding the Faroe Islands. Continuous arrows indicate flow of Modified North Atlantic Water (MNAW) and North Atlantic Water (NAW) in the upper layers (red), the cold Norwegian Seas Deep Water (NSDW) (purple), the colder and fresh East Icelandic Current (EIC) (purple) and the clockwise residual current on the shelf (yellow). Copied from Paper I in this thesis.*

The Faroe shelf is often defined as the region with bottom depths less than 200 m (Figure 2.4). Due to the strong tidal currents, the inner parts of the shelf are strongly mixed and the water column is often homogeneous from surface to bottom (Larsen et al., 2008).

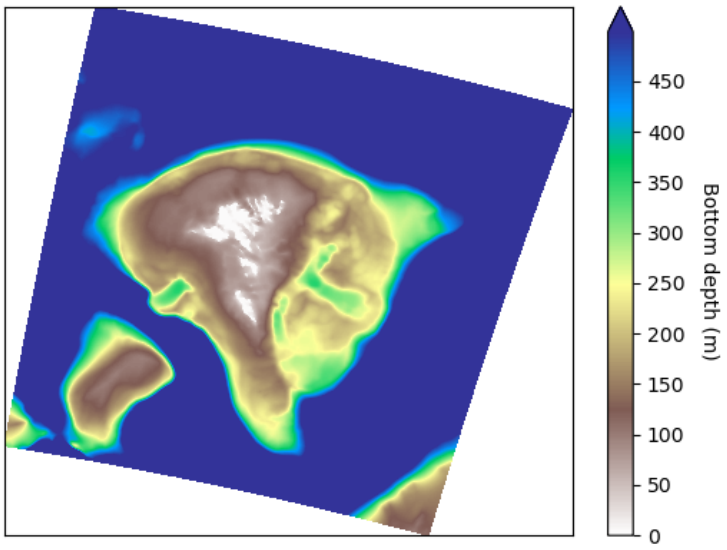

Figure 2.4. *Bottom topography of the Faroe shelf and surrounding areas. All areas deeper than 500 m are dark blue. Based on the bottom topography of the FC800m model discussed in Paper I.*

In winter, atmospheric cooling reduces the water temperature more efficiently in the shallow parts and a front may be generated, which separates the innermost parts of the shelf from the surrounding water masses (Figure 2.5). Due to the strong mixing, the water inside this front is often considered as one homogeneous water mass (Larsen et al., 2009).

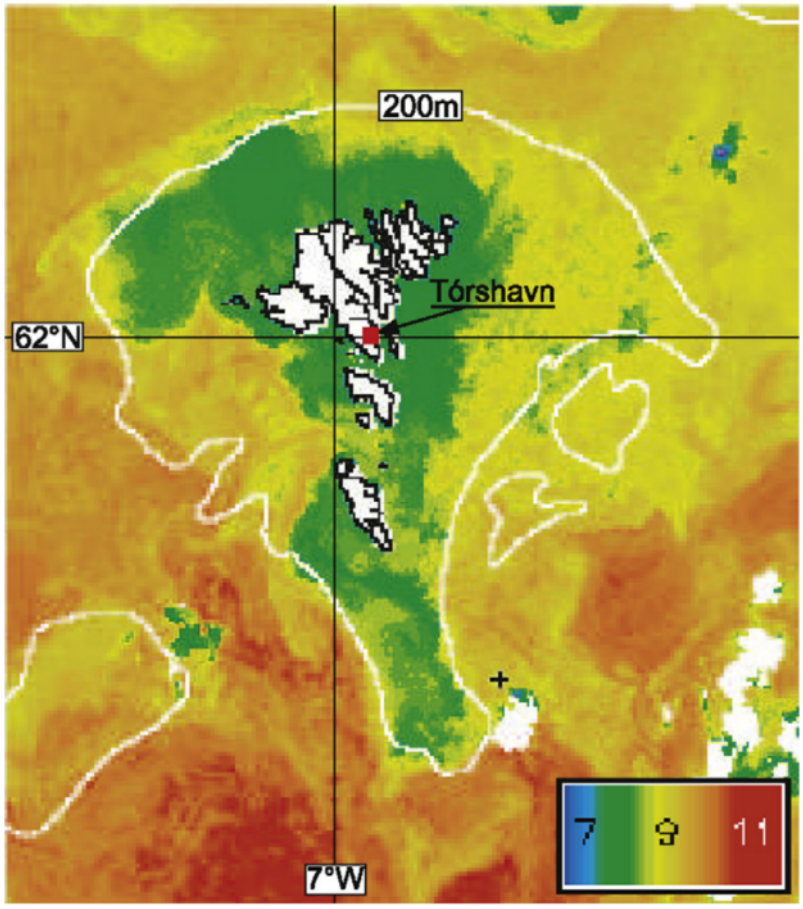

Figure 2.5. *Sea surface temperature around the Faroe Islands on 18th of April in 2003 from infrared satellite imagery using the scale shown in the lower right corner (°C). Adapted from Larsen et al.(2008).*

The most thorough studies of Faroese fjords are from the late 1980's (Hansen, 1990). The general picture from these Faroese fjord investigations is that they follow the typical pattern of other fjords with a brackish upper layer, where fresh water enters from rivers and a lower layer that is denser and more saline as illustrated in the left panel of Figure 2.6 by an example from the largest Faroese fjord: "Skálafjørður".

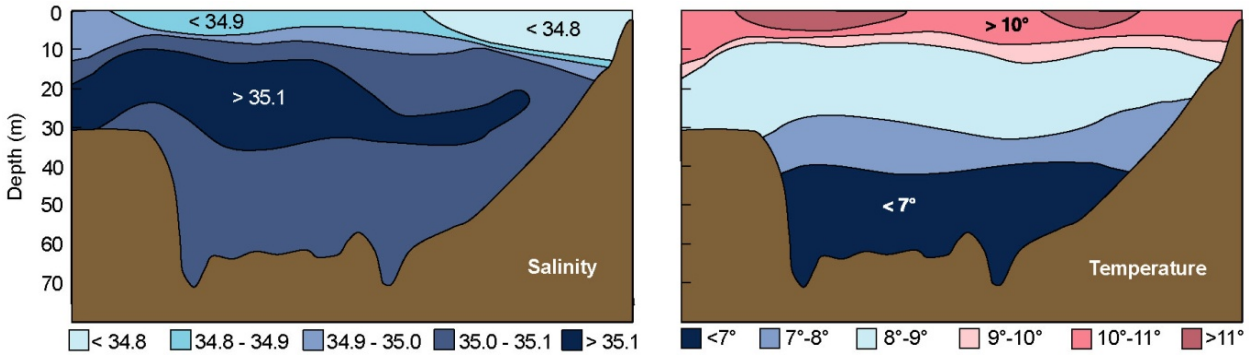

Figure 2.6. *Salinity (left) and temperature (right) on a section through Skálafjørð on 30 June 1988 based on CTD observations. Adapted from Hansen (2000).*

Several observations in the fjord reveal that the common case is that the brackish water is well mixed prior to leaving the fjord. During summer, the brackish layer is often heated as illustrated in the right panel of Figure 2.6, which increases the density difference between the two layers. This figure also demonstrates that this sill fjord in summer often will develop a middle layer and the lowest layer will become a locked bottom layer, not being ventilated. This reduces the amount of oxygen as there is little mixing with the upper layers during long periods (Figure 2.7). The oxygen loss may be enhanced if organic pollution from activities such as aquaculture enters the fjord.

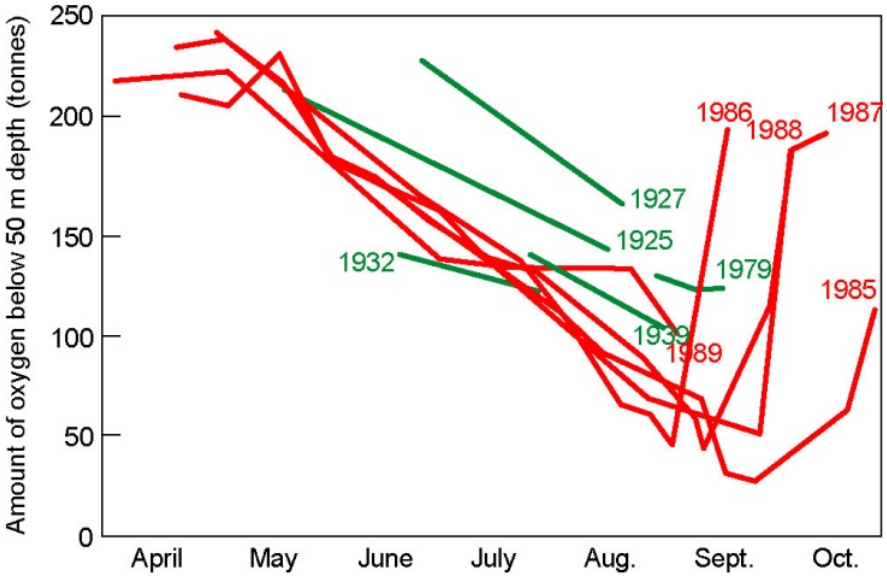

Figure 2.7. *The seasonal development of the amount of oxygen below 50 m depth in Skálafjørður for different years based on measurements. For years after 1984 (red), the curves are typically based on several measurements through the season. For years before 1984 (green), each curve is usually based on measurements at only two occasions. Adapted from Hansen (2000).*

3 Numerical ocean models

3.1 General description of ocean models

There is a basic distinction between Eulerian and Lagrangian models. The Eulerian grid is fixed in space and the equations are solved at each interception of the grid corners. The Lagrangian time step follows an individual parcel on a path trajectory. In this thesis, only Eulerian models have been used.

The most basic assumption for formulating a three dimensional Eulerian ocean model is that the ocean can be divided vertically into layers (layered model). Several different methods of vertical layering can be implemented:

- **z-coordinates:** Each layer has a constant depth. The surface layer can be free or can be a rigid lid.
- **σ-coordinates:** The layers follow the topography of the bottom.
- **Isopycnal coordinates:** The layers follow density (isopycnal) surfaces.
- **Hybrid-coordinates:** The hybrid-coordinates are hybrids of two or all of the formulations above using z-coordinates to describe the surface layers, isopycnal coordinates for the middle layers and σ-coordinates for the bottom layers.
- **S-coordinates:** The S coordinates or the stretched coordinates are a combined σ-coordinate and z-coordinate model where the surface layers are locked to a certain depth and the bottom layers follow the topography.

For the horizontal coordinates, some model formulation use unstructured grid formulation, but most models use an orthogonal regular grid formulation similar to the presentation in Figure 3.1. Here the equations should be solved at each cross-point (e.g., red dot labeled U_{33} in the figure) or at the centers (green and blue dots). The distances Δx and Δy determine the horizontal resolution.

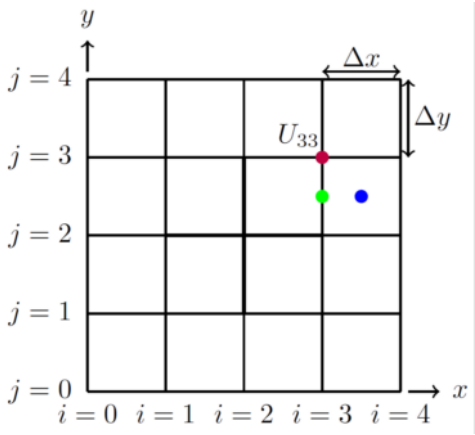

Figure 3.1. *General formulation of the regular horizontal grid. Made with TikZ LaTeX.*

Usually, the system for how and where to solve the numerical equations in the horizontal grid is defined through the Arakawa grid formulation (Figure 3.2) by Arakawa & Lamb (1977). The most common use is of the Arakawa C grid type. Where (i, j) is located at the red dot in Figure 3.1, q in the blue dot and u at the green dot. Arakawa C is a staggered type grid formulation.

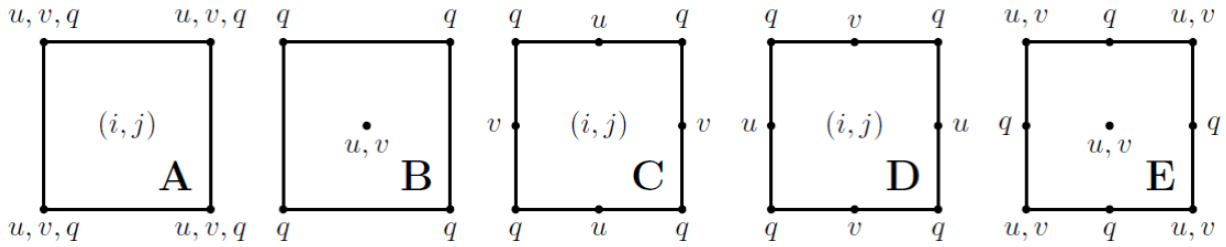

Figure 3.2. *The Arakawa grid formulations, from Arakawa and Lamb (1977), identified by letters from A to E. The letters "u" and "v" indicate the locations for calculating the horizontal velocity components while "q" indicates locations for calculating other parameters, e.g., temperature. Made with TikZ LaTeX.*

3.2 Numerical formulations and time stepping schemes

When considering time step schemes in a numerical model, some restrictions must be considered. One can start by considering the difference between the explicit and the implicit time step. The explicit time step considers calculations in the future from one starting point, which means that the calculations are only dependent on the past and the present. For an implicit scheme, the solutions are dependent on a future time step as well. This method demands some extra calculations as the future time steps must be calculated twice. This is the reason that several

models implement the semi-implicit time step as this is both easier to implement as well as providing faster computations.

The basic task of an ocean model is to solve the differential equations in Sect. 2.1 together with boundary conditions and other constraints for the specific case. The numerical method for solving differential equations is based on the Taylor Series approximation and the finite difference method, which may be grouped into Forwards, Backwards, and Centered finite difference methods. The simplest time step is often considered the forward Euler, which only uses the present time step, and thus is often considered for the very first time step. However, this method often demands very small time steps and is usually not used for the general numerical kernel of ocean models.

The numerical formulation in any numerical model is determined by different parameters where the subtle balance between accuracy, convergence, consistency, and stability must be considered. Especially the time step Δt and the spatial step Δx should fulfill the Courant-Friedrichs-Lewy (CFL) criterion. A further stability criterion is the von Neumann stability criterion (Durran, 2013).

3.3 ROMS

ROMS is the abbreviated name for the "Regional Ocean Model System". ROMS is a primitive equation solving, split-explicit, free-surface, topography-following-coordinate ocean model (http://myroms.org, Shchepetkin & McWilliams, (2005); Haidvogel et al., (2008)). This model is developed on the bases of the code from numerical models such as SPEM and SCRUM (Shchepetkin & McWilliams, 2005). The ROMS code has been rewritten, however, by Alexander Shchepetkin, Hernan Arango and John Warner along with many other contributors.

The general purpose of the ROMS model is to model regional and basin scale ocean processes. This is regarded as an optimal choice for modeling the hydrodynamics around the Faroe Islands, which is surrounded by deep ocean at all four open boundaries and has a shelf that may be considered as shallow water along the coastal lines.

ROMS is based on the Boussinesq approximated shallow water equations, as mentioned in section 2.1, and comes with a variety of options and with S-coordinates in the vertical. The vertical equation also has the hydrostatic assumption. The advection can be solved by many different numerical schemes.

3.4 The models implemented in this thesis

The first model implemented in this thesis is the FarCoast 800 m (FC800m) model, which has a horizontal grid resolution of 800 m (Figure 1.3). The setup used for this model is an adaptation

from the NorKyst800 model, a setup covering the entire Norwegian coast with 800 m resolution (Asplin et al., 2020). We applied input from the same large-scale model (Lien et al., 2013) as the Norwegian counterpart and a similar setup, but simulated one year, 2013, only. The advantage of this setup is that it uses increased resolution in the upper 50 meters. The general setup for FarCoast is that is uses 34 vertical S layers. These are defined through a stretching parameter defined in the setup (Hedstrøm, 2018).

The numerical scheme used for the horizontal advection is a third order upstream scheme and vertical mixing is parameterized with the GLS (Generic Length Scale) method (Umlauf & Burchard, 2003). The advantage of using the GLS method is that it seems to produce realistic values in areas that are dominated by tides, such as coastal and shelf areas. The vertical advection is presented as a split explicit mode suggested by Marchesiello et al. (2009), reducing spuriously developed currents at steep bathymetry.

On the boundaries of the FC800m model, the setup is forced by a ROMS4KM library from the Institute of Marine Research in Bergen (4 km × 4 km horizontal resolution (Lien et al., 2013)). The ROMS4KM is used on the boundaries, by applying a nudging relaxation scheme as in Marchesiello et al. (2001), This is to reduce the drift in sea surface salinity observed in the Norwegian Sea. For the ROMS4KM library used on the boundary, the setup is similar to the one described by Lien et al. (2013), except that the boundary conditions are based on climatology for temperature and salinity and not from SODA (Simple Ocean Data Assimilation).

The second nesting of the FarCoast model setup is the FC160m model (Figure 1.3), which has a resolution of 160 m × 160 m in the horizontal with 1000 grid points in one direction and 800 grid points in the other. This model is run for five months in 2013 and its main purpose was to be used as an intermediate parent model for the ultra-high-resolution (32 m) setup defining the FC32m model. The details and results from the 160 m model will not be discussed in any detail in the thesis.

The 32 m model was implemented to study the main focus of this thesis, the strait “Sundalagið Norður”. FC32m has 682 grid points in the direction along the strait and 187 points across it. It covers an area that includes the strait and the areas just north and south of it.

In addition to the constraints provided by the nesting, each of the three models is run with realistic atmospheric forcing. For the different setups quite distinct time steps are used in order to not violate the CFL criterion, but only hourly outputs are saved to the individual output files.

The atmospheric forcing for the model setup of FarCoast was obtained from simulations with the Weather Research and Forecasting (WRF) model (WRF, http: //www.wrf-model.org/). The model was configured with horizontal grid resolutions of 9-3-1 km, where the 1 km resolution domain covered the area of interest and was used as forcing for the ocean model. For further details on the configuration of the model see Myksvoll et al. (2012).

4 Results

As indicated by the title of the thesis, the main aim of this PhD has been to set up a three-dimensional ocean model system for the Faroese shelf and fjords. However, it was quickly realized, that any high resolved model only has relevance if the outer model is validated and acceptable. Then the capability of running a nested version with higher resolution can be considered. Most of the work has therefore been to set up, run, and validate the three models in this system, although some more general scientific results have been obtained as well. The ultimate aim was to implement a very high-resolution model that could simulate exchange and other processes in the small-scale fjords and sounds of the Faroe Islands, especially the key area: "Sundalagið Norður".

To realize this, it was decided to implement a model system consisting of three models, successively nested within a Norwegian 4 km × 4 km ROMS model, the ROMS4KM (Figure 1.3). The 160 m model, FC160m, was mainly used as an intermediate between the two other models and will not be discussed further. The main features and results of the other two models, FC800m and FC32m, are presented in separate sections based on Paper I and Paper II. An additional section summarizes the results obtained during further analysis of FC800m and observational data to investigate the effect of tidal mixing on stratification of the Faroe shelf. A preliminary manuscript with more detail on these results is attached as Paper III towards the end of the thesis.

4.1 FC800m: The 800 m model of the Faroe shelf

4.1.1 Setup and implementation of FC800m

The first part of the thesis work was to investigate the potential of a model based on the ROMS model system. ROMS has been set up in the North Atlantic region and validated towards observations here, by Lien et al., (2013) (Figure 4.1). Furthermore, this model is used for several sea lice applications in the Norwegian aquaculture industry and as this aspect is also relevant for the Faroe Islands the choice fell on this particular model.

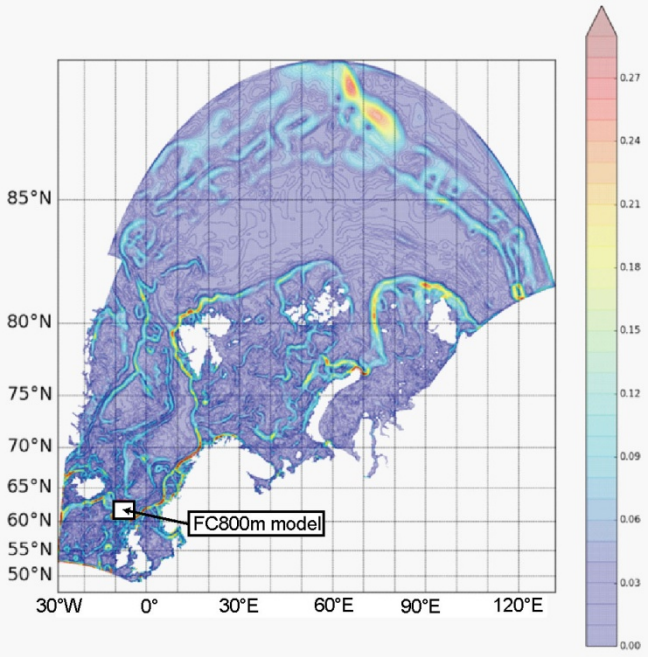

Figure 4.1. *Average barotropic velocity for 2013 in the ROMS4KM library used as lateral boundary condition for FC800m. The square indicates the domain of FC800m. Figure made in python from data supplied by Jon Albretsen.*

The model was set up locally on the Fiskaling high performance computer system "Munin", but required long computing time for realistic setups. Contact was therefore established to the Institute of Marine Research in Bergen, which has provided great help both in resources as well in academic counseling from the staff at IMR in Bergen, especially from Jon Albretsen who has worked extensively with the ROMS model system and helped us set up and run the model.

4.1.2 The average velocity field in FC800m

The horizontal variation of the barotropic velocity averaged over the whole year of 2013 is shown in Figure 4.2a for the parent ROMS4KM model and in Figure 4.2b for FC800m. The average velocity field has similar spatial structures in both simulations except at some of the boundaries. Most importantly, the currents over the shelf had compatible velocities to those observed in Larsen et al., (2008), (2009).

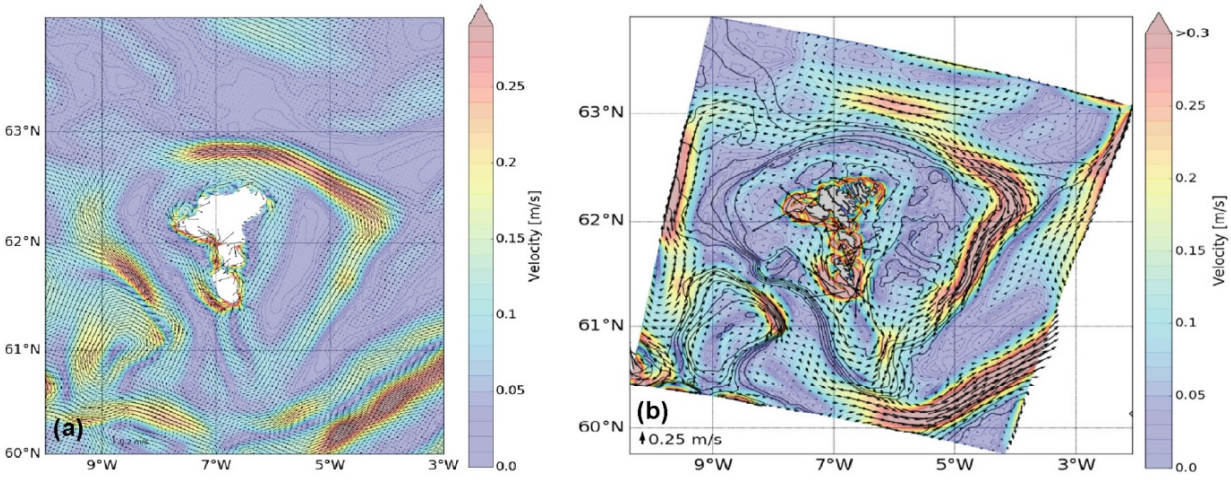

Figure 4.2. *Average barotropic velocities in the waters surrounding the Faroe Islands for 2013 in the ROMS4KM library (a) and in FC800m (b). Adapted from Paper I.*

4.1.3 Tidal sea level variations in FC800m

Tidal variations of sea level and currents are very important for the conditions on the Faroe shelf and in Faroese fjords and sounds. This will be apparent both in Paper II and Paper III. It is therefore essential for evaluating FC800m to verify that the model has realistic representation of the tides. Since this model was run over a whole year, the simulated sea level variations in each of the grid points is well suited for harmonic analysis as described in Sect. 2.2.1. The results of this analysis for the dominant semidiurnal and diurnal constituents are illustrated in Figure 4.3.

The Faroe Islands are located on the submarine ridge system that separates the Norwegian Sea from the rest of the North Atlantic where the tidal waves from the two ocean areas meet. It is well known that this is associated with strong variations in the tidal characteristics of the semidiurnal tides, especially M_2 with an amphidromic region somewhere in the area close to Tórshavn (e.g., Hansen, 1978; Simonsen & Niclasen, 2021). The upper panels of Figure 4.3 verify that FC800m does capture this feature. Not only M_2, but also S_2 and N_2 have strongly reduced amplitudes in the area close to Tórshavn (white circles in Figure 4.3). Remarkably, the two main diurnal constituents, K_1 and O_1 also seem to have an amphidromic character in the area close to Tórshavn.

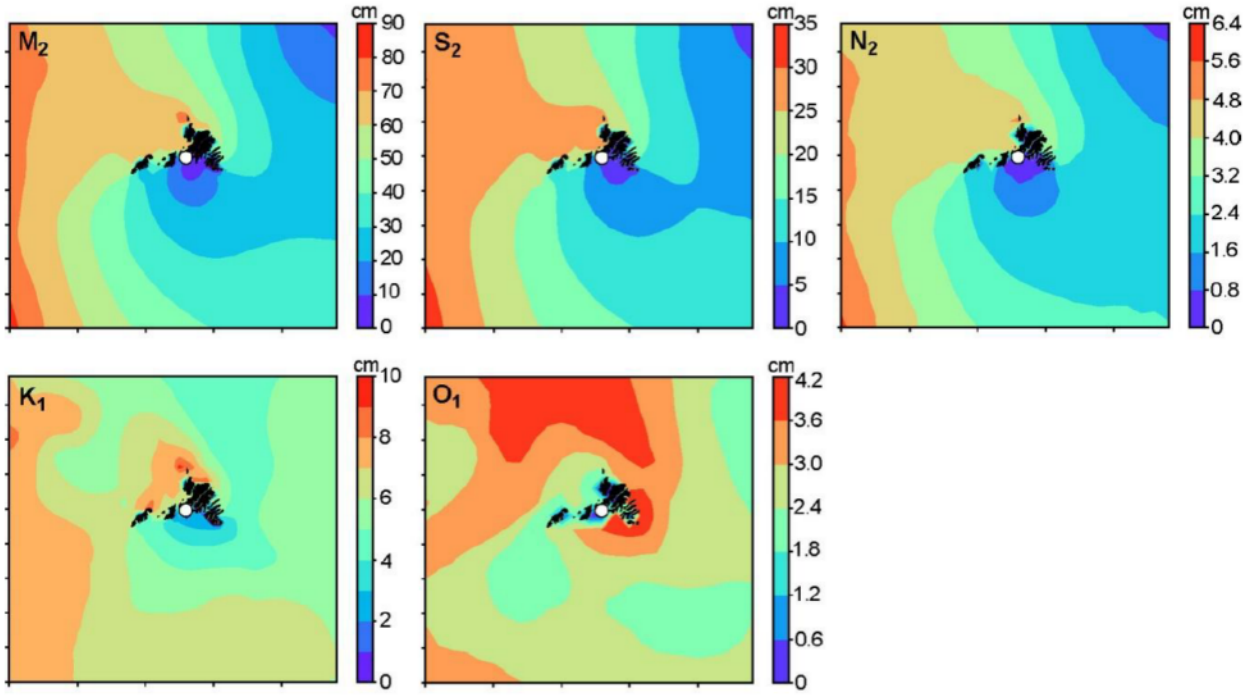

Figure 4.3. *Tidal amplitude in cm, of the dominant semidiurnal (M_2, S_2 and N_2) as well as the dominant diurnal (K_1 and O_1) constituents in FC800m. The white dot indicates the area just outside Tórshavn. Copied from the Supplement to Paper II.*

With the importance of the tides in mind, it was felt necessary to validate the tidal characteristics determined from FC800m against sea level measurements. For that purpose, sea level data from six tide gauges operated by the Faroese Office of Public Works (Landsverk) from 2009 to 2014 were analyzed and compared with the results from FC800m. The comparison for two of these stations is reported in Paper II while the appendix in Sect. 4.1.5 provides a more complete overview.

At a first glance, the message from the tables in the appendix is rather confusing. In most locations, the constituent M_2 will dominate and should be well determined by the harmonic analysis. Table 4.1 summarizes the comparison between FC800m and the tide gauge data for this constituent and the result is fairly encouraging at most locations. If we exclude Tórshavn, the simulated M_2 amplitude is at most 8% from the observed amplitude and the tables in Sect. 4.1.5 document that the observed amplitude varies somewhat depending on the period of analysis.

For all the locations in Table 4.1 except Tórshavn, the Gr-phase-lag difference is positive and varies by 9° (between +16° and + 25°), which is equivalent to a delay of less than twenty minutes. This general the delay is relatively small and likely derives from the forcing by the ROMS4KM model. The large discrepancies in amplitude ratio and Gr-phase-lag difference for Tórshavn were to be expected, since this is within the amphidromic region and indicate that considerably better resolution is needed to model this region.

Table 4.1. *Comparison between characteristics for M_2 as determined from FC800m for 2013 and from tide gauge measurements at six locations for 2009-2014. Amplitude ratio is defined as simulated amplitude divided by observed amplitude. Gr-phase-lag difference is simulated Greenwich phase-lag minus observed Greenwich phase-lag. The locations are shown on the map in the appendix in Sect. 4.1.5.*

	Eiði	Gamlarætt	Klakksvík	Krambat.	Sørvág	Tórshavn
Amplitude ratio:	1.08	1.02	0.99	1.04	1.02	0.39
Gr-phase-lag difference:	+20°	+25°	+16°	+16°	+19°	-33°

In addition to the main semidiurnal and diurnal constituents, the tables in the appendix also include harmonic constants for four long-period constituents, two fortnightly (Mf and MSf) and two monthly (Mm and MSm). The amplitudes of these constituents are much smaller than for the main semidiurnal and diurnal constituents and usually they are ignored. During the preparation of Paper II, it was found, however, that these long-period constituents were important for the circulation and exchange processes in “Sundalagið Norður”, which is a focus region of this thesis. They are also likely to affect the exchange processes in the southern part of this strait, “Sundalagið Suður”, and perhaps some of the adjacent fjords.

The spatial variations of the amplitudes of these four long-period constituents are illustrated in Figure 4.4. Although the amplitudes are much smaller than those for the semidiurnal and diurnal constituents, the relative variation in amplitude is still considerable. Unfortunately, the relative uncertainty in the harmonic analysis is especially high for the long-period constituents and this is reflected in the tables in the appendix, which show appreciable differences in constituents derived from observations for 2013 only compared to those derived for the whole 2009-2014 period.

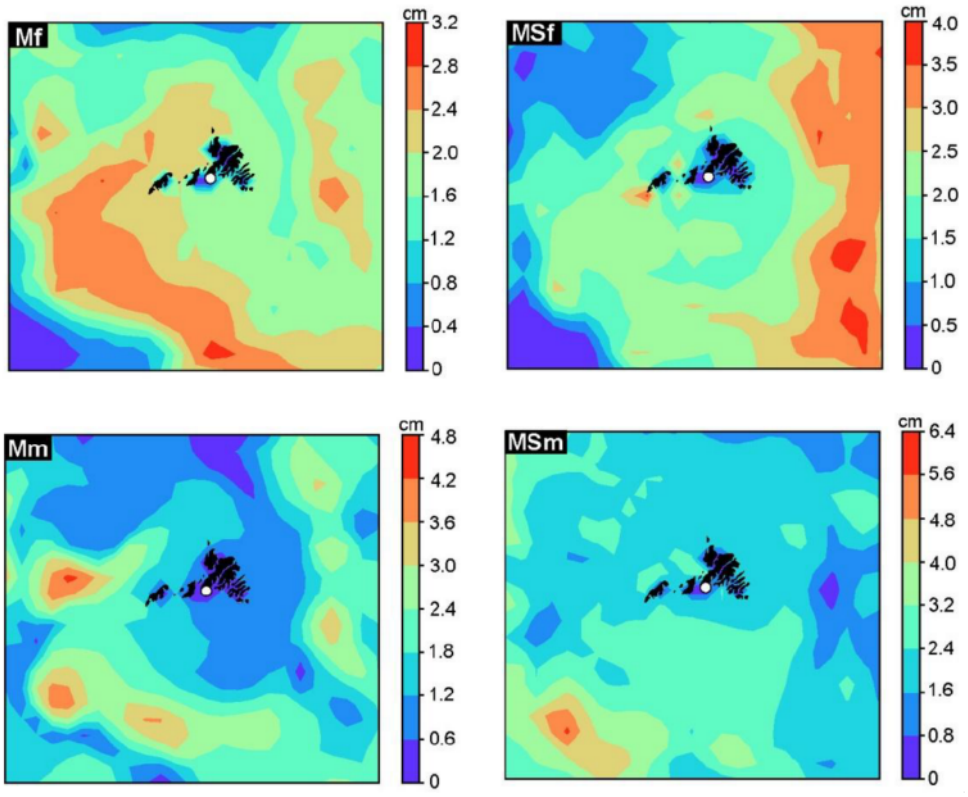

Figure 4.4. *Tidal amplitude in cm, of the dominant fortnightly (Mf and MSf) as well as the dominant monthly (Mm and MSm) constituents in FC800m. The white dot indicates the area just outside Torshavn. Copied from the Supplement to Paper II.*

4.1.4 Temperature variations in FC800

The main aim of the 800 m model was to act as the outer parent model for higher resolution nested models. However, in order to know the capability of the ROMS as a driver for such high-resolution nested domains one needs to know how the parent model performed. Thus, the focus of Paper I was validating the FC800m model. An overview of the seasonal, the horizontal and vertical temperature variation over the Faroe shelf in FC800m is presented in Figure 4.5 and this picture agrees well with the established picture for the Faroe shelf with a central area that remains well mixed throughout the year and seasonal stratification over the outer shelf (Larsen et al., 2008, 2009).

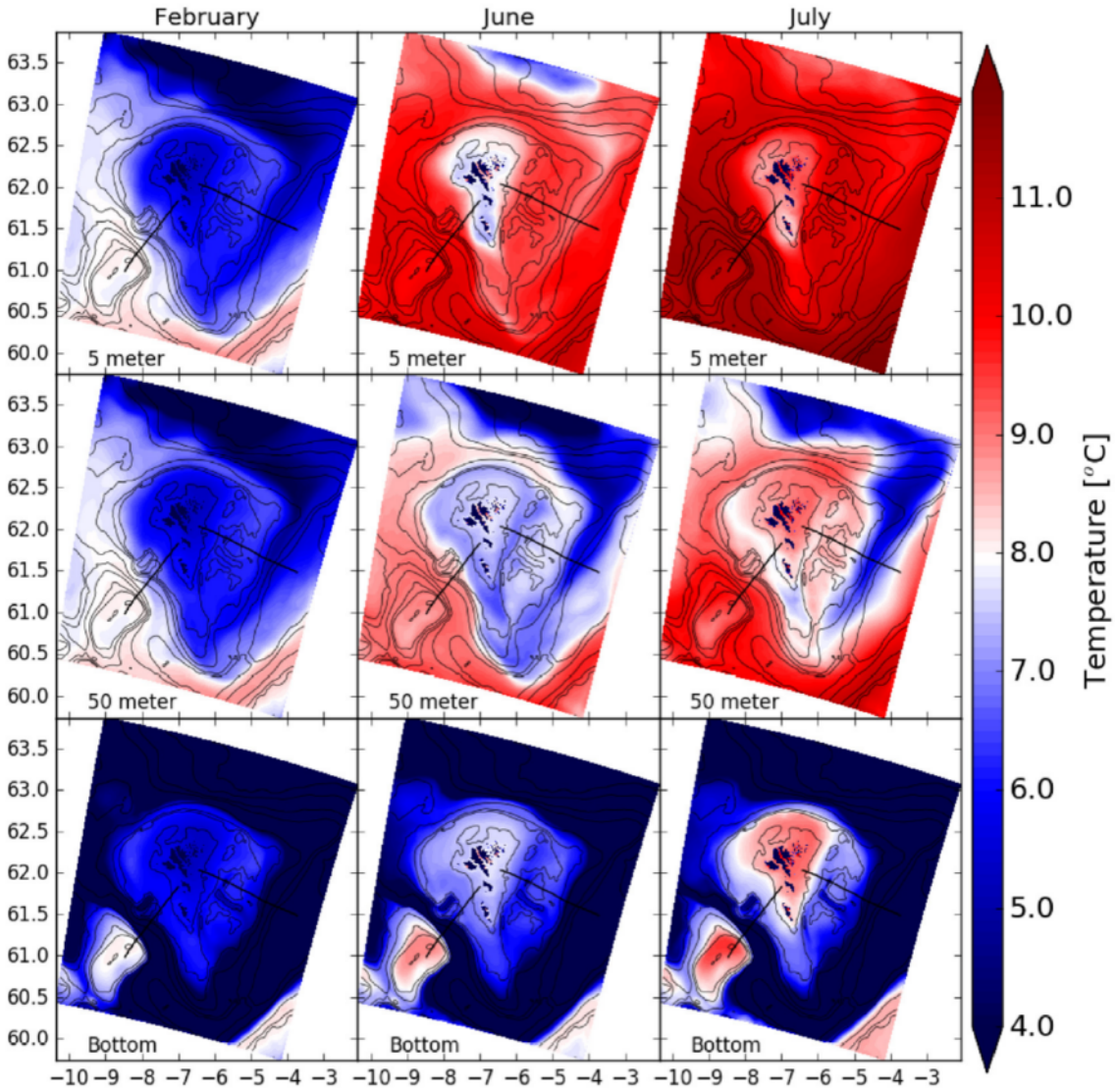

Figure 4.5. *Modeled temperature (◦C, color-bar) at 5 meters depth (top), and 50 meters depth (middle) and in the bottom layer (lowest) in February, June, and July 2013. Copied from Paper I.*

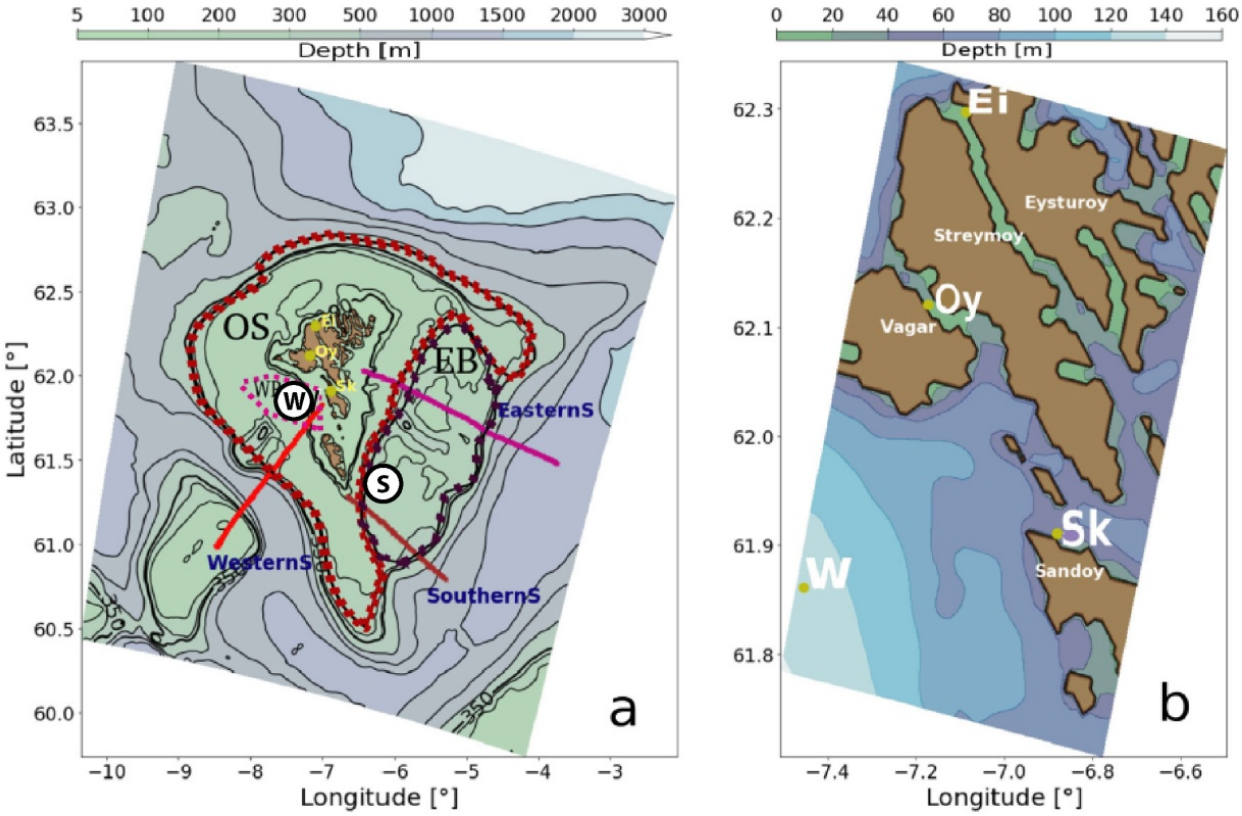

Figure 4.6. ***(a)*** *Locations of hydrographical observational data sets on the Faroe shelf. The thick lines, labelled EasternS, SouthernS, and WesternS, indicate standard CTD sections from which observational data are available for model validation. White circles with letters "W" and "S" indicate locations of two moorings with temperature loggers at different depths.* ***(b)*** *The locations of the coastal stations Ei, Oy and Sk, from which temperature time series are available. Adapted from Paper I.*

Paper I discusses in detail the validation of simulated temperature and salinity variations against observations both on-shelf and off-shelf. Here, only two examples will be discussed, comparing simulated and observed time series from two stations on the shelf (Figure 4.6a) and three coastal stations (Figure 4.6b).

The two stations "W" and "S" on the shelf have had temperature loggers close to the surface and close to the bottom (Figure 4.6a). The difference between these two temperatures, ΔT, may be seen as a measure of the stratification, which is a very important parameter for biological production (see manuscript III).

As mentioned previously, ROMS comes with a variety of options where one such option is the possibility of having increased vertical resolution near the surface or the bottom. As this thesis in particular is made for the applicability and usefulness towards the aquaculture industry in the Faroe Islands the focus for this parent study was to set up the model with special emphasis on the upper 50 meters. It is therefore encouraging to see that the model did compare favorably

with the observations (Figure 4.7). Certainly, the simulated values for ΔT (blue curves in Figure 4.7) are generally higher than the observed values (black curve), but the temporal variations are very similar in the simulations and observations. Also, the difference between the two stations is well reproduced in the model.

For the other example emphasized here, the surface temperature from the model simulation was validated against observations from three coastal stations (Figure 4.8). The observations were taken by the office of public works.

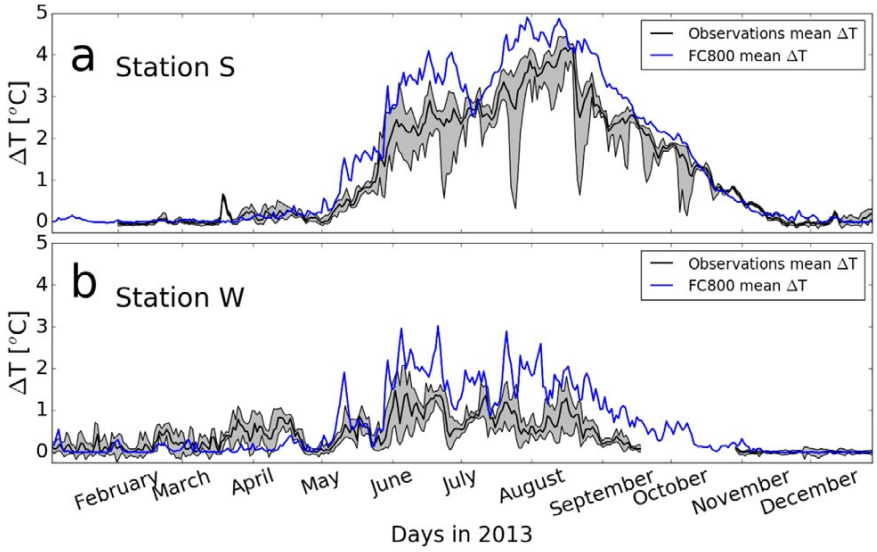

Figure 4.7. *Surface to bottom temperature difference at stations S* ***(a)*** *and W* ***(b)****. The black line is daily mean, while the gray areas indicate daily minimum and maximum measured temperature differences and blue lines are daily mean from the numerical model. Copied from Paper I.*

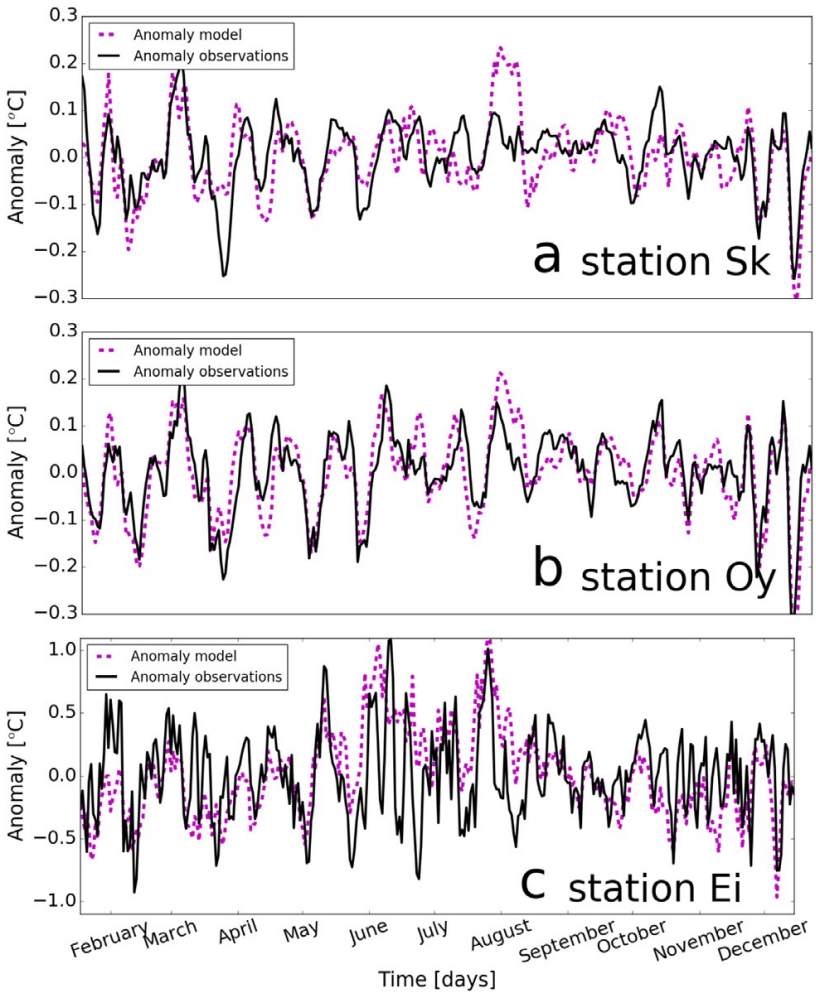

Figure 4.8. *Temperature anomalies at stations Sk* ***(a)****, Oy* ***(b)*** *and Ei* ***(c)*** *(Figure 4.6b) estimated by subtracting 30 day running mean from the daily mean temperatures. Note different vertical scale in the bottom plot. Copied from Paper I.*

From a visual inspection of Figure 4.8, the simulated temperature anomalies agree remarkably well with the observed anomalies at all of the coastal stations (Figure 4.6b). This good correspondence is verified by the high correlations listed in Table 1 of Paper I, where the Pearson correlation coefficient is 0.98 or higher for all of the stations.

Although the simulated temperatures for both these examples showed biases when compared with observations (Figure 4.7 and Table 1 in Paper I), the short-term temperature variations seem to be well simulated in the model. To some extent, this may be due to the high-resolution atmospheric forcing used for FC800m.

4.1.5 Appendix on validation of tidal constituents for FC800m

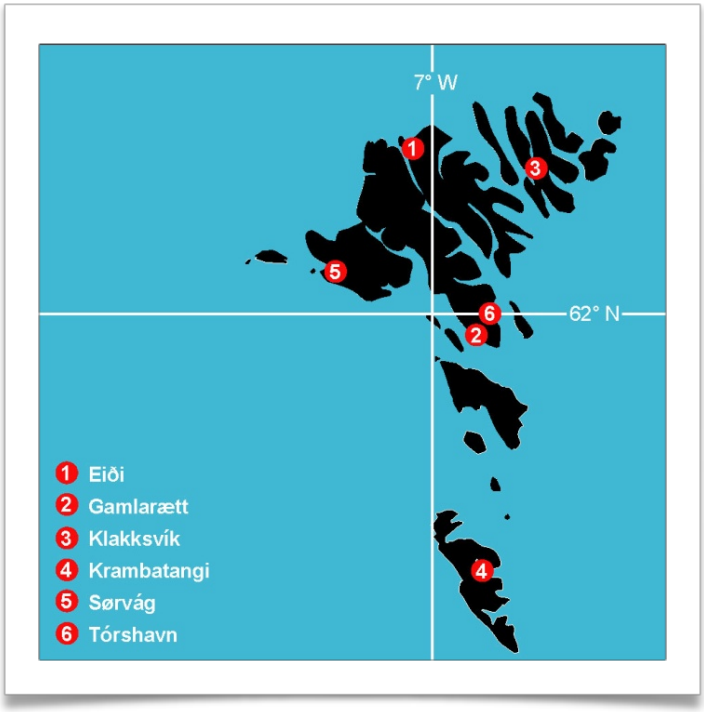

To evaluate the capability of FC800m to simulate the tides around the Faroe Islands adequately, characteristics of tidal constituents from the model, simulations were compared to those from tide gauge measurements. Observations of sea level height at six Faroese coastal sites (shown on the map on the right) were obtained from the Faroese Office of Public Works (Landsverk). All the observations cover the period 1 Jan 2009 to 31 Dec 2017 with a 10 minute interval, but there are many gaps as well as spikes in the data.

In order to remove the worst spikes, an error-flagging processing was carried out based on the approximation that the sea level height at a site can be seen as a superposition of a semidiurnal variation, a diurnal variation, and a slower residual variation, where the two amplitudes, the two phase-lags, and the residual may be seen as constant over a day, although they vary on longer time scales. To use this for de-spiking, the time series were split into sequences of 24 h 40 min (148 values) and a number of multiple linear regressions were run to determine the amplitudes and the residual while the phase-lags were varied in 10-minute intervals. The combination of phase-lags that gave the highest value for the explained variance R^2 was assumed to give the best fit to the data.

The original sea level values were then compared to this fit and all values that deviated more than 30 cm from the fit were error-flagged and ignored in the harmonic analysis. These sequences were selected every 12 hours (so that they overlap). If one or more spikes were found in a sequence, the regression was repeated.

The main outputs from this processing are six time series of quality controlled sea level height in which the identified spikes have been error-flagged. From visual inspection, several of the series seem to get offsets during the later years, especially after September 2014. Only data from before that date were therefore used. For each of the time series, amplitudes and Greenwich phase-lags were determined for the dominant semidiurnal, diurnal, and long-period constituents by harmonic analysis (Sect. 2.2.1). This was done both for the data from only 2013 and for the whole time series separately. On the three following pages, these values are shown together with

the characteristics determined from FC800m where the closest grid point to each of the sites was chosen to represent the site in the model.

Tables comparing amplitudes (in cm) and Greenwich phase-lags (in °) for nine selected tidal constituents as determined from the FC800m simulation (Model) and observations for 2013 (Obs. 2013) and for the 2009-2014 period (Obs. All) for six locations.

Eiði

Const.	Period	Amplitude (cm)			Greenw. phase-lag		
		Model	Obs. 2013	Obs. All	Model	Obs. 2013	Obs. All
M_2	12.42 h.	59.54	57.68	55.2	270	248	250
S_2	12.00 h.	20.45	19.61	19	286	281	282
N_2	12.66 h.	5.39	12.41	11.6	7	226	229
K_1	23.93 h.	7.36	9.12	8.5	286	159	161
O_1	25.82 h.	3.98	7.40	7.2	276	13	12
Mf	13.66 d.	1.18	2.10	1.5	204	157	186
MSf	14.78 d.	1.59	2.28	1.1	203	118	75
Mm	27.59 d.	1.58	3.26	1.6	190	193	172
MSm	31.81 d.	1.81	3.07	1.8	273	250	288

Gamlarætt

Const.	Period	Amplitude (cm)			Greenw. phase-lag		
		Model	Obs. 2013	Obs. All	Model	Obs. 2013	Obs. All
M_2	12.42 h.	30.45	32.24	29.78	207	180	182
S_2	12.00 h.	15.35	12.86	11.87	217	214	215
N_2	12.66 h.	3.11	5.92	5.37	284	162	164
K_1	23.93 h.	3.58	6.00	5.76	247	133	133
O_1	25.82 h.	2.58	5.50	5.08	292	41	42
M f	13.66 d.	1.43	2.73	1.94	203	163	189
M S f	14.78 d.	3.88	3.25	2.16	188	180	193
Mm	27.59 d.	1.51	4.01	2.66	190	200	197
MSm	31.81 d.	1.27	3.15	1.46	300	265	271

Klaksvík

Const.	Period	Amplitude (cm)			Greenw. phase-lag		
		Model	Obs. 2013	Obs. All	Model	Obs. 2013	Obs. All
M_2	12.42 h.	32.41	34.05	32.71	290	273	274
S_2	12.00 h.	10.56	11.22	10.85	301	309	307
N_2	12.66 h.	3.07	7.70	7.31	28	253	254
K_1	23.93 h.	4.25	6.72	6.20	286	163	165
O_1	25.82 h.	4.50	7.98	7.86	301	30	29
Mf	13.66 d.	1.21	1.65	1.75	194	148	179
MSf	14.78 d.	0.38	1.83	1.02	195	148	69
Mm	27.59 d.	1.56	3.84	1.68	215	204	170
MSm	31.81 d.	2.12	3.75	1.42	270	287	295

Krambatanga							
Const.	Period	Amplitude (cm)			Greenw. phase-lag		
		Model	Obs. 2013	Obs. All	Model	Obs. 2013	Obs. All
M_2	12.42 h.	28.97	29.34	27.95	214	195	198
S_2	12.00 h.	13.86	12.61	12.19	226	224	225
N_2	12.66 h.	2.67	5.96	5.69	308	170	173
K_1	23.93 h.	4.86	5.51	5.36	247	133	132
O_1	25.82 h.	3.37	6.08	5.80	318	46	46
Mf	13.66 d.	1.62	1.81	1.31	203	154	177
MSf	14.78 d.	0.44	1.64	1.75	132	113	65
Mm	27.59 d.	1.63	3.27	1.15	193	197	166
MSm	31.81 d.	2.50	4.64	1.61	273	288	289

Sørvágur							
Const.	Period	Amplitude (cm)			Greenw. phase-lag		
		Model	Obs. 2013	Obs. All	Model	Obs. 2013	Obs. All
M_2	12.42 h.	61.98	65.02	60.80	230	209	211
S_2	12.00 h.	28.68	24.05	22.77	239	245	245
N_2	12.66 h.	6.71	14.14	12.49	303	192	191
K_1	23.93 h.	5.35	8.46	8.03	258	142	143
O_1	25.82 h.	1.80	5.27	5.11	255	13	13
M f	13.66 d.	0.92	2.36	0.66	181	149	173
M S f	14.78 d.	1.34	2.55	1.93	181	91	74
Mm	27.59 d.	0.95	2.59	0.46	234	160	249
MSm	31.81 d.	1.34	3.33	1.69	281	254	280

Tórshavn							
Const.	Period	Amplitude (cm)			Greenw. phase-lag		
		Model	Obs. 2013	Obs. All	Model	Obs. 2013	Obs. All
M_2	12.42 h.	3.31	9.30	8.48	164	196	197
S_2	12.00 h.	3.97	5.08	4.73	195	213	215
N_2	12.66 h.	0.15	1.68	1.51	261	171	180
K_1	23.93 h.	2.58	4.38	3.81	248	140	139
O_1	25.82 h.	4.54	7.18	6.51	319	52	52
Mf	13.66 d.	1.29	2.16	1.64	201	159	176
MSf	14.78 d.	1.48	2.30	0.62	201	184	146
Mm	27.59 d.	1.68	4.26	1.74	190	200	179
MSm	31.81 d.	1.98	4.24	1.12	272	292	281

4.2 FC32m: The 32 m model of Sundalagið Norður

4.2.1 Background, setup, and implementation of FC32

The 32 m model was set up for the focus region of this thesis "Sundalagið Norður", which is the northern part of the narrow strait between two of the largest islands. The implementation and results for this model are described in Paper II: "*A tidally driven fjord-like strait close to an amphidromic region*". This paper has been resubmitted to Ocean Science after major revisions.

The motivation for the study was to establish whether the model system setup for the Faroe Islands with the triply nested (800 m → 160 m → 32 m) model system (Figure 1.3) could be used for scientific studies as well as questions of more commercial interest. The model was designed to include the focus region (red rectangle in Figure 4.9 labeled "Estuary") and the open ocean to the north as well as the immediate area south of the focus region. In the original submission of Paper II, the term "estuary" was used for the focus region as indicated in Figure 4.9, but all three referees considered it rather a strait, which motivated the term "*fjord-like strait"* in the revised title. Henceforth, Sundalagið Norður will be termed "*the strait*".

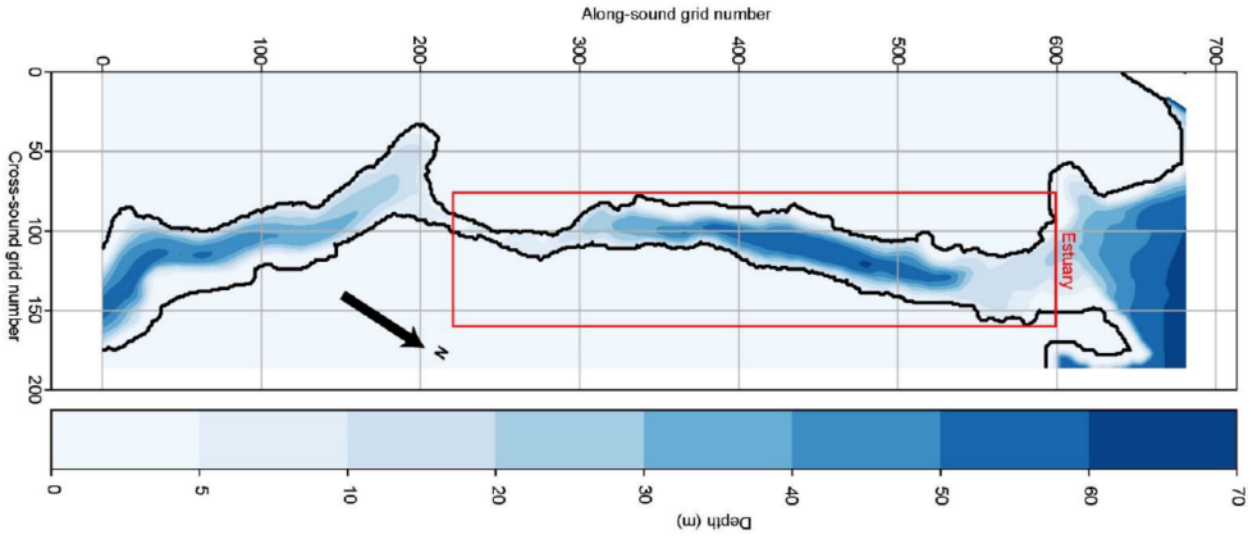

Figure 4.9. *The domain of FC32m with the focus region, "Sundalagið Norður", enclosed within the red rectangle. The region has shallow sills in both ends. The northern sill has a sill depth of 11 m and the southern sill around 4 m. Between the sills, bottom depths reach more than 60 m.*

The only previously published study of this region, is from the 1980's (Hansen, 1990). This study describes the Sundalagið Norður as a sill fjord with a periodically stagnant bottom layer during summer, at least some years. This same study also suggested that the typical time for the brackish water in Sundalagið Norður to be flushed out of the area is about five days, based on

observations. Hansen (1990) suggested that tides rather than estuarine circulation drive the circulation in Sundalagið Norður.

As elaborated in Sect. 4.1, the main conclusion of Paper I was that FC800m simulated tides, currents, and temperature on the Faroe shelf fairly well compared to observations and established knowledge. Thus, FC800m should be well suited to drive a higher resolved nested area through the intermediate 160 m model. This was tested with a 4 week simulation of FC32m during February and March of 2013.

4.2.2 Validation of FC32

The validation was done with focus on three different types of observations. One type was the set of tide gauge measurements from the Faroese Office of Public Works at six coastal stations around the Faroe Islands. One of these stations, "Eiði", is located within the strait, just south of the northern sill. Another station, "Tórshavn", is located south of the southern sill in an amphidromic region for the semidiurnal tide where amplitudes and phase-lags change over short distances. The duration of the FC32m simulation was too short to allow harmonic analysis with reasonable accuracy. Therefore, the harmonic analyses from FC800m were used (Table 4.1 and Sect. 4.1.5). These analyses did exhibit differences between the harmonic constants from the simulated and observed sea level time series, but the tidal forcing is mainly determined by the strength and timing of the sea level difference between both ends of the strait. For this parameter it was concluded in Paper II that "*the tidal forcing of the strait, thus, is fairly accurately simulated by the model*".

The second type of observations used for validation was a set of current velocity measurements within the strait during the simulation period. These observations were obtained as a part of a project in 2013 (ASAF) where three different moorings were deployed in the strait at the same time, two ADCPs and one AWAC. The two ADCP data sets could be used for validation as illustrated in Figure 4.10. Although the simulated and observed velocities in Figure 4.10 are not identical, the velocities are of similar magnitudes and similar patterns are seen in both Hovmøller diagrams from each location. A more objective correlation analysis (Figure 3 in Paper II) verifies this.

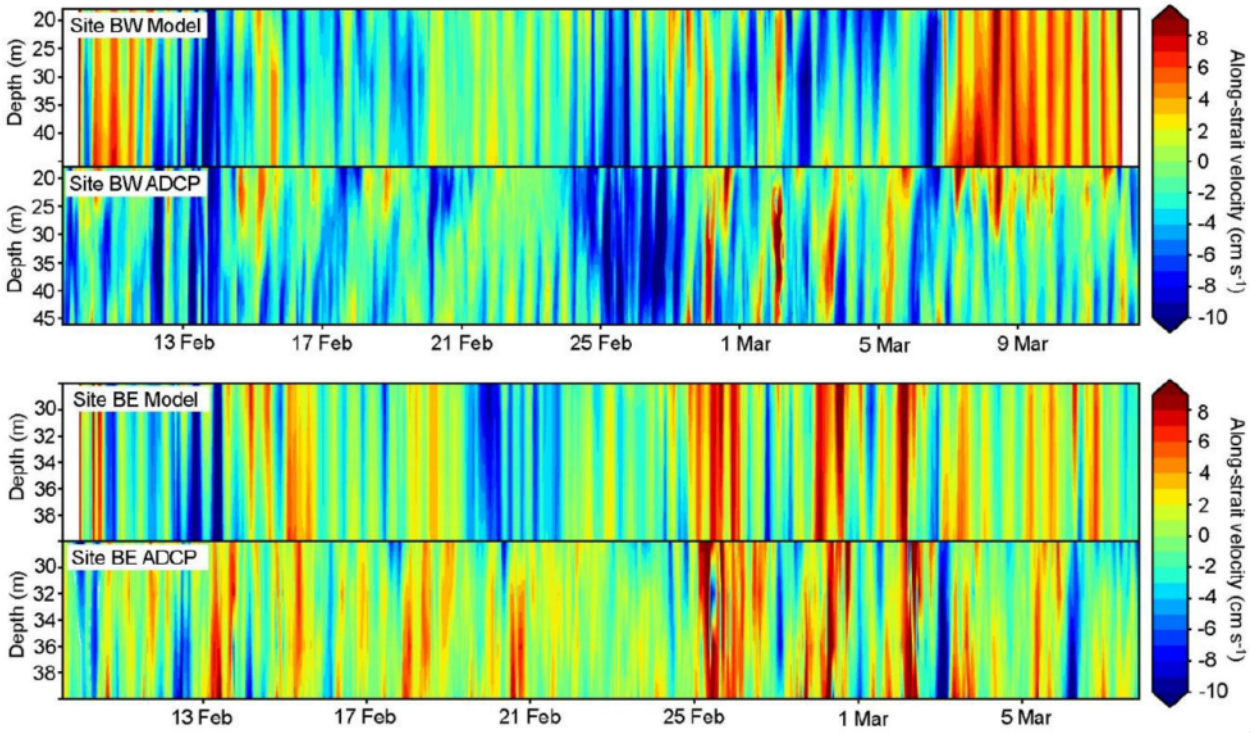

Figure 4.10. *Hovmøller diagrams showing the vertical and temporal variations of along-strait current velocities at two locations, BW (top) and BE (bottom), within the strait (see Figure 1 and Figure 2 in Paper II for locations). For each of the locations, the lower panel (ADCP) shows observed velocities while the upper panel (Model) shows simulated velocities from a grid point close to the mooring.*

The third type of observations was salinity, which during winter is the main hydrographic parameter determining stratification in the strait. No hydrographic observations were made during the simulation period. Instead, simulated salinity profiles were compared to observed profiles obtained in other years during winter. The correspondence was not impressive, but the model was run with constant runoff rate and can therefore not be expected to reproduce the periods with excessive runoff that occur in nature. Thus, no conclusion as to model performance on salinity simulation could be drawn.

4.2.3 Driving mechanisms for Sundalagið Norður

Estuaries are typically forced by three types of driving mechanisms: winds, tides, and estuarine forcing induced by freshwater runoff from land (Figure 2.1). In the FC32m simulations of Sundalagið Norður, it seems clear that tidal forcing is dominating. This is evident in the thin red and blue curves in Figure 4.11c, which represent volume transport across the two sills. If there was appreciable wind forcing, the semidiurnal variations in simulated volume transport would hardly be so regular. A similar argument can be put forward for estuarine forcing, although one

might perhaps see a larger effect if the runoff applied to the model was allowed to vary as in nature rather being constant.

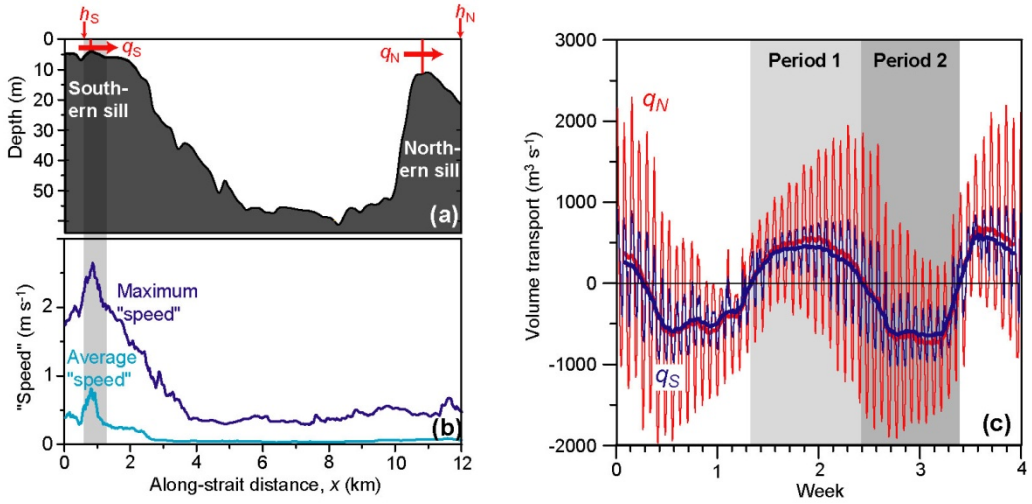

Figure 4.11. (a) *A section along the strait. The bottom depth indicated is the maximum depth along each section crossing the estuary. Horizontal red arrows indicate simulated volume transport across the southern sill, q_S, and across the northern sill, q_N. Vertical red arrows indicate locations for sampling sea level south of the strait, h_S, and north of the strait, h_N.* ***(b)*** *The cyan and dark blue curves show the along-strait variation of maximum (dark blue) and (temporally) averaged "speed", defined as the absolute value of the cross-strait averaged along-strait velocity component.* ***(c)*** *Hourly (thin lines) and 25-hour averaged (thick lines) simulated northward volume transport across the northern sill, q_N, (red) and across the southern sill, q_S, (blue). Adapted from Paper II.*

The amphidromic character of the region south of the strait (Figure 4.3) implies that the tidal sea level variations south of the strait are much smaller than those north of the strait. The sea level difference between both ends of the strait (h_N – h_S), therefore, varies with dominantly semidiurnal periodicity and relatively large amplitudes. This induces strong pressure gradients along the strait, which induces acceleration (e.g., Eq. (2.3)). Verification of this kind of tidal forcing is provided by the high correlations in the two bottom rows of Table 2 in Paper II.

An interesting feature of Figure 4.11c is that the amplitude of q_S (thin blue curve) seems consistently to be only around half the amplitude of q_N. This implies that only around half of the water entering the strait from the north during the rising tide manages to leave the strait across the southern sill. The rest has to return northwards on the ebbing tide as in a tidally forced estuary or fjord. This was the motivation for using the term "*fjord-like strait*" in the revised title.

The reason for this seems to be the small cross-sectional area over the southern sill, which is almost twenty times smaller than the cross-sectional area over the northern sill. This induces very high velocities over the southern sill (Figure 4.11b), which again leads to strong bottom friction. According to the interpretation in Paper II, around half of the potential energy typically

generated by tidal sea level variations is lost to friction and that loss occurs in a small area over the southern sill (shaded region around x = 1 km in Figure 4.11a,b).

4.2.4 Mixing processes in Sundalagið Norður

The hydrostatic approximation used in FC32m is not optimal for studying mixing processes. In addition, the model was unfortunately not set up to store some important mixing parameters, such as turbulent dissipation rate. The information that can be gained from FC32m on mixing processes in the strait is therefore limited, but the model can simulate density inversions and they are usually associated with enhanced mixing. As shown in Figure 4.12, density inversions do occur over the southern slope of the northern sill and they are clearly modulated by tidal variations (Figure 4.12b). This should be considered in future modelling studies of this strait.

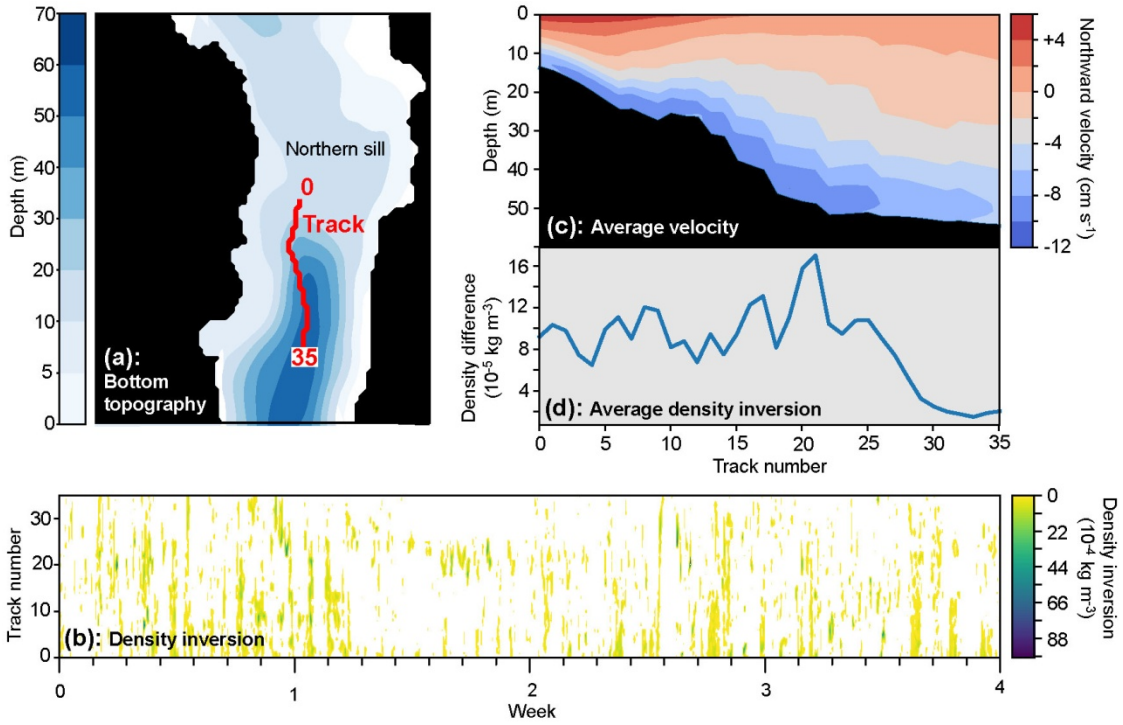

Figure 4.12. (a) Bottom topography around the northern sill. The red line shows a track with numbers ranging from 0 to 35, which are used in the other panels. (b) Density inversion, defined as density (σ_θ) difference between the deepest layer and two layers above (layer 2 minus layer 0) along the track every hour. Only positive values are shown (negative values white). (c) Average northward velocity at various depths along the track. (d) Density inversion along the track averaged over the whole period. Adapted from Paper II.

4.2.5 Fortnightly variations in Sundalagið Norður

Perhaps the most unexpected result to come from the FC32m simulations was the identification of strong long-period variations, mainly with fortnightly periodicities. As seen in Figure 4.11c, there are two types of fortnightly variations. The first type is the variation in amplitude of the semidiurnal oscillations (thin curves in Figure 4.11c). This kind of fortnightly variation is to be expected as the different semidiurnal constituents, especially M_2 and S_2, vary between being in phase and out of phase according to the lunar cycle.

The second type of fortnightly variations is seen in the thick red and blue curves in Figure 4.11c, which show 25-hour averaged volume transports across the two sills. These curves also exhibit long-period variations, mainly of fortnightly periodicity. A part of this signal comes as a residual from the averaging of the semidiurnal and diurnal transport variations, because these variations do not have periods that are exactly equal to the 25-hour averaging period or half of it. This part would, however, be much smaller than what is shown by the thick curves in Figure 4.11c.

Instead, it was concluded in Paper II that most of the signal shown by the thick curves in Figure 4.11c was caused by the long-period tidal constituents of sea level (Mf, MSf, Mm, and MSm). The amplitudes of these constituents are much smaller than for the semidiurnal and diurnal constituents (tables in Sect. 4.1.5), but they don't average out over 25 hours as the semidiurnal and diurnal constituents (almost) do. This means that the 25-hour average of the sea level difference between both ends of the strait, ($h_N - h_S$), varies over fortnightly periods. This variation drives the fortnightly variation in average flow through the strait.

When this explanation was first identified in the simulations from FC32m, it was hypothesized that this might be a model artifact, but analysis of tide gauge data from Eiði and Tórshavn verified that the signal is also found in nature. This is documented in Figure 4.13 where the blue curve shows the 25-hour averaged sea level difference between Eiði and Tórshavn calculated by using the observed harmonic constants of three semidiurnal (M_2, S_2, and N_2) and two diurnal (K_1 and O_1) constituents. The red curve uses the same semidiurnal and diurnal constituents, but also uses four long-term constituents (Mf, MSf, Mm, and MSm), in addition. The blue curve changes sign several times a day, whereas the red curve has a dominant fortnightly variation.

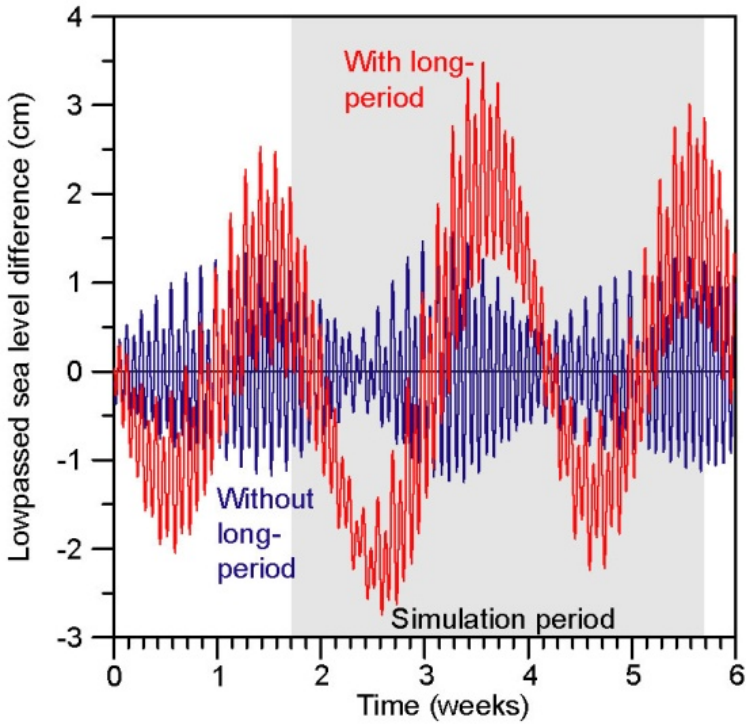

Figure 4.13. *Lowpassed (25-hour averaged) sea level difference between Eiði and Tórshavn (Eiði minus Tórshavn) calculated from the "observed" amplitudes and Greenwich phase-lags in Table 1 in Paper II for a six-week period starting 1 February 2013. The blue curve is generated by using only the five semidiurnal and diurnal constituents in the table. The red curve is based on all the constituents including the four long-period constituents. The gray-shaded area indicates the simulation period. Adapted from Paper II.*

Paper II, therefore, concludes that the fortnightly variation is not a model artifact although it may perhaps be enhanced in the model simulations. According to the FC32m simulations, the effect of the long-period tidal constituents has profound influences on the net flow through the strait and its exchange with the areas outside both ends of the strait. This is illustrated in Figure 4.14 which shows volume transports averaged over the two periods defined in Figure 4.11c. Not only is the net flow through the strait different in the two periods, but the flow – and hence the flushing – is also different at depth (note the deep blue arrows).

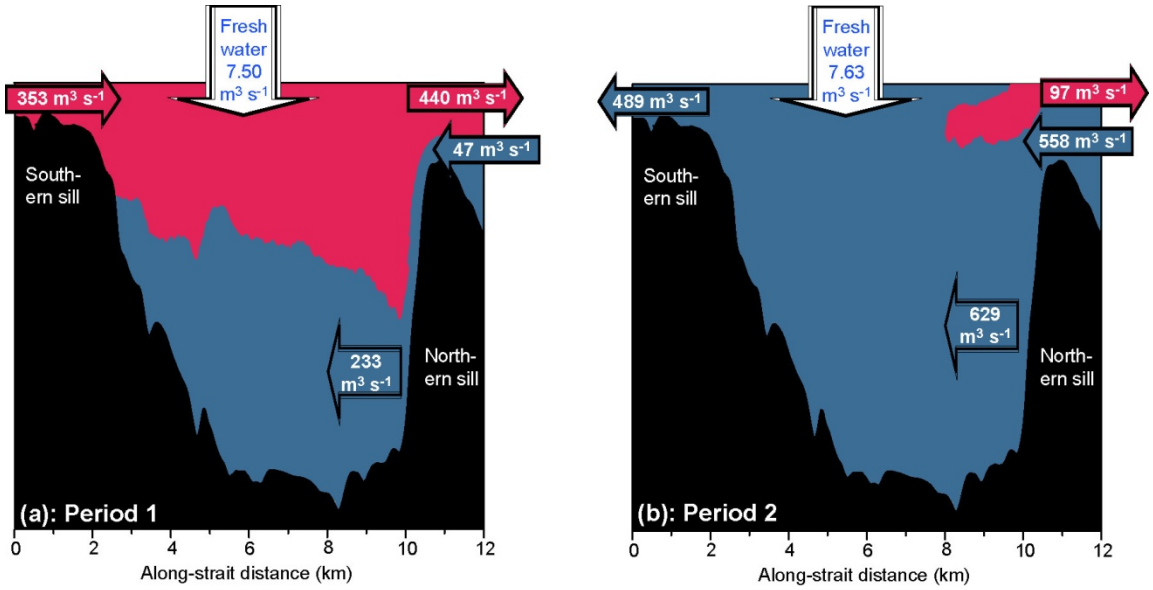

Figure 4.14. *Schematic flow patterns and exchanges for the two periods defined in Figure 4.11c. Red and blue areas show north- and south-going (cross-estuary averaged) flow, respectively. Horizontal arrows over the two sills show average volume transport over the sills for each period. The wide south-going arrow at depth for each period shows the total south-going volume transport just south of the northern sill (along-strait distance ≈ 10 km). Vertical arrows show average freshwater supply to the estuary for each period, including river and hydropower supply (constant) as well as precipitation (variable). Note that the transport values are based on averages for each period with sea level kept constant, which explains why they do not balance.*

In conclusion, one has to agree with the referees that Sundalagið Norður by the strictest definition is a strait since it is open in both ends. In many ways, this strait does, however, behave like a fjord, especially since the strait receives high amounts of fresh water as runoff. Remarkably, the long-period tides seem to induce fortnightly shifts between more fjord-like and more strait-like behavior, Period 1 and Period 2 respectively in Figure 4.14.

4.3 Paper III: The effects of tidal mixing on stratification over the Faroe shelf

4.3.1 Motivation

The main motivation for this study was the importance of stratification for the primary production and thus the entire ecosystem on the Faroe shelf. This is illustrated in Figure 4.15 from a publication by Eliasen et al. (2017). The left panel in this figure shows the dominant EOF (Empirical Orthogonal Function) mode of near-surface chlorophyll concentration as determined from satellite data. The open ocean is seen to differ from the central shelf (CS) as well as the eastern banks (EB).

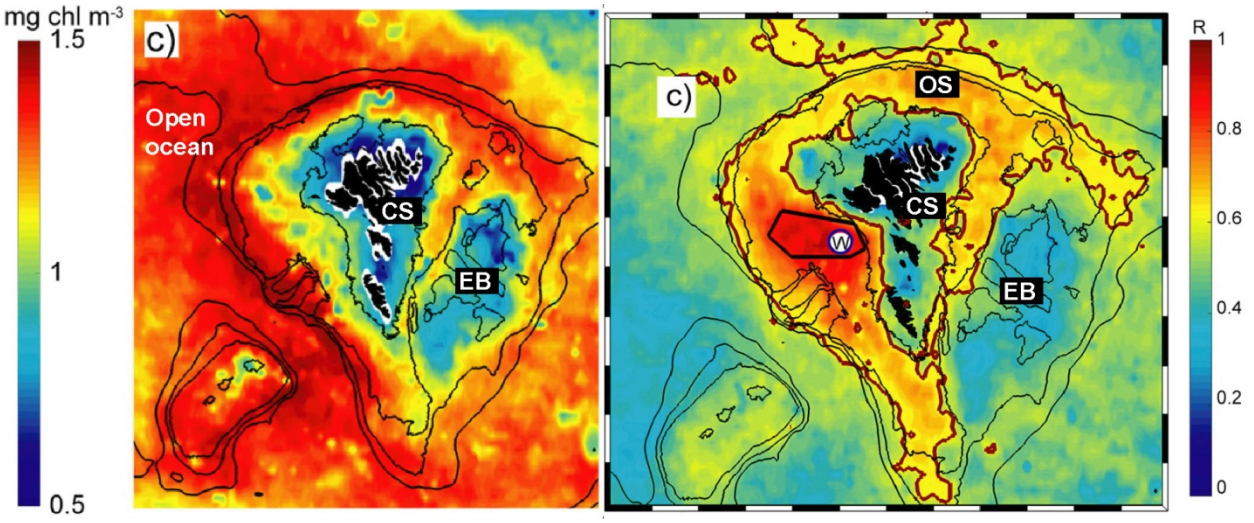

Figure 4.15. Characteristics of near-surface chlorophyll (chl) concentrations in the waters surrounding the Faroe Islands based on satellite data. Left panel: The leading EOF mode, explaining 75% of the total variance. Right panel: Correlation between the spatially averaged chl time series from the black polygon labeled W and the chl in each grid point. The R=0.6 correlation contour is drawn in dark red. Three regions labeled OS (Outer shelf), CS (Central shelf) and EB (Eastern banks) are indicated. The 100m, 200m, 300m, and 500m isobaths are shown. Adapted from Eliasen et al. (2017).

From a physical point of view, the main difference between the open ocean and the central shelf is the stratification. The open ocean becomes stratified in summer, whereas the central shelf is almost always vertically homogeneous. It is well established that the reason for this is the intensive mixing over the central shelf induced by the strong tidal currents. It seems likely that the patterns of phytoplankton biomass seen in the left panel of Figure 4.15 reflect patterns of stratification.

In general, the development of stratification may be seen as a competition between the stratifying effect of heat input from the atmosphere and the de-stratifying effect of mixing, which

may come from turbulence induced by currents or from wind. The open ocean and the central shelf may be seen as two extremes representing persistent summer stratification and persistent un-stratified waters, respectively. But, one would also expect there to be a transition area between these two extremes; an area, which may become stratified, although less regularly than the open ocean.

The spatial variation of atmospheric heat input and winds should be considerably smaller than the spatial variation of tidal mixing. Therefore, it seems likely that the strength and variations of tidal mixing to a large extent determine the conditions for stratification and hence primary production in the transition areas.

One such transition area is the region labeled OS (outer shelf) in the right panel in Figure 4.15. The high correlations seen in this figure imply that the temporal variations of primary production are similar throughout this region, most likely because of similar temporal variations in stratification. The thick red lines in the panel define this region and it is seen to roughly be located between the 100 m isobaths and the 200 m isobaths. In this region, the tidal current speed is in general intermediate between the high speeds over the central shelf and the low speeds over deeper areas.

On this background, the main hypothesis motivating this study is that the characteristics of the tidal currents to a large extent determine the conditions for stratification and primary production in the transition areas. This seems most likely to be the case for the outer shelf (OS) region, but could conceivably also be the case for the eastern banks (EB). As noted in Paper I, the results from FC800m are in fairly good agreements with the regional classification suggested by (Eliasen et al., 2017).

4.3.2 Theory

The question of stratification in a system that is heated from above and stirred by tidal mixing has been treated by several authors as reviewed by Simpson & Sharples (2012). They quantify stratification by the parameter:

$$\Phi = \frac{1}{h}\int_{-h}^{0}\left[\hat{\varrho} - \varrho(z)\right] g z \, dz \qquad (4.1)$$

where h is bottom depth and $\hat{\varrho}$ is the depth averaged density. The governing equation for stratification then becomes, their Eq. (6.14):

$$\frac{\partial \Phi}{\partial \mathrm{t}} = \frac{\alpha g Q}{2c} - \frac{ek\varrho_0 |u|^3}{h} \qquad (4.2)$$

where $\alpha = 1.5 \cdot 10^{-4}$ [°C^{-1}], $g = 9.8$ [m s^{-2}], $c = 4000$ [J kg^{-1} °C^{-1}], $e \approx 0.004$, $k \approx 0.0025$, $\rho_0 = 1027$ [kg m^{-3}] while Q is the heat flux through the surface and u is the speed of the tidal current. The stratification parameter may be related to a more traditional parameter such as the temperature difference between surface and a given depth, ΔT, if the shape of the temperature profile is known. Generally:

$$\frac{\partial \Delta T}{\partial \mathrm{t}} = \gamma \frac{1}{\alpha g \varrho_0 h} \frac{\partial \Phi}{\partial \mathrm{t}} = \frac{\gamma Q}{2c\varrho_0 h} - \frac{\gamma ek|u|^3}{\alpha g h^2} = A\frac{Q}{h} - B\frac{|u|^3}{h^2} \qquad (4.3)$$

where γ is a dimensionless number greater than 1 that is dependent on the shape of the temperature profile and will be higher, the thinner the heated surface layer is. The two coefficients A and B will have the values:

$$A = 1.25 \bullet 10^{-7} \bullet \gamma \left[\frac{\text{°C m}^3}{\text{J}}\right] \quad \text{and} \quad B = 6.8 \bullet 10^{-3} \bullet \gamma \left[\frac{\text{°C s}^2}{\text{m}}\right] \qquad (4.4)$$

4.3.3 Preliminary results from FC800m

A main characteristic of the tidal currents over the Faroe shelf is that they are dominated by semidiurnal periodicities and that the amplitudes of these semidiurnal variations vary on fortnightly time scales with the changing phases of the moon. In areas where tidal mixing affects stratification, we might therefore expect to see variations of near-surface temperature with fortnightly periodicities. And that indeed seems to be the case (Figure 4.16).

As argued in the theoretical section above, e.g., Eq. (4.3), the effect of tidal mixing may be parameterized by the current speed to the third power (current speed cubed). The average value of this parameter is illustrated in Figure 4.17b and it displays similar distribution patterns as the average stratification (Figure 4.17a). Generally, both distributions follow bottom topography, but north of the islands, stratification is especially weak whereas current speed is especially high. This is as expected if tidal mixing has a large effect on stratification.

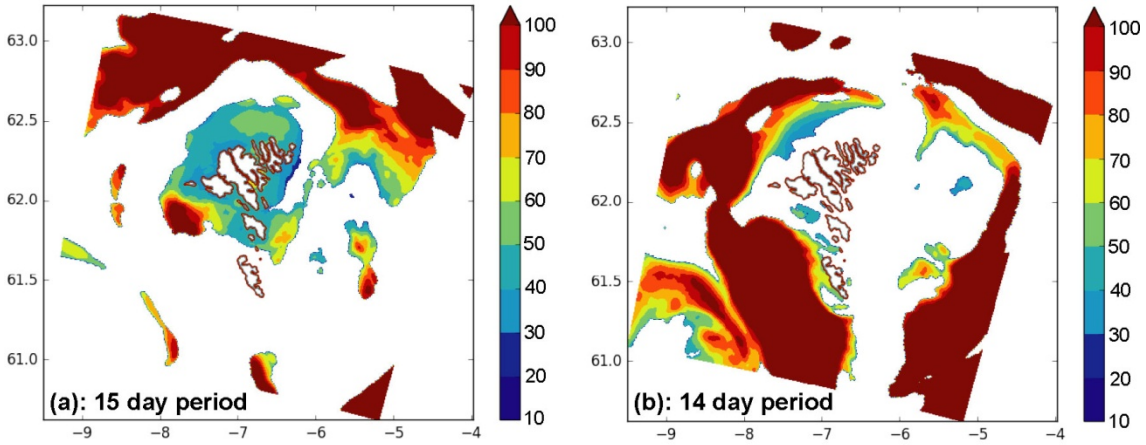

Figure 4.16. *Spatial variation of the amplitudes of spectral peaks of near-surface temperature with periods of 15* ***(a)*** *and 14* ***(b)*** *days in a relative scale with the strongest signal set to 100. White areas have signal-to-noise ratio less than 3:1 where the noise is estimated as the standard deviation of the signal. Copied from Paper III.*

This relationship, is further strengthened by correlation analyses of the FC800m simulations as well as observational data (Paper III). The general picture seems to be that areas around the 100 m isobath east and north of the islands may become stratified when positive heat input coincides with weak currents, but the stratification is short-lived. Longer-lasting stratification is seen at larger depths, but seems also to correlate negatively with current speed cubed, especially north of the islands.

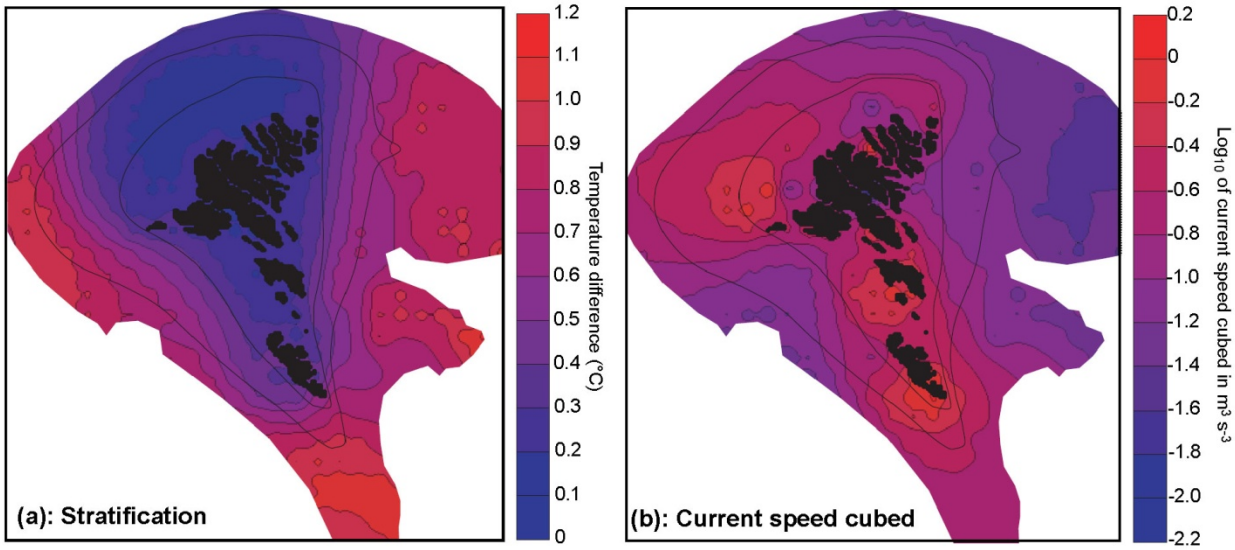

Figure 4.17. ***(a)*** *Average (Jan-Sept) stratification defined as simulated temperature difference between 5 m and 50 m depth, ΔT.* ***(b)*** *Logarithm (base 10) of the average (Jan-Sept) simulated current speed cubed. Thin black lines indicate the 100 and 150 m depth contours. Copied from Paper III.*

4.3.4 Further work

As previously stated, the results in Paper III are at a preliminary stage, but they do clearly indicate that tidal mixing does affect stratification over the Faroe shelf; not only over the strongly mixed central shelf, but also over deeper water, especially the outer shelf. Paper III also demonstrates that FC800m should be a good tool for further work.

5 Summary and outlook

This thesis is a synthesis of three separate papers that are included. In general, the thesis is based on computational science and oceanography. The thesis has contributed to knowledge on the oceanography of the Faroe Shelf as well as on fjord dynamics.

For the first study, which has been published, "*A step towards high resolution modeling of the Faroe Shelf by FarCoast800*", the main aim was on validation. The results were sufficiently positive to let us continue to work with a ROMS based system in terms of FarCoast in the Faroe Shelf. However, we still gain the option to use another system than ROMS4KM in future on the boundaries for forcing, even though FarCoast itself will be based on ROMS for the model setup. One of the main issues in regards to this first study was that along the eastern and northern boundaries, spurious currents developed within the FarCoast800m domain. This we have worked towards solving in a future setup where the grid domain for the outer region will be tilted, to ensure that the intense velocities seen from the Scottish Slope Current are not entering at such a steep angle as was the case for FarCoast800. However, the conclusion was still that the currents on the shelf itself were not influenced by the spurious currents on the outer perimeters of the domain.

For the second paper the focus was on the sound Sundalagið Norður and the areas outside both ends. For this model setup the very high resolution FarCoast32m was used. The decrease of the horizontal resolution also demanded a decrease in the size of the time step as to keep the CFL criterion fulfilled. This made the calculation very demanding computationally and thus the simulation period was very short. However, the aim was that the simulation should include the period when actual current measurements were available. This was why the short period during February and March was chosen. The model FarCoast32m was validated in paper II and found to be a good choice for such highly resolved model domains. The heavy computational demand emphasized the importance of considering both location and periods for such future calculations when considering setup of the model domain. In the future, it should also be considered whether high resolution in space is more important than the length of the simulation period. Paper II demonstrates the dominance of tidal forcing for Sundalagið Norður, both the semidiurnal and diurnal tides, but also long-period tides. Unfortunately, the simulation period, which was chosen to get an overlap with observations, did not include the summer period when there is a risk of developing a stagnant bottom layer. For future studies this would be interesting to investigate further, also to see if the long-period tides influence the risk of developing a stagnant bottom layer. Furthermore, the density inversions and the possibility of periodic hydraulic jumps over the slope of the northern sill, could be investigated further by storing additional parameters in the model output. This concept would also be highly interesting to further study with a more targeted field experiment.

The third manuscript returns to the 800 m model, but also focuses on tidal dynamics as this study investigates a fortnightly signal in the temperature over the outer shelf and aims at clarifying the effect of tidal currents on stratification over the shelf. Although still in preparation, the results clearly indicate that there is an effect, although different in different areas. The amphidromic character of the Faroe shelf is essential in generating the strong tidal currents that mix the water and break down stratification. The success of FarCoast800 in simulating the tides should therefore be well suited for this study.

Many of the hours spent working towards these results have been spent on computing. This involved setting up the local computer MUNIN to be able to run FARCOAST locally, as well as analyzing the output from ROMS and FARCOAST. However, the run time on the local machines was too long for running FarCoast800. With the acquisition of more computing power, this work has laid the foundation for future ocean modeling in the Faroe Islands.

References

1. Arakawa, A., & Lamb, V. R. (1977). Computational Design of the Basic Dynamical Processes of the UCLA General Circulation Model. In J. Chang (Ed.), *Methods in Computational Physics: Advances in Research and Applications* (Vol. 17, pp. 173-265). Elsevier. https://doi.org/https://doi.org/10.1016/B978-0-12-460817-7.50009-4
2. Arneborg, L. (2004). Turnover times for the water above sill level in Gullmar Fjord. *Cont. Shelf Res.*, *24*, 443-460. https://doi.org/10.1016/j.csr.2003.12.005
3. Asplin, L., Albretsen, J., Johnsen, I. A., & Sandvik, A. D. (2020). The hydrodynamic foundation for salmon lice dispersion modeling along the Norwegian coast. *Ocean Dynamics*, *70*(8), 1151-1167.
4. Cushman-Roisin, B., & Beckers, J.-M. (2011). Introduction to geophysical fluid dynamics: physical and numerical aspects. Academic press.
5. Doodson, A. T., & Lamb, H. (1921). The harmonic development of the tide-generating potential. Proceedings of the Royal Society of London. Series A, Containing Papers of a Mathematical and Physical Character, 100(704), 305-329. https://doi.org/doi:10.1098/rspa.1921.0088
6. Durran, D. R. (2013). Numerical methods for wave equations in geophysical fluid dynamics (Vol. 32). Springer Science & Business Media.
7. Eliasen, S. K., Hátún, H., Larsen, K. M. H., Hansen, B., & Rasmussen, T. A. S. (2017). Phenologically distinct phytoplankton regions on the Faroe Shelf-identified by satellite data, in-situ observations and model. *Journal of Marine Systems*, *169*, 99-110.
8. Farmer, D., & Freeland, H. (1983). The physical oceanography of fjords. *Prog. Oceanogr.*, *12*, 147-219. https://doi.org/10.1016/0079-6611(83)90004-6
9. Foreman, M. G. G., & Henry, R. F. (1989). The harmonic analysis of tidal model time series. *Advances in Water Resources*, *12*(3), 109-120. https://doi.org/https://doi.org/10.1016/0309-1708(89)90017-1
10. Godin, G. (1972). *The Analysis of Tides*. University of Toronto Press. https://books.google.com/books?id=rxUIAQAAIAAJ
11. Haidvogel, D. B., Arango, H., Budgell, W. P., Cornuelle, B. D., Curchitser, E., Di Lorenzo, E., Fennel, K., Geyer, W. R., Hermann, A. J., & Lanerolle, L. (2008). Ocean forecasting in terrain-following coordinates: Formulation and skill assessment of the Regional Ocean Modeling System. *Journal of Computational Physics*, *227*(7), 3595-3624.
12. Hansen, B. (1978). Sea level variations and currents on the Faroe Plateau and their relation to the hydrography University of Copenhagen].
13. Hansen, B. (1990). Oxygentrot og útskifting í botnvatninum á Føroyskum gáttarfirðum. Fiskirannspknir_6.pdf
14. Hansen, B. (2000). *Havið*. Nám.

15. Hedstrøm, K. (2018). Technical Manual for a Coupled Sea-Ice/Ocean Circulation Model (Version 5).

16. Inall, M. E., & Gillibrand, P. A. (2010). The physics of mid-latitude fjords: A review. *Geol. Soc. London Spec. Publ.*, *344*, 17-33. https://doi.org/10.1144/sp344.3

17. Jackson, R. H., & Straneo, F. (2016). Heat, salt, and freshwater budgets for a glacial fjord in Greenland. *J. Phys. Oceanogr.*, *46*, 2735-2768. https://doi.org/10.1175/jpo-d-15-0134.1

18. Jacobsen, H. (2020). Úr eyga til varandi aling.

19. Larsen, K. M. H., Hansen, B., & Svendsen, H. (2008). Faroe Shelf Water. *Continental Shelf Research*, *28*(14), 1754-1768. https://doi.org/https://doi.org/10.1016/j.csr.2008.04.006

20. Larsen, K. M. H., Hansen, B., & Svendsen, H. (2009). The Faroe shelf front: Properties and exchange. *Journal of Marine Systems*, *78*(1), 9-17.

21. Lien, V., Gusdal, Y., Albretsen, J., Melsom, A., & Vikebø, F. (2013). Evaluation of a Nordic Seas 4 km numerical ocean model hindcast archive (SVIM), 1960-2011. *Fisken og Havet*, *7*, 1-80.

22. Marchesiello, P., Debreu, L., & Couvelard, X. (2009). Spurious diapycnal mixing in terrain-following coordinate models: The problem and a solution. *Ocean Modelling*, *26*(3), 156-169. https://doi.org/https://doi.org/10.1016/j.ocemod.2008.09.004

23. Marchesiello, P., McWilliams, J. C., & Shchepetkin, A. (2001). Open boundary conditions for long-term integration of regional oceanic models. *Ocean Modelling*, *3*(1), 1-20. https://doi.org/https://doi.org/10.1016/S1463-5003(00)00013-5

24. Myksvoll, M. S., Sandvik, A. D., Skarðhamar, J., & Sundby, S. (2012). Importance of high resolution wind forcing on eddy activity and particle dispersion in a Norwegian fjord. *Estuarine, Coastal and Shelf Science*, *113*, 293-304. https://doi.org/https://doi.org/10.1016/j.ecss.2012.08.019

25. Pawlowicz, R., Beardsley, B., & Lentz, S. (2002). Classical tidal harmonic analysis including error estimates in MATLAB using T_TIDE. *Computers & Geosciences*, *28*(8), 929-937. https://doi.org/https://doi.org/10.1016/S0098-3004(02)00013-4

26. Pugh, D., & Woodworth, P. (2014). Sea-Level Science: Understanding Tides, Surges, Tsunamis and Mean Sea-Level Changes. Cambridge University Press. https://doi.org/DOI: 10.1017/CBO9781139235778

27. Shchepetkin, A. F., & McWilliams, J. C. (2005). The regional oceanic modeling system (ROMS): a split-explicit, free-surface, topography-following-coordinate oceanic model. *Ocean Modelling*, *9*(4), 347-404. https://doi.org/https://doi.org/10.1016/j.ocemod.2004.08.002

28. Simpson, J. H., & Sharples, J. (2012). *Introduction to the Physical and Biological Oceanography of Shelf Seas*. Cambridge University Press. https://doi.org/DOI: 10.1017/CBO9781139034098

29. Stigebrandt, A. (1981). A mechanism governing the estuarine circulation in deep, strongly stratified fjords. *Estuarine Coastal Shelf Sci.*, *13*, 197-211. https://doi.org/10.1016/s0302-3524(81)80076-x

30. Umlauf, L., & Burchard, H. (2003). A generic length-scale equation for geophysical turbulence models. *Journal of Marine Research*, *61*(2), 235-265.

Paper I

Erenbjerg, S. V., Albretsen, J., Simonsen, K., Sandvik, A. D., & Kaas, E. (2020). A step towards high resolution modeling of the central Faroe shelf circulation by FarCoast800. Regional Studies in Marine Science, 40, 101475. https://doi.org/https://doi.org/10.1016/j.rsma.2020.101475

I

Regional Studies in Marine Science 40 (2020) 101475

Contents lists available at ScienceDirect

Regional Studies in Marine Science

journal homepage: www.elsevier.com/locate/rsma

A step towards high resolution modeling of the central Faroe shelf circulation by FarCoast800

Sissal V. Erenbjerg [a,c,*], Jon Albretsen [d], Knud Simonsen [a,b], Anne D. Sandvik [d], Eigil Kaas [c]

[a] Fiskaaling - Aquaculture Research Station of the Faroes, við Áir 11, FO-430 Hvalvík, Faroe Islands
[b] University of the Faroe Islands, J. C. Svabosgøta 14, FO-100 Tórshavn, Faroe Islands
[c] Niels Bohr Institute, Copenhagen University, Juliane Maries Vei 30, DK-2100 Copenhagen, Denmark
[d] Institute of Marine Research, P.O. box 1870 Nordnes, NO-5817, Bergen, Norway

ARTICLE INFO

Article history:
Received 31 January 2020
Received in revised form 1 September 2020
Accepted 17 September 2020
Available online 9 October 2020

Keywords:
North Atlantic
Faroe shelf
Circulation
Numerical modeling
Aquaculture

ABSTRACT

This paper describes the FarCoast800 model setup for the Faroe shelf and the validation towards observations. We found that the circulation was in accordance with observations on the shelf and the upper ∼500m of the water column, away from the lateral boundaries. Furthermore, we found high correlations between the model and observations for the on-shelf water, in particular for short-term variations of temperature, demonstrating the importance of high resolution atmospheric forcing. A main challenge for this study was the lateral boundary conditions at all four open boundaries in the varying and steep bathymetry of the FarCoast800 model setup. We also investigated the origin of water reaching the different areas of the shelf. Notably our results indicated intrusion of water originating from the East Icelandic Current into the deeper areas on the eastern part of the Faroe shelf.

Our long term motivation of the study was to investigate the capability of the model to drive an even higher resolution ROMS model setup for the central Faroe shelf, enabling the resolution of processes on a 100m scale or less. The study concludes that FarCoast800 can drive a high-resolution nested model area on the Faroe shelf.

Here we present a Regional Ocean Model System (ROMS) model setup for the Faroe shelf with a horizontal resolution of 800m x 800m and 35 vertical layers. The model setup is forced by a high resolution atmospheric model, and forced by a 4km x 4km horizontal resolution version of the ROMS model on the lateral boundaries. We name our model setup FarCoast800. The model setup was run for the entire sample year 2013.

1. Introduction

The Faroe Islands is an archipelago located in the Northeast Atlantic Ocean (Fig. 1). The greatest contribution to the economy is from the ocean, through the off-shore fishery and the fish farms located in the fjords and straits (Dam, 2019). This increases the interest towards understanding the circulation on the shelf in relation to both ecology on the shelf, and dispersion between the fish farming sites. The long term strategic goal of our work has been to assist studies on matters regarding fish farming through providing helpful scientific knowledge for the industry of fish farming.

The central location of the Faroe Islands on the Greenland–Scotland Ridge (Fig. 1 and Section 2), ensures that the area is included in a large number of numerical circulation models on the ocean exchange between the Atlantic Ocean and the Arctic Ocean. Nonetheless the efforts to investigate the water properties and circulation more locally on the Faroe shelf by the means of numerical models are still limited, with only two prior model setups. The first model study by Rasmussen et al. (2014) uses a modified version of the 3D HYbrid Coordinate Ocean Model (HYCOM) (Chassignet et al., 2007), with a horizontal resolution ranging from 750–1300 m in a hindcast run for the years from 2000 to 2009. The study of Rasmussen et al. (2014) quantifies the exchange of the shelf water mass, and explains the processes controlling the variability between years of the Faroe shelf spring bloom. The second model study by Kragesteen et al. (2018) and Patursson et al. (2017) uses results from a 2D numerical tidal model with a spatial resolution of 100 m, to identify the significant contribution of the tidal currents and the residual currents generated by tidal rectification in dispersion of parasites between fish farming sites.

For the atmosphere in windy and mountainous areas like the Faroe Islands, the large scale wind flow is highly modified by the local topography. The wind forcing on the upper

* Corresponding author at: Fiskaaling - Aquaculture Research Station of the Faroes, við Áir, FO-430 Hvalvík, Faroe Islands.
E-mail address: sissal@fiskaaling.fo (S.V. Erenbjerg).

https://doi.org/10.1016/j.rsma.2020.101475

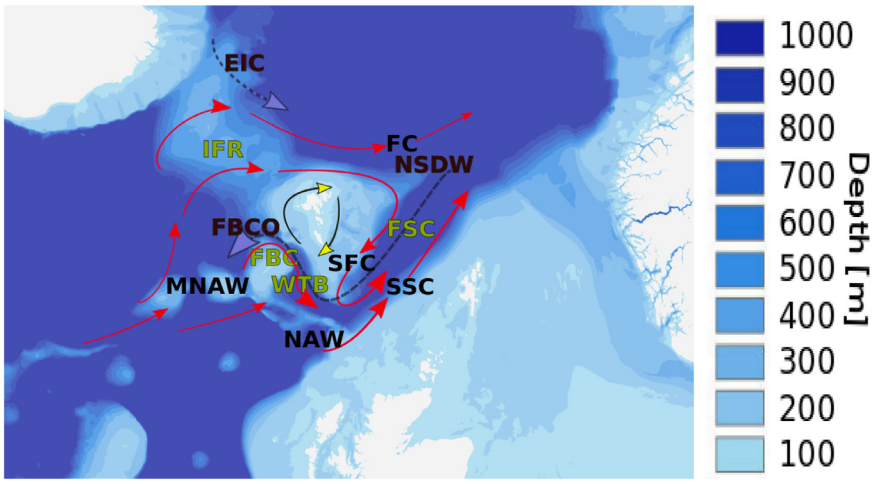

Fig. 1. Bathymetry of the area and schematic arrows of the main flow pathways. Continuous arrows indicate flow of Modified North Atlantic Water (MNAW) and North Atlantic Water (NAW) in the upper layers (red), the cold Norwegian Seas Deep Water (NSDW) (purple), the colder and fresh East Icelandic Current (EIC) (purple) and the clockwise residual current on the shelf (yellow). The other abbreviations are the Faroe Bank Channel (FBC), the Faroe Bank Channel Overflow (FBCO), the Wyville Thomsen Basin (WTB), the Faroe Shetland Channel (FSC), the Iceland Faroe Ridge (IFR), Faroe Current (FC), South Faroe Current (SFC) and Scottish Slope Current (SSC). Redrawn from Larsen et al. (2009) and Hansen et al. (2017). Map is by courtesy of Anders Nygård (ArcGIS). (For interpretation of the references to color in this figure legend, the reader is referred to the web version of this article.)

ocean has a large spatial and temporal variability. High resolution atmospheric forcing is important for distributing the precipitation correctly in mountainous areas (lee and lo side of mountains), and inclusion of high quality atmospheric forcing will increase the ability to simulate the ocean circulation in a realistic way (Myksvoll et al., 2012; Skogseth et al., 2007).

To represent the circulation in a complex bathymetry a 3D dynamical ocean model is imperative. However, Forcing a high-resolution coastal model from all geographical directions demands good precision on the offshore model, as biases will propagate towards the coast. One ocean model that has been proven effective for regions with many fjords and highly varying and steep bathymetry, such as our model domain (Section 2), is the Regional Ocean Model System (ROMS) (Shchepetkin and McWilliams, 2005), such as it is applied for the Norwegian coast in the NorKyst800 model setup (Lien et al., 2013).

Here we adapt the NorKyst800 model setup, see e.g. applications in Huserbråten et al. (2018) and Myksvoll et al. (2018) with 800 m × 800 m resolution and 35 vertical layers to the Faroe shelf, aiming at providing further insight into the general circulation on the Faroe shelf and providing validated boundary conditions for future higher resolution simulations of the central shelf and coastal regions.

A summary of present knowledge of the relatively complex circulation in the region is provided in Section 2. The model setup, applied forcing and simulation is described in Section 3.1, and observed data sets for validation are presented in Section 3.4. The model output and validation towards observations are provided in Section 4, which is followed by a discussion in Section 5 and concluding remarks in Section 6.

2. Hydrographic area description

The ocean surrounding the Faroe Islands (Fig. 1) is for the off-shelf waters, in the upper layers dominated by water of Atlantic origin (Larsen et al., 2008, 2009; Hansen and Østerhus, 2007; Hansen et al., 2017). The water entering the area from the west is traditionally termed Modified North Atlantic Water (MNAW), while to the south over the Scottish slope the warmer and more saline North Atlantic Water (NAW) is carried by the Scottish Slope Current (SSC) (Hansen et al., 2017). In the open northwest Atlantic the MNAW splits into two branches. One branch flows over the banks to the southwest towards the Faroe Shetland Channel (FSC), where it joins the SSC. The other branch is flowing north of the Faroe Islands, after crossing the Iceland Faroe Ridge (IFR) between the Faroe Islands and Iceland, it becomes focused into the narrow Faroe Current (FC) north of the Faroe Islands (Hansen et al., 2017). On the eastern slope of the Faroe Bank (FB) there is a southward flowing branch of MNAW, which either joins the MNAW water in the Wyville Thomson Basin (WTB) (Fig. 1), or is recirculated in the Faroe Bank Channel (FBC) and flows northward again along the western Faroe shelf (Hansen et al., 2017).

Northeast of the Faroe Islands the MNAW continues northeastward into the Norwegian Sea, but a branch turns southward along the eastern flank of the Faroe shelf and is retroflected eastward in the FSC. This southwestward flow along the eastern slope of the Faroe shelf is named the Southern Faroe Current (SFC) by Hátún (2004). The strength of these two branches may vary (Hátún et al., 2005).

To the north the fresher and colder water of Arctic origin is transported towards the area east of IFR by the East Icelandic Current (EIC) (Beaird et al., 2016). Approaching the Faroe shelf, this water is overlaid by the warmer and more saline water of Atlantic origin, but is leaning towards the shelf slope to the north and is flowing southwards along the slope of the eastern shelf (Hansen et al., 2010). Along its path it is diluted by the surrounding water, and it is generally considered to reflect eastward in the FSC, although traces of this water are also seen as an intermediate layer in the out-flowing water in the FBC (Hansen and Østerhus, 2000; Ullgren et al., 2014). The appearance of the EIC water explains the generally slightly colder and fresher water east of the Faroes compared to the western side (Hansen et al., 2017; Hátún, 2004). However, occasional mixing onto Faroe shelf is seen from the more saline and warmer SSC (Larsen et al., 2008).

The deeper layers are dominated by the relatively cold and fresh Norwegian Sea Deep Water (NSDW), which fills up the deeper part of the Norwegian Sea Basin to the east of the Faroe Islands. This modified NSDW flows through FSC to the south and continuous through WTB to the FBC as the Faroe Bank Channel Overflow (FBCO) west of the Faroe shelf, contributing to the North Atlantic Deep Water (NADW) formation (Hansen et al., 2016, 2017).

The on-shelf waters consist of a mixture of the surrounding waters (Larsen et al., 2008) and is characterized by relatively

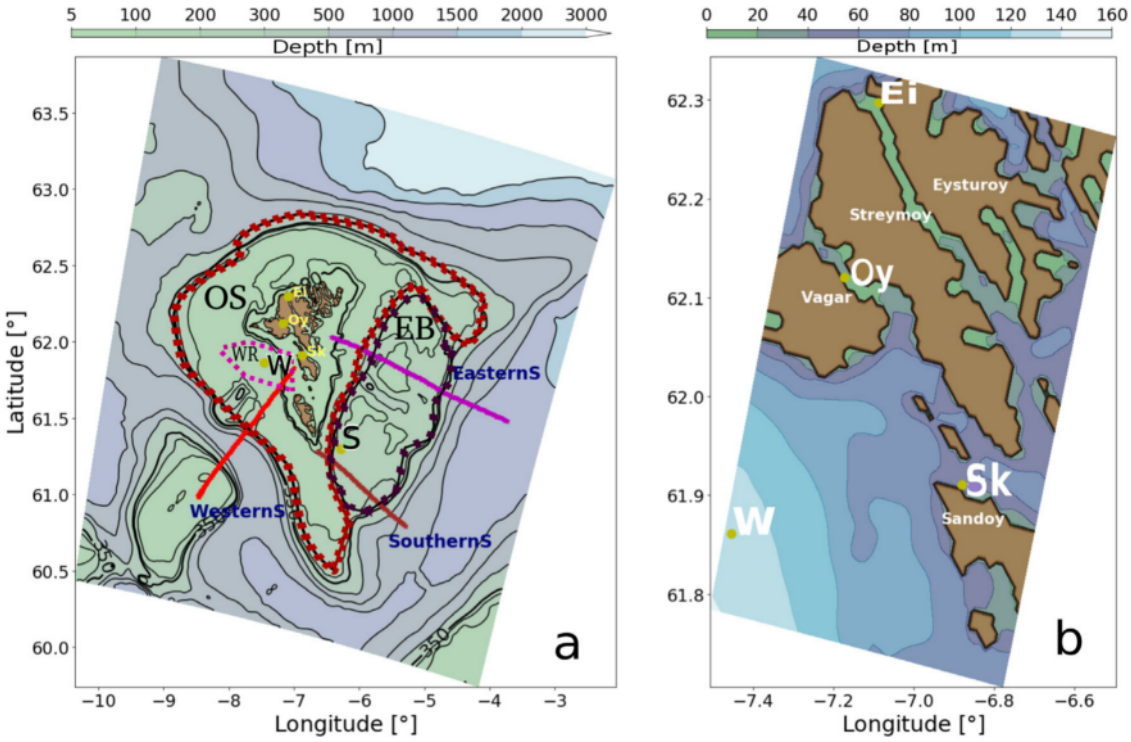

Fig. 2. **a**: The Faroe shelf and the model domain. The black thin lines shows the bottom contours for 50 m, 100 m, 300 m, 500 m, 700 m, 1000 m, 1500 m, 2000 m, 3000 m. (1) The thick red line WesternS indicates the positions of the hydrographic section from the Faroe Shelf at 61.8°N 7.0°W westwards through the FBC out to the FB at 61.0°N 8.5°W. The thick purple line EasternS indicates the positions of the hydrographic section from the Faroe shelf at 62.0°N 6.4°W eastwards of the Faroe shelf into the FSC to the east at 61.5°N 3.7°W . (2) The stations (see text) by letters W and S are locations of timeseries on the OS depth greater 100 m. The stations (see text) Ei, Oy and Sk are locations of coastal timeseries depth less than 100 m. (3) The three areas OS (red broken line), WR (pink broken line) and EB (purple broken line) are largely redrawn from Eliasen et al. (2017b). **b**: Zoom on the locations of the coastal stations Ei, Oy and Sk as well as the bathymetry. (For interpretation of the references to color in this figure legend, the reader is referred to the web version of this article.)

strong tidal currents with clockwise residual currents around the islands (Larsen et al., 2008; Kragesteen et al., 2018). Moreover the on-shelf waters are divided into three domains based on ocean dynamics (Eliasen et al., 2019; Larsen et al., 2008, 2009) and phytoplankton variability (Fig. 2) (Eliasen et al., 2017a, 2019). The Central Shelf (CS) is separated from the rest of the water on the shelf by a tidal front at the ∼100–150 m depth contour named the Faroe Shelf Front (FSF) and is permanently well mixed due to the relatively strong tidal currents (Larsen et al., 2009). Studies of the abundance and timing of blooming of phytoplankton (Eliasen et al., 2017a, 2019) shows that CS has different characteristics than the remaining shelf, which may be divided into two additional separate areas. One area covering the banks on the eastern shelf, the Eastern Banks (EB) (Fig. 2) and the remaining Outer Shelf (OS). The highest averages and variances in chlorophyll concentrations are found in a region on the western side of the shelf, termed Western Region (WR), and the entire OS varies similar to WR (Eliasen et al., 2017a). The different phytoplankton phenology in these three distinct areas on the shelf is also reflected in the variability of zooplankton (Jacobsen et al., 2018).

From the influence of the relatively warm MNAW, which embeds the Faroe shelf, the atmosphere cools the ocean the entire year except for the high summer months. This cooling is most effective in the shallower and permanently mixed CS, and is reflected in a ∼1 °C lower temperature (Larsen et al., 2009). Also, the CS has ∼0.1 psu fresher water than in OS, which is explained to be due to enhanced precipitation because of orographical effects on the islands (Larsen et al., 2009). The residence time is 1–2 months, but is likely highly variable (Larsen et al., 2009; Rasmussen et al., 2014; Eliasen et al., 2016). The separation of the on-shelf waters and the surrounding open ocean waters, as well as the separation of the on-shelf water into the CS and OS are crucial for the ecology in the area and significant in the recruitment of several commercial important fish stocks (Larsen et al., 2008; Eliasen et al., 2017a, 2019; Jacobsen et al., 2018). This separation plays a significant role in maintaining drift particles, including sea lice, within the CS and a better understanding of the circulation on the shelf is crucial in developing models and strategies for management of the local aquaculture industry (Kragesteen et al., 2018).

3. Material and methods

3.1. The FarCoast800 model

The ROMS model setup applying 800 m × 800 m horizontal resolution around the Faroe shelf, hereafter named FarCoast800, was originally adapted from the Norwegian Coastal model, NorKyst800 applying the same resolution. Such coastal model systems are developed as a compromise between geographical extension of the model domain and sufficient grid resolution to provide realistic hydrodynamic information of coastal zones. Our version covers the entire Faroe Shelf and the Faroe Bank to the west of the Faroes and extends into the deep water surrounding the area to the east, north and west, and the Scottish shelf to the south (Fig. 2a). Our main interests are the shallower regions, above the 350 meter contour line in Fig. 2a. FarCoast800 is implemented using ROMS as the hydrodynamic model (e.g. Shchepetkin and McWilliams (2005) and Haidvogel et al. (2008) , or see http://myroms.org). ROMS is a state-of-the-art, three-dimensional, free-surface, primitive equation numerical ocean model using a generalized terrain-following s-coordinate in

the vertical. The FarCoast800 model applies 35 vertical levels and was set up with enhanced resolution in the upper ∼50 m.

The Chapman boundary condition (Chapman, 1985) was used for the free-surface boundary condition and the lateral boundary condition by Flather (1976)) was applied for the barotropic velocity. As described by Marchesiello et al. (2001) and as applied in our model set-up, ROMS has an option for providing radiation conditions on outflow and nudging to a known exterior value on inflow for 3D momentum and tracers. This is here implemented as a variation on the radiation condition, requiring two timescales, namely the inflow nudging timescale and the outflow nudging timescale. Here, the nudging on inflow was 120 times larger than on the outflow. For vertical turbulence, the local closure scheme was based on the Generic Length Scale (GLS) parameterization (Umlauf and Burchard, 2003).

Lateral boundary conditions and initial fields conditions are retrieved from the Nordic Seas 4 km numerical ocean model hindcast archive (SVIM), which covers the area from the North Atlantic west of Ireland, the Nordic Seas and into the Arctic to the north and is described in Lien et al. (2013). Note that the boundaries in the SVIM-model after 2009 applied monthly climatological values of currents and hydrography, as the provider, the Simple Ocean Data Assimilation set (SODA; Carton et al., 2000; Carton and Giese, 2008) was released with a final simulation date in 2009 (version 3.6.1). The years of SODA fields aggregated to force the SVIM model are 2000–08. This implies that the open boundaries in the FarCoast800 simulation applied monthly climatological external forcing as input and then mainly resolved the seasonal variability only. The tidal forcing was applied along the open boundaries and interpolated from the global TPXO7.2 (Egbert and Erofeeva, 2002).

The simulation was initialized January 1st, 2013 from SVIM 4 km state and was run for one year until December 31st, 2013. The first 1–2 months should then be considered as a spin-up period.

3.2. Atmospheric forcing, WRF

The atmospheric forcing is obtained from simulations with the Weather Research and Forecasting (WRF) model (WRF, http://www.wrf-model.org/) The model was configured with horizontal grid resolutions of 9-3-1 km, where the 1 km resolution domain covered the area of interest and was used as forcing for the ocean model. See Myksvoll et al. (2012) for more details on the configuration.

3.3. Fresh water forcing, rivers

River runoff is neglected except for the runoff into the strait between two largest islands, Streymoy and Eysturoy (Fig. 2 right), where the river runoff is estimated from various freshwater gauges (courtesy to the local energy producer, SEV) and the orographic model by Davidsen et al. (1994).

3.4. Observed data

3.4.1. Hydrographic sections

The Faroe Marine Research Institute (FAMRI) runs a monitoring program, which includes regular hydrographic surveys 2–4 times per year along standard sections radiating from the islands and into the deep waters east, north, west and south of the Faroe shelf. Here we compare with the western section (Fig. 2a) which intersects the FBC and FB to the west and has hydrographic data available from cruises in February, May and August/September 2013. We also compare with the section across the eastern shelf from cruises in February and May 2013, and, since the eastern section was not done on the August/September cruise, we compare to the southern section in August/September 2013.

3.4.2. Temperature and salinity time series

The location of the three coastal stations are shown in Fig. 2a and b as Ei, Oy and Sk. Temperature is acquired at all stations, while salinity is only available at station Sk.

At station Sk water is pumped from 18 m depth in a tidally well mixed strait. Salinity samples are taken every 4–7 day (since 1997) by FAMRI (www.hav.fo) (Larsen et al., 2008). Temperature at station Sk is measured every 5 min. FAMRI have operated the tidal-gauge station Oy every 30 min since 1991 (Larsen et al., 2008). The remaining coastal station Ei is a tidal-gauge station located in the harbor and operated by the Office for Public Works (OPW) (www.landsverk.fo).

Stations W and S (Fig. 2a) are temperature loggers mounted close to the bottom and at 5 m depth, operated by FAMRI, on the moorings on semi-permanent wave-riders operated by OPW (Eliasen et al., 2017a).

4. Results and comparison with observations

In this section the model results are described and compared with observations. Our main interest is the circulation on the shelf, however, the off-shelf circulation is important for the on-shelf circulation. Thus the model performance for the water surrounding the shelf, is described prior to the model results for the outer and inner shelf respectively. Due to the limitation of observations and our sample year only running through 2013, we also included results from February, with care, despite this is considered part of the spin-up period.

4.1. Ocean currents in FarCoast800

The annual barotropic flow is shown in Fig. 3. Here, as expected from the literature and presented in Fig. 1: The MNAW bifurcates prior to the FB. One branch travels northward and continues along the northern edge of the Faroe shelf as part of the FC. North–northeast of the Faroe shelf at 63°N and 5°W the FC bifurcates and a well defined flow follows the bathymetry southwards in agreement with the velocity estimates obtained for the upper 100 m from a ferry mounted acoustic Doppler current profiler (ADCP) by Rossby and Flagg (2012). Entering the FSC the majority of this flow is recirculated into the SSC, as suggested by Hansen et al. (2017, e.g). However, the innermost fraction of the flow is crossing the southern tip of the shelf and continues northward along the shelf edge on the western side of the islands. The SSC is evident in the southern part of the model domain in congruence with Rossby and Flagg (2012). From the square at 60°N-61°N and 5°W-7°W, it appears that the SSC is partly fed by NAW from the boundary conditions to the south, but also with the other, southward traveling, branch of the MNAW bifurcating prior to the FB. The southward traveling branch along the FB, is strongly dominated by high velocities in the upper layers (Figs. 4d and S2). This is not in accordance with Hansen and Østerhus (2007). The main contribution to the mean annual barotropic flow is from the upper layers (Figure S2). The bottom layers have EIC water along the IFR from the north and the NSDW from the northeast (Figs. 8, 9 and S3) as expected from Fig. 1.

The spurious boundary currents to the north and northeast of the model domain are not appearing in the 4 km × 4 km model forcing (Figure S1), suggesting this to be a boundary condition artifact in the current model set-up.

4.2. Off-shelf water properties

Seasonal means of temperature, salinity, density and velocity along the hydrographic standard sections west and east of the shelf (WesternS and EasternS in Fig. 2a) are extracted from the model simulations following the validation approach by Rasmussen et al. (2014).

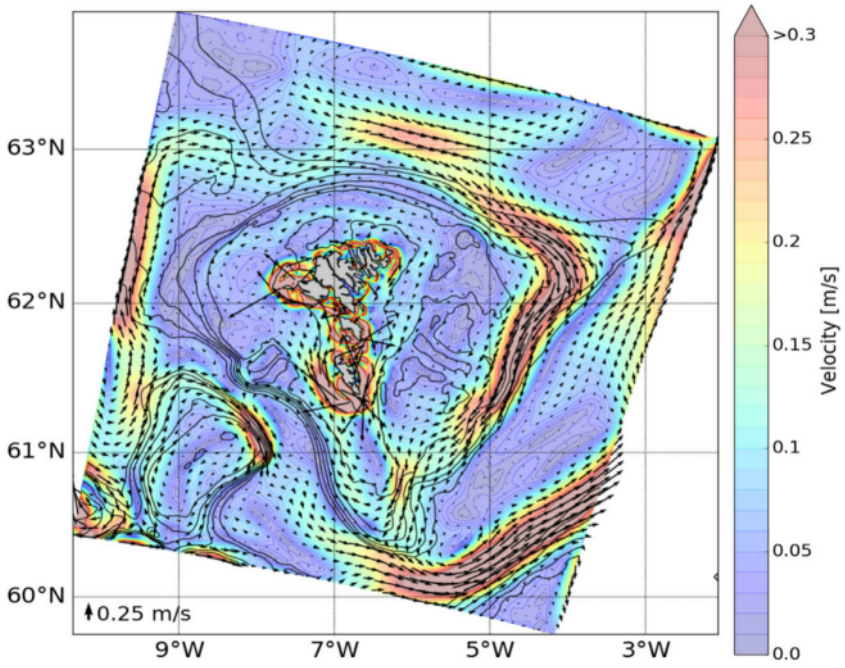

Fig. 3. Modeled annual mean barotropic flow. The colors indicate the speed (m/s), the velocity is given by the arrows. The speed is the length of the arrows.

4.2.1. Off the western shelf

The WesternS section (Fig. 2a) begins near land off the coast of the island Sandoy (Fig. 2b), and traverses the western shelf, the FBC and ends on the FB. This section is ∼120 km long and the deepest point in the section is 870 m deep around 8°W (Fig. 4).

Seasonal average temperature from June, July and August (JJA) is shown in Fig. 4a. The temperature gradients, down to ∼600 m, are tilting towards the shelf, as expected from geostrophy (Margules equation), during all seasons (Figure S4). Around 600–700 m depth the temperature isotherms are flattening and the water colder than one degree has a horizontal contour line. This is in accordance with Hansen and Østerhus (2007) and Hansen et al. (2017). Furthermore, we identify the water warmer than 7 °C depicted in Fig. 4a to be MNAW as do Hansen and Østerhus (2007).

The annual modeled mean temperature in the bottom layer in the FBC is 0.3 °C. This is warmer than the running 3-year average bottom temperature for the year 2013 of about -0.35 °C in the almost continues recordings from 1995–2015 by Hansen et al. (2016). Over the span of the record there is an increase in the bottom temperature of the order of 0.1 °C (Hansen et al., 2016). The model temperature variation in the deepest part of the FBC has a bias of up to 0.8 °C compared to what was seen in the observations for the year 2013 (Hansen et al., 2016).

Salinity in JJA at SectionW (Fig. 4b) has the same trend as the temperature in the intermediate part of the water column. Here, again the gradient lines are tilting towards the Faroe shelf. The MNAW is the more saline water (35.15<) and the NSDW is the less saline (35.0>) water in the deeper part of FBC in accordance with Hansen and Østerhus (2007) and Hansen et al. (2016, 2017). When comparing daily mean with the cruise data (Figs. 7 and 9) it is clear that the salinity levels are slightly underestimated, but the main structures are still captured for the westernS all plots.

Density is shown in Fig. 4c. The density generally follows the temperature structure from Fig. 4a in the upper part and both the salinity and temperature structure in the lower part. Again the isolines are tilting towards the Faroe shelf. The density is calculated from temperature and salinity and is thus affected by the biases in both temperature and salinity.

The northward velocity component, is shown in Fig. 4d for JJA, and the FBCO is recognized as the northward current in the model simulation below 600 m depth. Maximum values of the FBCO are along the flank of FB, decreasing towards the Faroe shelf, as expected from potential vorticity conservation (Hansen and Østerhus, 2007). There is a weak seasonal variation in the overflow, which in our model is weakest during JJA and strongest in MAM (Figure S9), which is out of phase with the observations showing maximum current in August and minimum in February (Hansen et al., 2016). We also see a short period during July in the model simulation were the FBCO is going in the opposite direction, contributing to the low average northward velocity during JJA (∼0.1 m/s). This is likely a constrain from boundary conditions (Figure not shown).

Along the upper eastern flank of the FB, a divaricate of the MNAW persist as a strong southward flow (Fig. 4d) during all seasons. In the model simulation this flow has a seasonal variation and is strongest in the summer months (Figure S9). This branch mainly contributes to the SSC, yet a small fraction of the easternmost water mass seems to be recirculated and continues northward along the western Faroe shelf (Fig. 4d at −7.8°W and Fig. 3).

4.2.2. Off the eastern shelf

The section EasternS (Fig. 2a) is across the eastern shelf. It begins near the island Eysturoy (Fig. 2b) and traverses the EB, continuing into the mid FSC. The maximum depth is 1245 m (Fig. 5).

In the FSC the deep water (>800 m) is dominated by NSDW with temperatures below 0.0 °C, and salinity less than 34.94 (Fig. 5a,b); with minimum seasonal temperature average in the bottom layer of approximately -0.4 °C during all seasons. This is in agreement with observations (Hansen et al., 2017). The current in the deepest part is southward on the Faroe side, and becomes weaker in the central FSC (Fig. 5d). The density isolines follow both the salinity isolines and the temperature isolines in the FSC Fig. 5a,b, and c.

In the intermediate water depth at about 500–800 m, there is a weak salinity minimum during all seasons, with values below

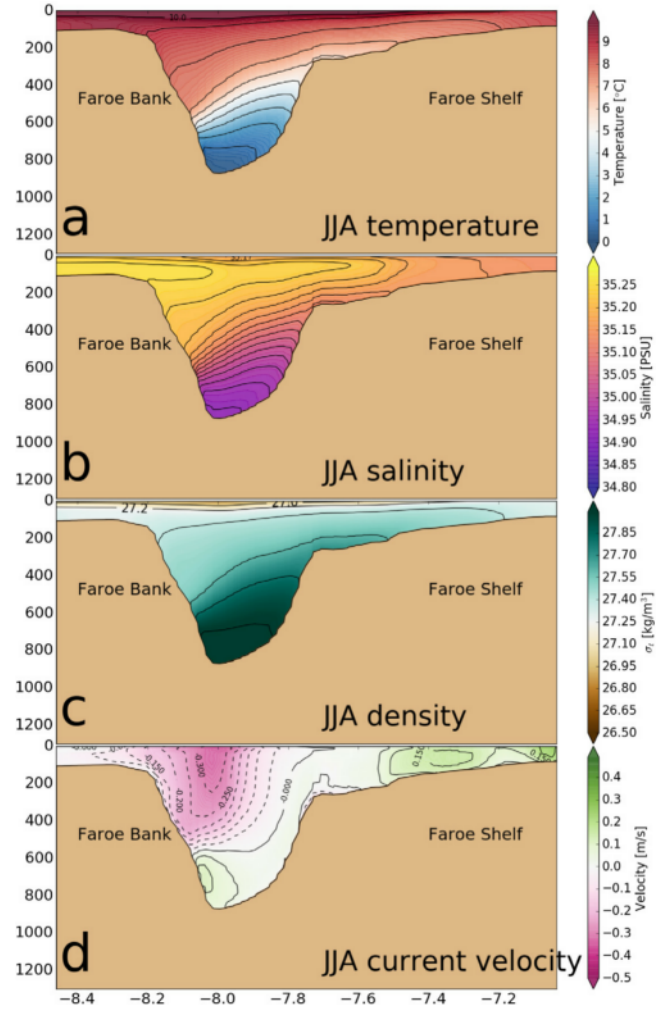

Fig. 4. Modeled average (a) temperature (one °C between lines), (b) salinity (0.025 psu between lines), (c) density (0.2 kg/m^3 between lines) and (d) velocity (northward component, 0.05 m/s between lines) for the June, July, August (JJA) summer season along the western section (WesternS) in Fig. 2. Similar plots for all seasons are available in the supplementary material.

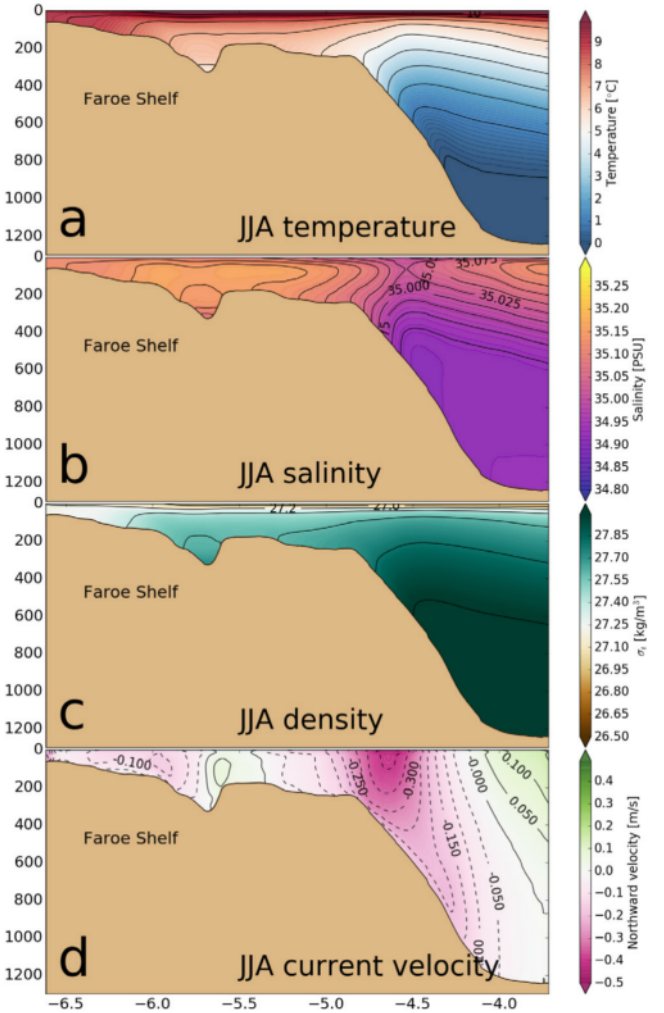

Fig. 5. Modeled average (a) temperature (one °C between lines), (b) salinity (0.025 psu between lines), (c) density (0.2 kg/m^3 between lines) and (d) velocity (northward component, 0.05 m/s between lines) for the June, July, August (JJA) season along the eastern section in Fig. 2. Similar plots for all seasons are available in the supplementary material.

34.92 PSU and a core of fresher water against the shelf only existing in the JJA and SON average (Figs. 5 and S7) indicating water of Arctic origin (Hansen and Østerhus, 2007; McKenna et al., 2016). Above the upper part of the Faroe shelf slope at 4.9°W to 4.2°W, the water is in general fresher, colder and flowing southwards (Figs. 5, 8 and 9). Comparing towards the observations (Figs. 8 and 9) the salinity is somewhat too low and the temperature is somewhat too high comparing to the model (Fig. 8c) and (Fig. 9c). Following the horizontal distribution of the temperature at 50 m depth (Figs. 10 and 11) this colder and fresher water seen in this section arrives from north of the Faroes and is thus mostly likely of EIC origin.

During February the temperature and salinity isolines from the model and the observations are tilting in opposite directions from 4.3°W and further east (Figs. 8a,d and 9a,d). This is in the model area where spurious currents occur in Fig. 3 at 4°W, induced by the boundary conditions in our model domain since they are not present in the lateral ocean forcing model domain (Figure S1). For the section during May (Fig. 9b,e), there appears to be a spatial bias where the salinity maximum in the model simulation is located at about 5.0°W the observations have a salinity maximum at 4.8°W.

The upper layers are dominated by MNAW (>7 °C) on the Faroe shelf side in the FSC, and the warmer and saltier NAW on the Scottish side, with some intrusion from below of the fresher and colder EIC above the Faroe shelf slope at ∼4.5°W. The strong summer (JJA) stratification (Fig. 5a,b) in the upper 50 m, breaks down during winter and spring (Figures S7 and S5).

The flow field along the eastern shelf Fig. 5d resembles the results obtained by ferry mounted ADCP by Rossby and Flagg (2012), despite the northward flow in model appears further west than in the study by Rossby and Flagg (2012); this is in the area with spurious currents. The salinity and temperature is in fair accordance with the literature (Hansen and Østerhus, 2007; McKenna et al., 2016; Rossby and Flagg, 2012), although the content of the fresher and colder water appears to be slightly exaggerated in the model and the salinity slightly underestimated as the core of the NAW is about 0.05 PSU below what is observed in Hansen and Østerhus (2007).

4.3. The on-shelf waters

4.3.1. The on-shelf annual mean currents

The annual mean currents from the barotropic flow in the model simulation (Fig. 3) captures the relatively strong clockwise

mean circulation in the coastal areas described amongst other by Larsen et al. (2008) and Rasmussen et al. (2014) and Fig. 1. The relatively strong residual flow around the southern tip of the southern most island towards the west may be noted, where velocities reach up to 0.6 m/s, and currents of similar strength as in Rasmussen et al. (2014). Similar mean velocities are also reached around the westernmost islands in fair agreement with previous numerical simulations (Rasmussen et al., 2014; Kragesteen et al., 2018). This relatively strong residual tidal current largely defines the CS which is within the 90 m contour line. As in Kragesteen et al. (2018) the tidal residual current is distinguishable between a northern, a central and a southern group of islands. The CS appears as areas with same temperature at all shown depths in Fig. 10 and as homogeneous water masses on the shelf in hydrographic sections in Figs. 4–9. The separation into several different areas of tidal residual currents is more obvious in Fig. 11 at 50 m depth.

On the OS there is a generally weaker, mean clockwise flow around the islands, on the order of 0.1 m/s or less, which is comparable with observations (Larsen et al., 2008). The OS tidal residual current is also visible at 7.4°W in Fig. 4d and at 6.1°W in Fig. 5d.

4.3.2. Outer shelf, western region

On the western shelf the model shows well mixed water masses in the CS water. Seen east of 7.2°W in Figs. 4a,b as well as the daily averages in Figs. 6 and 7. West of the CS, from 7.2°W to 7.6°W, which here identifies the FSF, and out to the shelf edge the model indicate more homogeneous water than in the observations in February (during the spin-up period), but the surface stratification develops through the spring in fairly good accordance with the observations (Eliasen et al., 2017b).

The section from the model in February and September are about one degree colder than the observations.

4.3.3. Outer eastern shelf, eastern banks

During winter and spring the water on the eastern shelf is vertically homogeneous (Figs. 8a,b,d,e and 9a,b,d,e), but in summer a surface stratification develops (Figs. 8c,f and 9c,f). It is only in proximity of land west of 6.6°W that the water column is mixed all year round.

Over the bank on the eastern shelf, the model has a small maximum in both salinity and temperature (Figs. 8 and 9a,b,c), which is weakly identifiable in the observations (Figs. 8 and 9d,e,f) and seasonal model mean (Fig. 5a,b and clearer identifiable during the other seasons in supplement Figure S5). Spatial plots of the temperature at 50 m depth (Fig. 10) indicate an inflow of MNAW intruding the eastern region from the FC to the north, in particular in spring and summer (Fig. 10). This water is overlaid by the summer stratification, and less visible at 5 m depth (Figs. 8 and 10). Observing the temperature anomaly in Fig. 11 in February at 5 m and 50 m depth and in June at 50 m depth the intrusion of MNAW occurs at the boundary between the OS and the EB in Fig. 2

In the trench separating EB from the OS at 5.6°W, the model has relatively cold and fresh water (Figs. 8 and 9). This is also seen in the observations, however not visible in the contour plots, since this is only a single station.

The residual current (Figs. 3 and 5d) on the inner part of the eastern shelf is southward, and the region close to the shelf edge is also dominated by southward flow as discussed in Section 4.2.2 in good accordance with the clockwise current described by Hansen and Østerhus (2007) and Larsen et al. (2008, e.g.). However, at the inner edge of the bank on the eastern shelf (5.7°W), the model has a residual northward flow, which is evident in current profiles obtained by ferry crossing this area regularly (Rossby and Flagg, 2012). In the model this current disappears during DJF (Figure S8).

Table 1
Annual temperature averages from observations and model simulation and Pearson correlation coefficient p between observed and modeled temperature anomalies at the three coastal stations.

Annual mean temperatures (°C):			
Station	Sk	Oy	Ei
Observation	8.33	8.32	8.20
Model	7.51	7.52	7.48
Bias	0.82	0.8	0.72
Pearson correlation coefficient (p):			
p	0.995	0.996	0.98

4.4. Seasons on the Faroe shelf

4.4.1. Temporal variations on the shelf

Annual timeseries of the simulated difference between the near bottom and near surface temperature are compared to observations and shown in Fig. 12. As in Eliasen et al. (2017a) the temperature timeseries are used to separate WR and EB (station W and S in Fig. 2). Here the model captures the strong summer stratification on the EB at station S. The model captures fairly well the annual variation, as well as most of the short term variations, although, there is some bias between the observations and the model. For station W the Pearson correlation coefficient is 0.71, the covariance is 0.23 for the period from 3rd of January to 17th of September. For station S the correlation and the covariance are 0.97 and 2.06, respectively.

For the EB the stratification occurs in the beginning of May (Fig. 12a). From Figs. 8 and 9 it is clear that this is the case for the entire EB and not just the local station S. The observations in Fig. 12a indicate a more gradual gradient change in the stratification in May than the model setup reproduces. For the WR the stable stratification occurs later, in June, and is less significant; thus not seen in the section Figs. 6 and 7 until the section from early September.

During the summer season there is a bias of ΔT up to 1 °C on the EB at station S and up to 2 °C on the WR station W (Fig. 12).

4.5. Coastal timeseries

The temperature time series are available from the three coastal stations: Sk, Oy and Ei (Fig. 2). The model displays vertically well mixed water on the CS (Figs. 4–8) through all seasons (Figure S5).

The annual mean temperature in the model is generally about 0.8 °C colder than the observations (Table 1), but this bias varies both with time and spatially (Fig. 13). At the two stations with tidally well mixed water, Oy and Sk (Figs. 13a and b) the model slightly underestimates the temperature in particular in winter, while at the more protected station Ei the bias is more constant throughout the year (Fig. 13c). See location in Fig. 2b.

Comparison with observations at the southernmost islands are similar to the two tidally well mixed stations (Oy and Sk), while comparisons with observations from the islands in the northeast shows a good agreement between model and data in winter, but the model is slightly warmer in summer (not shown).

The capability of the model to simulate the short term variability is investigated by calculating the anomaly between the daily temperature and a monthly 30 day running mean for the three coastal stations (Fig. 14). The model performance at all three coastal stations is quite high as demonstrated by the Pearson correlation coefficient p in Table 1.

At station Sk (Fig. 14a) there is an event in March and one in August where the model under and over-estimates the temperature respectively. Otherwise the model captures the variation to

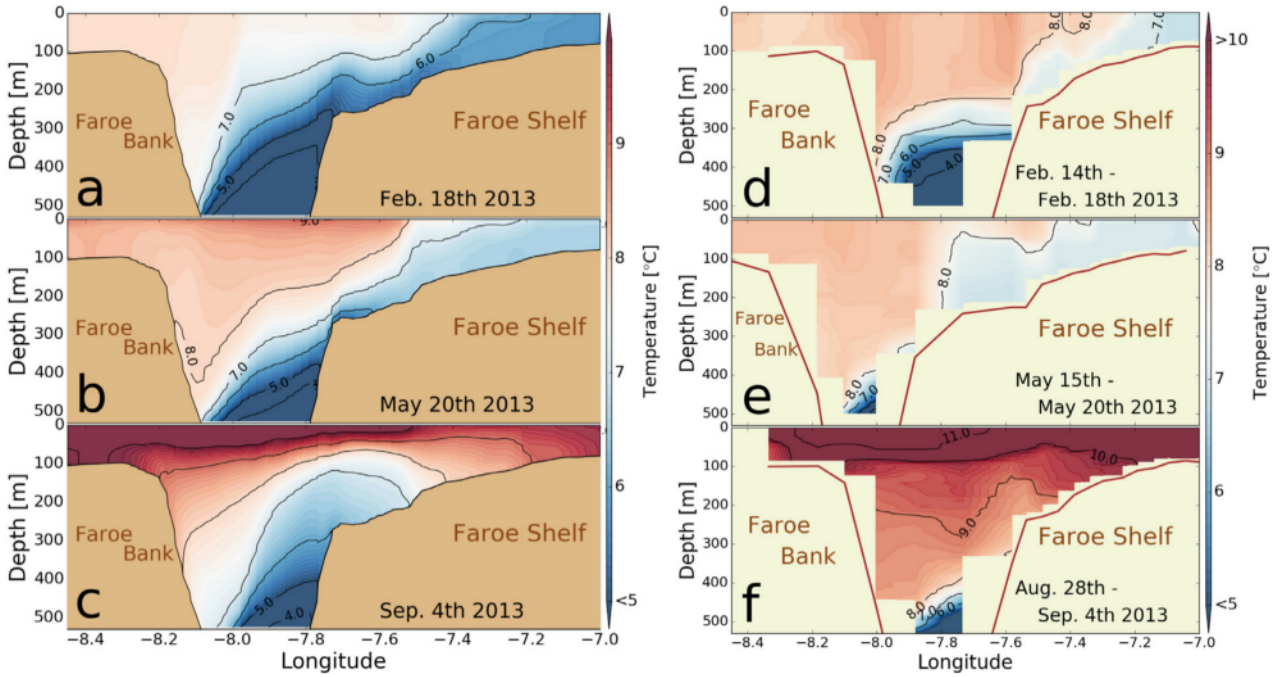

Fig. 6. a,b,c: Daily temperature averages from the model at section WesternS (Fig. 2). d,e,f: Temperature from observations at section WesternS obtained by FAMRI during cruises in February, May and August 2013 (Fig. 2).

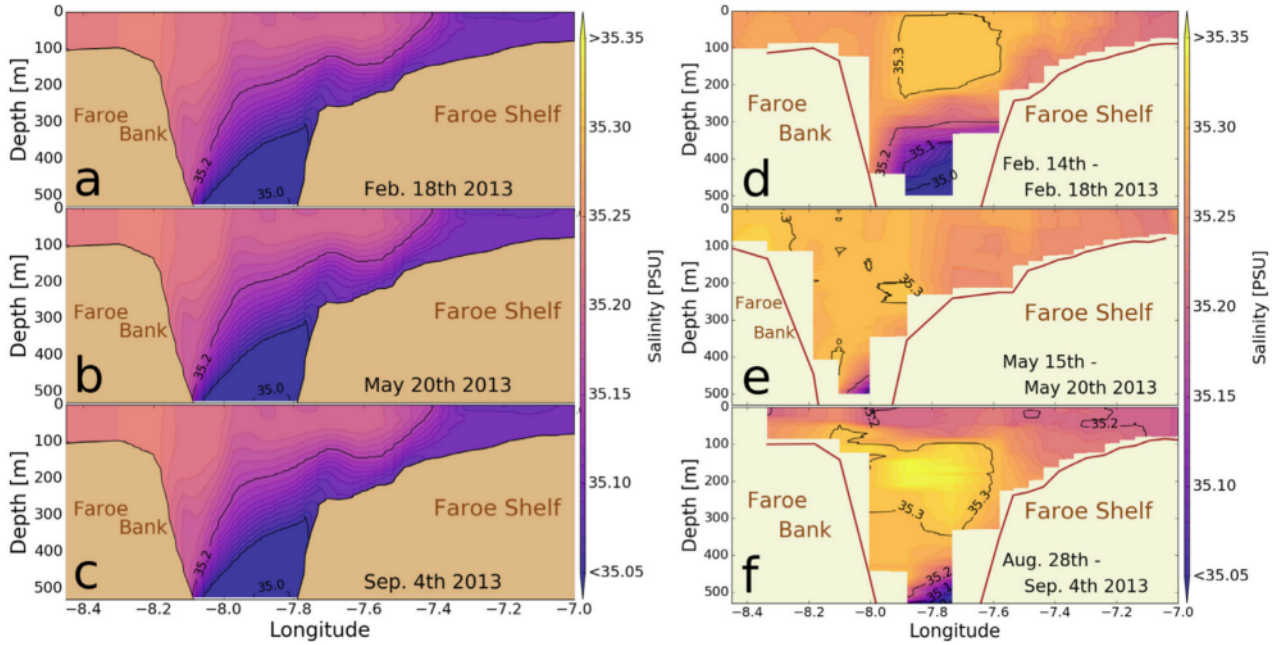

Fig. 7. a,b,c: Daily salinity averages from the model at section WesternS (Fig. 2). d,e,f: Salinity from observations at section WesternS obtained by FAMRI during cruises in February, May and August 2013 (Fig. 2).

a high degree. For the station Oy (Fig. 13b) the discrepancies are even less, there is no significant difference between the model and observed variation. There is a small period in August where the model slightly overestimates the temperature variation.

For station Ei (Fig. 1c) the agreement between model and observations is generally good, except for some low temperature events seen in the observations in the summer months June and July.

Generally, the model underestimates the salinity with 0.02–0.17 PSU when compared to the observations from station Sk, with the largest deviation in the first half year of the simulation (Fig. 16). The lower salinities are also apparent when compared with the hydrographic sections (Figs. 7 and 9).

5. Discussion

The FarCoast800 model setup reproduced the hydrodynamics on and off the Faroe shelf reasonably well. The temperature variations were reproduced with a very high correlation for the coastal stations compared to observations (Table 1). Similarly the current velocities were also well reproduced, and both the inner

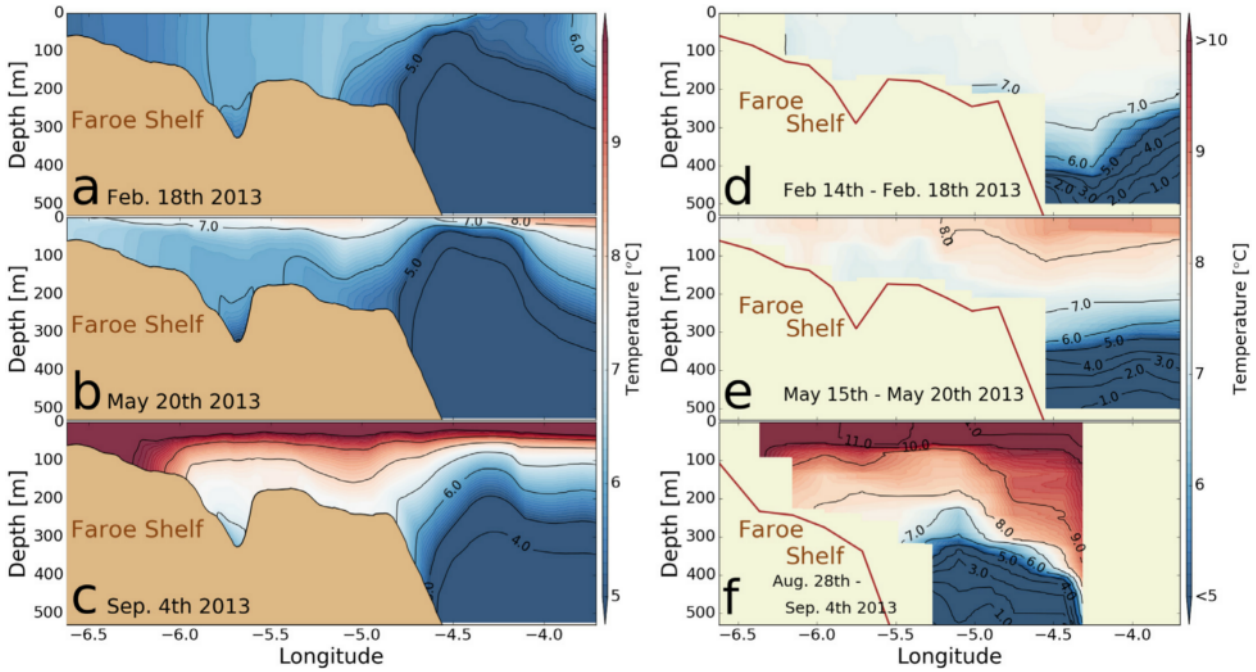

Fig. 8. a,b,c: Daily temperature averages from the model at section EasternS (Fig. 2). d,e: Temperature from observations from the Section EasternS obtained by FAMRI in February and May 2013. f: Temperature from section SouthernS a bit south of EasternS from FAMRI during cruise in August 2013 (Fig. 2).

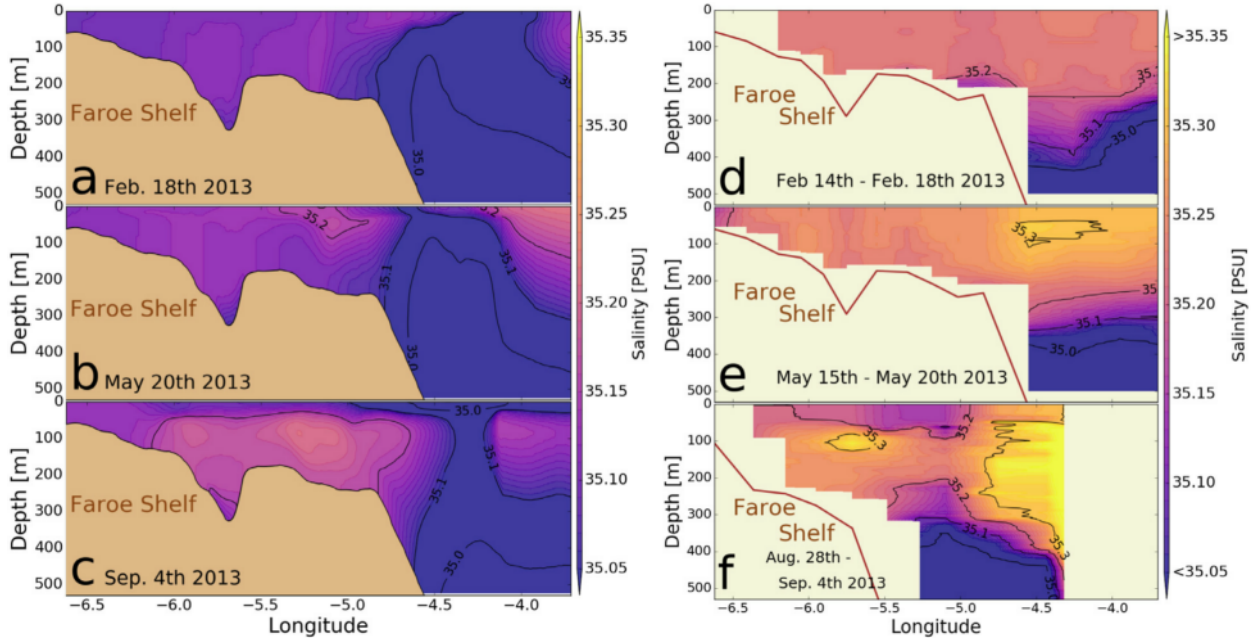

Fig. 9. a,b,c: Daily salinity averages from the model at section EasternS (Fig. 2). d,e: salinity from observations at the Section EasternS obtained by FAMRI in February and May 2013. f: salinity from section SouthernS a bit south of EasternS from FAMRI during cruise in August 2013 (Fig. 2).

and outer clockwise residual currents had compatible velocities to earlier studies (Larsen et al., 2008, 2009; Hansen et al., 2017).

In Section 4.1 we touched upon the model circulation, in particular along the eastern part of the model domain perimeter but also along the northern part of the model domain perimeter being rather spurious (Fig. 3). This is from the inconsistency of the bathymetry between the coarser 4 km model and the 800 meter simulation (Figure S1). However as stated through the results section this seems not to affect the obtained circulation on the shelf area, which is our main interest. The results showed reasonably realistic values for the circulation in the CS and we saw the tidal residual circulation in the barotropic flow in Fig. 3. Only on the easternmost part of the EasternS in the FSC we observed a large inconsistency between the model and the observations in velocities 5d. Nonetheless, this together with the recirculation on the northern boundary of the domain, implies that some caution most be taken in the interpretation of the flow of Atlantic water, entering the northern shelf and continuing into the southward flowing water on the eastern shelf as this amount could be exaggerated. The spurious flow along the boundary may also imply an erroneous pressure field as mentioned in Lien et al. (2013). In our case this could reduce the eastern flowing branch of Atlantic water into the Norwegian Sea and instead increase the amount of Atlantic water that is flowing onto the eastern shelf.

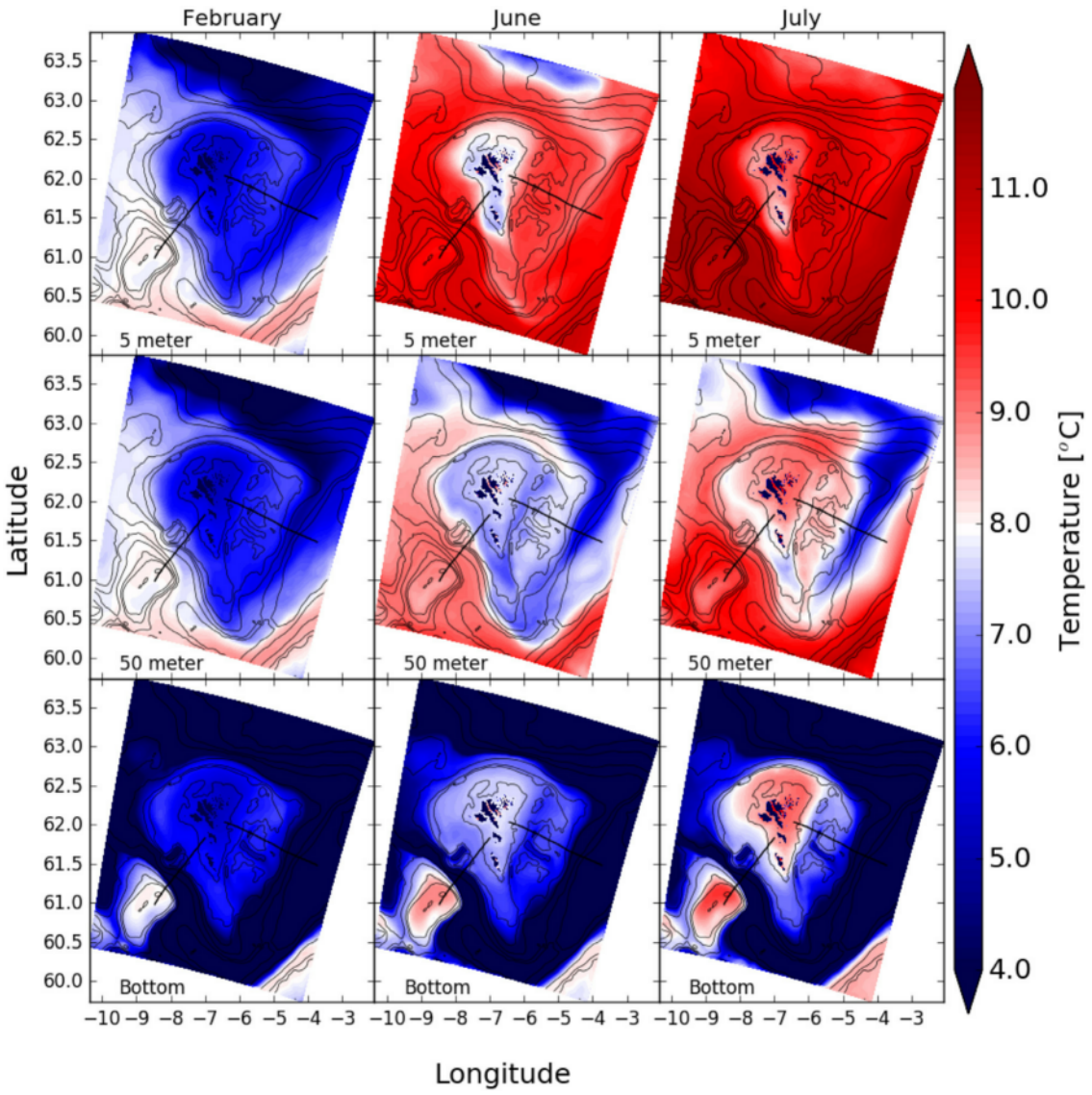

Fig. 10. Modeled temperature (°C, colorbar) at 5 meters depth (top), and 50 meters depth (middle) and in the bottom layer (last) in February, June, and July. Solid lines are depth contours at 100 m, 300 m, 500 m, 700 m, 1000 m, 1500 m, 2000 m, 3000 m. The black lines are the WesternS and the EasternS respectively.

The model domain is balancing the inflow and outflow and thus introducing the spurious currents along the northern and eastern model domain boundaries. However since our main interest is the Faroe shelf itself, it seems that the FarCoast800 model setup handles this issue quite well and is adjusted to simulate realistic conditions for the currents once reaching the central area of the model domain.

The results in Sections 4.2 and 4.3 indicate that the model performance by FarCoast800 is quite realistic on the shelf. Only during February, which is part of the spin-up period, the modeled salinity and the modeled temperature (Figs. 8a and 9a) disagree with observations. However, there is clearly a bias between the model and the observations when considering the absolute values of both temperature and salinity during the entire sample year. Due to the bias being quite persistent, this is an indication that the model setup and the dynamics are well captured and the issue is mainly from the boundary forcing. Thus the bias in temperature and in particular salinity may, at least partly, be traced back to the climatology (SODA) used as boundary condition in the SWIM model. Improving this would probably make it possible to compare the absolute values of temperature and salinity in Section 4.5.

The panel plot in Fig. 10, showing the monthly averages of the temperature for February, June and July at three different depths, clearly supports the assumption of the difference in dynamics of the OS and EB (Fig. 2). In the bottom layer (Fig. 10) the horizontal temperature gradient is strongest in the summer months, this demonstrates the dominance of atmospheric forcing in the shallow areas. Furthermore, at 50 meters depth the model indicates that water from the west (MNAW) flows northeastward around the shelf and flushes directly onto the EB from the northwest.

The model indicates that water, originating from the EIC, on the eastern Faroe shelf slope, flows in a relatively thin layer into the trenches deeper than 140 m on the eastern shelf (Fig. 10). There might be a week signal of some inflow along the banks in the observed sections in February and May (Fig. 8, at 5.7°W). Otherwise the observational evidence are scarce, except for a temperature series near bottom at the inner slope of the this trench showing an abrupt drop in temperature of 3–4 °C, and thereafter in periods, a tidal variation indicating that a temperature front is moving across this location. (K. M. H. Larsen, FAMRI, 2019, pers. comm., Hansen (2018))

The results also indicate a small intrusion of water from the eastern shelf being recirculated onto the western side of the

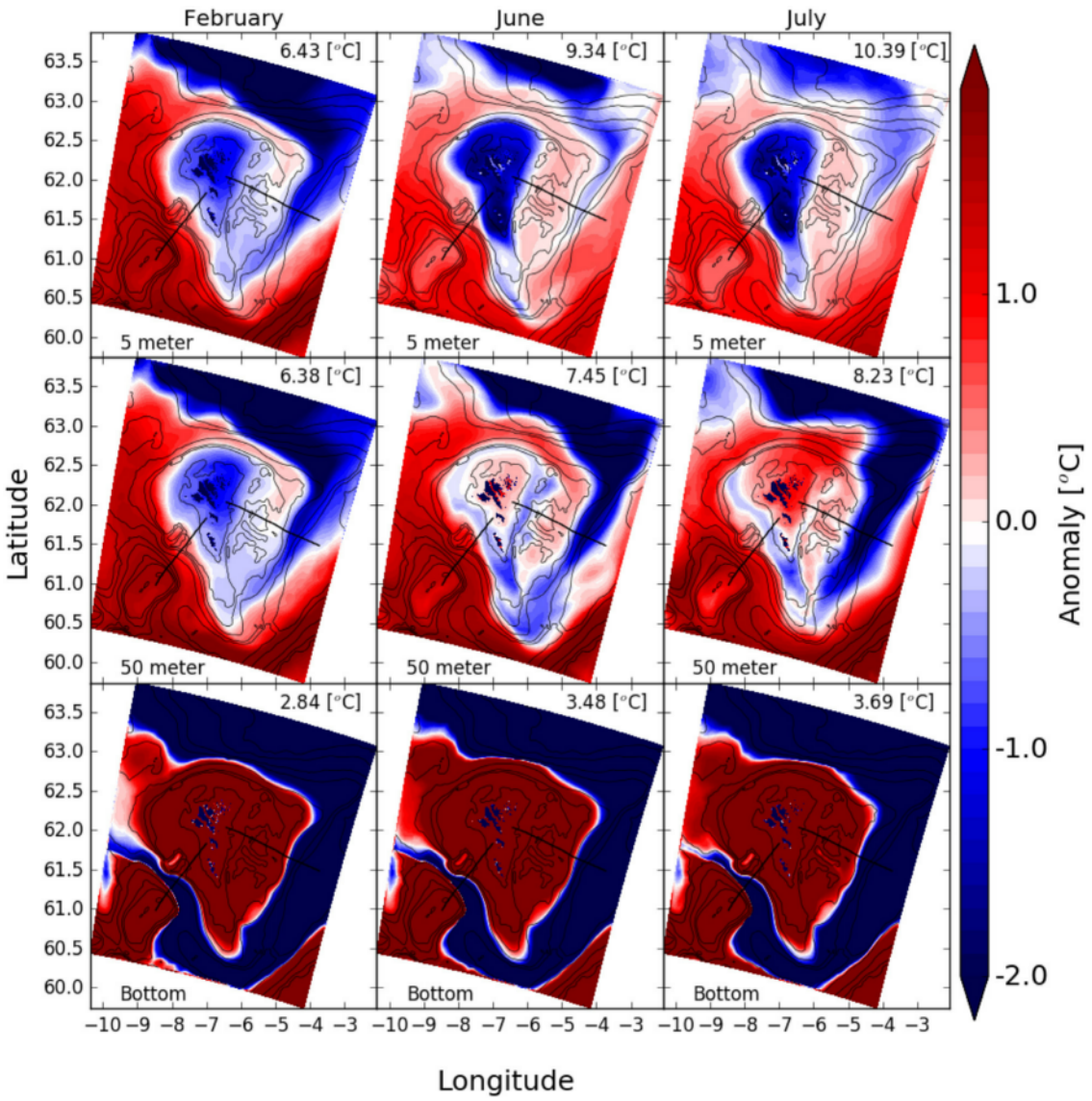

Fig. 11. Modeled temperature anomaly (°C, colorbar) at 5 meters depth (top), and 50 meters depth (middle) and in the bottom layer (last) in February, June, and July. Temperature anomaly is relative to monthly mean temperature shown in upper right corner of each plot. Solid lines are depth contours at 100 m, 300 m, 500 m, 700 m, 1000 m, 1500 m, 2000 m, 3000 m. The black lines are the WesternS and the EasternS respectively.

shelf across the southern part of the shelf (Fig. 3). There is some disagreement in how large this recirculation is in volume (Rossby and Flagg, 2012; Hansen et al., 2017). From the model simulation, it seems possible, that the WR and OS are fed from below by the colder water masses from FC and EIC through the southeastern part of the shelf (Fig. 11 at 50 meter depth and S3).

Again looking at Fig. 10 bottom layer, there is also a temperature gradient, between the central area of the sound between the largest islands, and the surrounding CS, indicating a locked bottom layer in the sound during June and July which is observed by Simonsen et al. (2018) and Hansen (1990) in the sound, although this has not been quantified by a model simulation prior to this study. The upper layers are controlled by atmosphere to a strong degree and below 50 meter depth we observe the oceanographic influence to become more dominant. The on-shelf water masses are resupplied by the surrounding ocean waters masses where mechanical energy drives the exchange (Eliasen et al., 2017a; Simpson and Sharples, 2012). Buoyancy driven input from atmosphere is dominant for shelf water, alongside fresh water input and tidal direct forcing from wind and waves (Eliasen et al., 2017a; Simpson and Sharples, 2012).

The seasons on the Faroe shelf are defined through temperature changes and the changes observed through stratification (Eliasen et al., 2017a) which are clearly visible in Fig. 12. During winter the shelf water is unstratified and there is no vertical temperature gradient neither in the WR nor the EB (Figs. 6a and 8a). The spring season is defined as to when the stratification on the shelf begins (Eliasen et al., 2017b). The temperature bias in Fig. 12 is greatest in the bottom layer of the model and is most likely influenced by the boundary conditions (Figure not shown). Since the setup favors higher resolution in the upper 50 m, our applied grid stiffness may introduce various levels of horizontal pressure gradient errors and then non-real velocities as observed in the FBC (Beckmann and Haidvogel, 1993; Haney, 1991).

However, considering the long term salinity variations in the observations at station Sk (Fig. 15), the salinity was generally higher than obtained by the model in all years back to the beginning of the record in year 1996 (Larsen et al., 2008). The observation shows a clear seasonal variation with lower values in the winter, though not as low as seen in our simulation in the period back to year 2000 (Larsen et al., 2008). In mid 2013 the observed seasonal decline started relatively early and ended

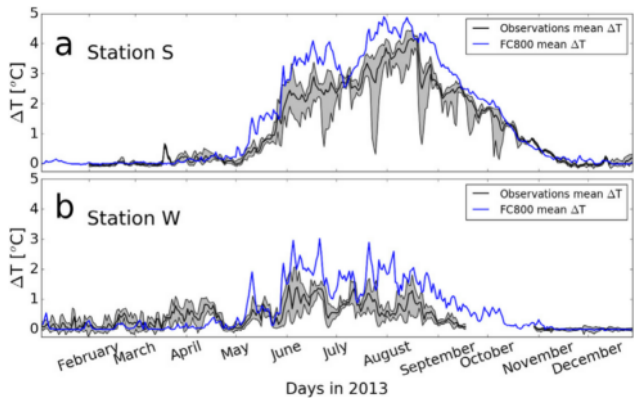

Fig. 12. Surface to bottom temperature difference at stations S (a) and W (b). The black line is daily mean, while the gray areas indicate daily minimum and maximum measured temperature differences and blue lines are daily mean from the numerical model. (For interpretation of the references to color in this figure legend, the reader is referred to the web version of this article.)

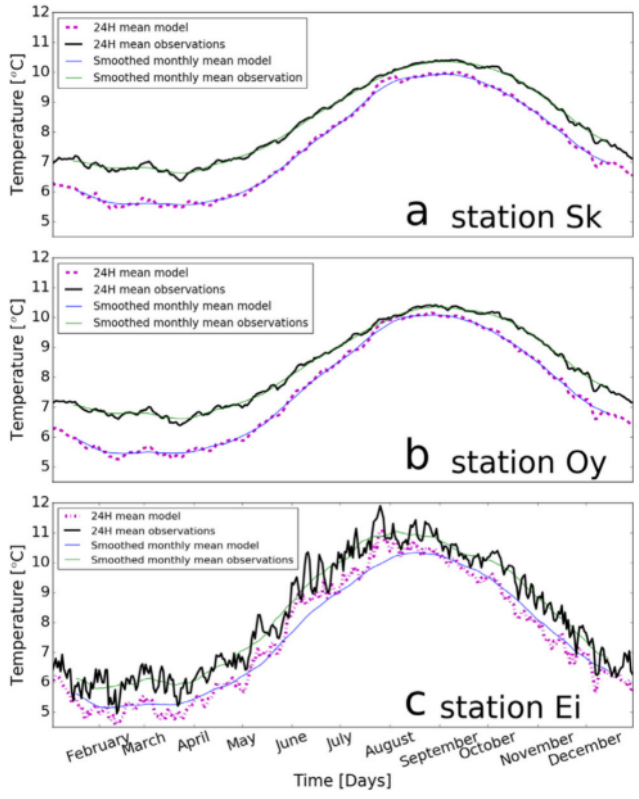

Fig. 13. Daily mean (thick line) and monthly mean (thin line) from the model (magenta and blue) and observations (black and green) at the central shelf stations Sk (a), Oy (b), and Ei (c). See Fig. 2 for locations. (For interpretation of the references to color in this figure legend, the reader is referred to the web version of this article.)

in the lowest winter minimum seen in the record until then. In the following three years the observed salinity stayed at the level obtained in the simulation until the winter 2016–17, when the salinity declined further to a level of order 0.1 PSU below our model results. In the multiyear simulation by Rasmussen et al. (2014), they obtained a fairly good agreement in salinity in the first years of their simulations, but in the last years of the simulation the model was not able to follow the increasing salinity, which they explained was related to their boundary forcing.

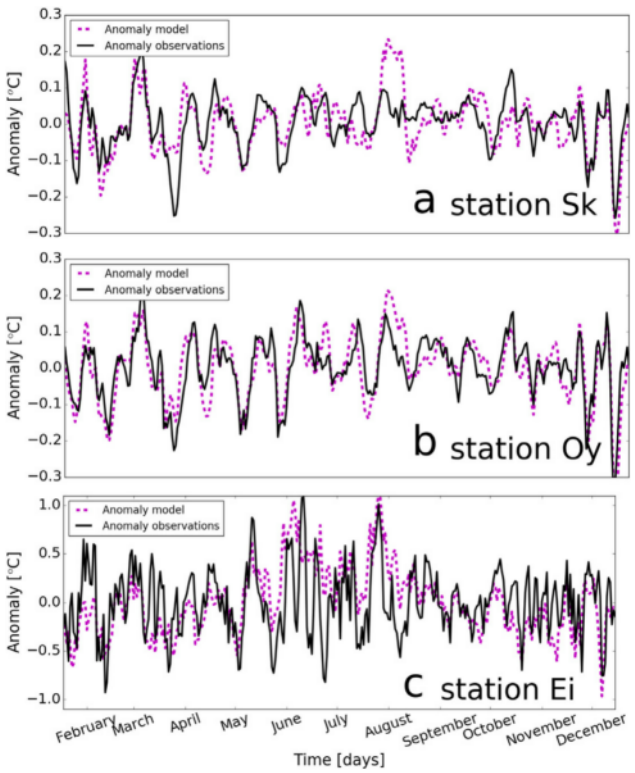

Fig. 14. Temperature anomalies at stations Sk (a), Oy (b) and Ei (c) (Fig. 2) estimated by subtracting 30 day running mean from the daily mean temperatures in Fig. 13. Note different vertical scale in the bottom plot.

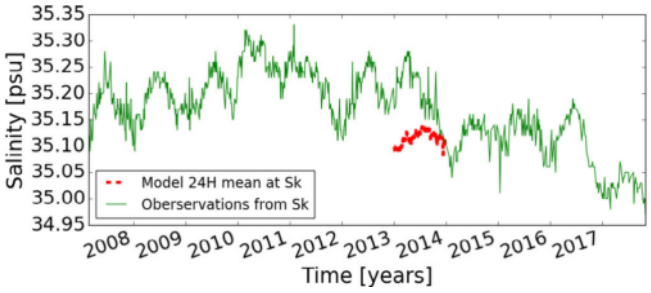

Fig. 15. Salinity at station Sk Fig. 2.

These long-term variations seen in the observed salinity are of lateral origin Larsen et al. (2009). The salinity variations are likely regulated by the strength of the North Atlantic Subpolar Gyre, which influences the strength of the relative amount of MNAW and the more saline NAW water is flowing into the area (Hátún et al., 2005). This dynamic feature of the North Atlantic that most probably is influencing our region of interest is omitted in our simulation. Here, as mentioned, we adopt the lateral boundary forcing from the SVIM model, which again applies a climatology along its lateral boundary in the Atlantic in 2013 (Section 3.1).

6. Concluding remarks

Our main conclusions are firstly that in order to be able to simulate day to day upper ocean variations a highly resolved atmospheric model is important, as we found high correlations between observations and model output. Secondly we can conclude that there is a difference of the feeding of water onto the eastern region and the western region controlled by the

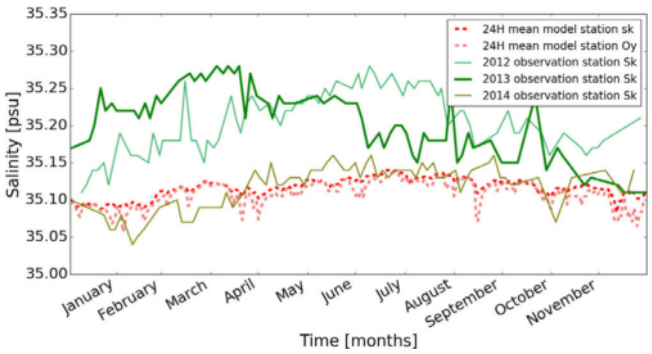

Fig. 16. Annual salinity observations 2012–2014 against FC800 from 2013.

large scale upper ocean currents that can be recognized through temperature differences on the shelf.

The 800 meter resolution of FarCoast800 is highly capable of reproducing the short term variations on the upper shelf. Our validation show that a high resolution atmospheric forcing is significant in order to get a realistic simulation.

This paper shows that the FarCoast800 model setup has good performance on and around the Faroe shelf, even though the model flow in the off-shelf area is highly constrained by the boundary conditions and the set-up, where enhanced resolution for the upper 50 meters is preferred.

In a future model based salmon louse prediction and contingency system for the Faroe Islands the model domain can improve the predictions of sea lice infestation pressure as in Sandvik et al. (2016). Since the quality of such a louse dispersion model will depend of the quality of the underlying system, it is imperative that the ocean model is of high quality.

7. Abbreviations

ADCP	Acoustic Doppler Current Profiler
CS	Central Shelf
EIC	East Icelandic Current
EB	Eastern Banks
FB	Faroe Bank
FBC	Faroe Bank Channel
FBCO	Faroe Bank Chanel Overflow
FC	Faroe Current
FMRI	Faroe Marine Research Institute
FSC	Faroe Shetland channel
FSF	Faroe Shelf Front
GLS	Generic Length Scale
HYCOM	3D HYbrid Coordinate Ocean Model
IFR	Iceland Faroe Ridge
MNAW	Modified North Atlantic Water
NADW	North Atlantic Deep Water
NAW	North Atlantic Water
NSDW	Norwegian Sea Deep Water
OPW	Office for Public Works
OS	Outer Shelf
ROMS	Regional Ocean Modeling System
SFC	Southern Faroe Current
SODA	Simple Ocean Data Assimilation
SSC	Scottish Slope Current
SVIM	Nordic Seas 4 km numerical ocean model hindcast archive
WR	Western Region
WRF	Weather Research and Forecasting model
WTB	Wyville Thomson Basin

Declaration of competing interest

The authors declare that they have no known competing financial interests or personal relationships that could have appeared to influence the work reported in this paper.

Acknowledgments

The timeseries and hydrographic data provided by Faroe Marine Research Institute and Office for Public Works in the Faroes (www.landsverk.fo) is very much appreciated.

Thanks to Lars Asplin, Institute of Marine Research, Norway, for providing the network and for the general introduction to ROMS.

Thanks to the two anonymous reviewers for the highly appreciated constructive feedback.

This paper is part of the PhD project by SVE, which is financially supported by Statoil Faroes, Mowi Faroe Islands , P/F Bakkafrost and the Faroese Research Council (Grant no. 0445).

Appendix A. Supplementary data

Supplementary material related to this article can be found online at https://doi.org/10.1016/j.rsma.2020.101475. Here we include all of the seasonal section plots for both sections WesternS and EasternS, as well as average

References

Beaird, N.L., Rhines, P.B., Eriksen, C., 2016. Observations of seasonal subduction at the iceland-faroe front. J. Geophys. Res.: Oceans 121 (6), 4026–4040. http://dx.doi.org/10.1002/2015JC011501, URL: https://agupubs.onlinelibrary.wiley.com/doi/abs/10.1002/2015JC011501.

Beckmann, A., Haidvogel, D.B., 1993. Numerical simulation of flow around a tall isolated seamount. part I: Problem formulation and model accuracy. J. Phys. Oceanogr. 23 (8), 1736–1753. http://dx.doi.org/10.1175/1520-0485(1993)023<1736:NSOFAA>2.0.CO;2, URL: arXiv:https://journals.ametsoc.org/jpo/article-pdf/23/8/1736/4423464/1520-0485(1993)023_1736_nsofaa_2_0_co_2.pdf.

Carton, J., Chepurin, G., Cao, X., Giese, B., 2000. A simple ocean data assimilation analysis of the global upper ocean 1950 95. part I: Methodology. J. Phys. Oceanogr. 30, 294–309. http://dx.doi.org/10.1175/1520-0485(2000)030<0294:ASODAA>2.0.CO;2.

Carton, J.A., Giese, B.S., 2008. A reanalysis of ocean climate using simple ocean data assimilation (SODA). Mon. Weather Rev. 136 (8), 2999–3017. http://dx.doi.org/10.1175/2007MWR1978.1, URL: arXiv:https://doi.org/10.1175/2007MWR1978.1.

Chapman, D.C., 1985. Numerical treatment of cross-shelf open boundaries in a barotropic coastal ocean model. J. Phys. Oceanogr. 15, 1060–1075. http://dx.doi.org/10.1175/1520-0485(1985)015.

Chassignet, E.P., Hurlburt, H.E., Smedstad, O.M., Halliwell, G.R., Hogan, P.J., Wallcraft, A.J., Baraille, R., Bleck, R., 2007. The HYCOM (hybrid coordinate ocean model) data assimilative system. J. Mar. Syst. 65 (1), 60–83. http://dx.doi.org/10.1016/j.jmarsys.2005.09.016, Marine Environmental Monitoring and Prediction.

Dam, P.M., 2019. Statistics FAROE ISLANDS. URL: https://hagstova.fo/en/economy/international-trade/exports-goods.

Davidsen, E., Førland, E., Madsen, H., 1994. Orographically enhanced proecipitation on the faroe islands. In: Kern-Hansen, C., Rosbjerg, D., Thomsen, R. (Eds.), Nordic Hydrological Conference 1994. Nordic Hydrological Program (NHP) Report, number 34, Nordic Association for Hydrology, Tórshavn, Faroe Islands, pp. 229–239.

Egbert, G., Erofeeva, S., 2002. Efficient inverse modeling of Barotropic ocean tides. J. Atmos. Ocean. Technol. 19, 183–204. http://dx.doi.org/10.1175/1520-0426(2002)019<0183:EIMOBO>2.0.CO;2.

Eliasen, S.K., Hansen, B., Larsen, K.M.H., Hátún, H., 2016. The exchange of water between the Faroe Shelf and the surrounding waters and its effect on the primary production. J. Mar. Syst. 153, 1–9. http://dx.doi.org/10.1016/j.jmarsys.2015.08.004.

Eliasen, S.K., Hátún, H., Larsen, K.M.H., Hansen, B., Rasmussen, T.A.S., 2017a. Phenologically distinct phytoplankton regions on the Faroe Shelf - identified by satellite data, in-situ observations and model. J. Mar. Syst. 169, 99–110. http://dx.doi.org/10.1016/j.jmarsys.2017.01.015.

Eliasen, S.K., Hátún, H., Larsen, K.M.H., Jacobsen, S., 2017b. Faroe shelf bloom phenology – the importance of ocean-to-shelf silicate fluxes. Cont. Shelf Res. 143, 43–53. http://dx.doi.org/10.1016/j.csr.2017.06.004.

Eliasen, S.K., Hátún, H., Larsen, K.M.H., Vang, H.B.M., Rasmussen, T.A.S., 2019. The faroe shelf spring bloom onset explained by a 'Critical Volume Hypothesis'. J. Mar. Syst. 194, 91–101. http://dx.doi.org/10.1016/j.jmarsys.2019.02.005.

Flather, R., 1976. A tidal model of the northwest European continental shelf. Mem. Soc. R. Sci. Liege 10, 141–164..

Haidvogel, D., Arango, H., Budgell, W., Cornuelle, B., Curchitser, E., Lorenzo, E., Fennel, K., Geyer, W., Hermann, A., Lanerolle, L., Levin, J., McWilliams, J., Miller, A., Moore, A., Powell, T., Shchepetkin, A., Sherwood, C., Signell, R., Warner, J., Wilkin, J., 2008. Ocean forecasting in terrain-following coordinates: Formulation and skill assessment of the regional ocean modeling system. J. Comput. Phys. 227, 3595–3624. http://dx.doi.org/10.1016/j.jcp.2007.06.016.

Haney, R.L., 1991. On the pressure gradient force over steep topography in sigma coordinate ocean models. J. Phys. Oceanogr. 21 (4), 610–619. http://dx.doi.org/10.1175/1520-0485(1991)021<0610:OTPGFO>2.0.CO;2, URL: arXiv:https://journals.ametsoc.org/jpo/article-pdf/21/4/610/4422471/1520-0485(1991)021_0610_otpgfo_2_0_co_2.pdf.

Hansen, B., 1990. Oxygentrot og útskifting íbotnvatninum á føroyskum gáttarfiròum. Fiskirannsóknir 6, 188–258.

Hansen, B., 2018. Botnhitin kring Føroyar. In: Faroe Marine Research Institute. Smárit, number 03, Havstovan, Tórshavn, Faroe Islands, pp. 1–22.

Hansen, B., Hátún, H., Kristiansen, R., Olsen, S.M., Østerhus, S., 2010. Stability and forcing of the Iceland-Faroe inflow of water, heat,and salt to the Arctic. Ocean Sci. 6, 1013–1026. http://dx.doi.org/10.5194/os-6-1013-2010.

Hansen, B., Húsgarò Larsen, K.M., Hátún, H., Østerhus, S., 2016. A stable faroe bank channel overflow 1995–2015. Ocean Sci. 12 (6), 1205–1220. http://dx.doi.org/10.5194/os-12-1205-2016, URL: https://www.ocean-sci.net/12/1205/2016/.

Hansen, B., Østerhus, S., 2000. North atlantic-nordic seas exchanges. Prog. Oceanogr. 45, 109–208.

Hansen, B., Østerhus, 2007. Faroe bank channel overflow 1995–2005. Prog. Oceanogr. 75, http://dx.doi.org/10.1016/j.pocean.2007.09.004.

Hansen, B., Poulsen, T., Húsgarò Larsen, K.M., Hátún, H., Østerhus, S., Darelius, E., Berx, B., Quadfasel, D., Jochumsen, K., 2017. Atlantic water flow through the faroese channels. Ocean Sci. 13 (6), 873–888. http://dx.doi.org/10.5194/os-13-873-2017.

Hátún, H., 2004. The Faroe Current (Ph.D. thesis). University of Bergen/Faroe Marine Research Institute.

Hátún, H., Sandø, A.B., Drange, H., Hansen, B., Valdimarsson, H., 2005. Influence of the atlantic subpolar gyre on the thermohaline circulation. Science 309, 1841–1843.

Huserbråten, M., Moland, E., Albretsen, J., 2018. Cod at drift in the North Sea. Prog. Oceanogr. 167, http://dx.doi.org/10.1016/j.pocean.2018.07.005.

Jacobsen, S., Gaard, E., Larsen, K.M.H., Eliasen, S.K., Hátún, H., 2018. Temporal and spatial variability of zooplankton on the Faroe shelf in spring 1997–2016. J. Mar. Syst. 177, 28–38. http://dx.doi.org/10.1016/j.jmarsys.2017.08.004.

Kragesteen, T.J., Simonsen, K., Visser, A.W., Andersen, K.H., 2018. Identifying salmon lice transmission characteristics between faroese salmon farms. Aquac. Environ. Interact. 10, 49. http://dx.doi.org/10.3354/aei00252.

Larsen, K.M., Hansen, B., Svendsen, H., 2008. Faroe shelf water. Cont. Shelf Res. 28 (14), 1754–1768. http://dx.doi.org/10.1016/j.csr.2008.04.006.

Larsen, K.M., Hansen, B., Svendsen, H., 2009. The faroe shelf front: Properties and exchange. J. Mar. Syst. 78 (1), 9–17. http://dx.doi.org/10.1016/j.jmarsys.2009.02.003.

Lien, V., Gusdal, Y., Albretsen, J., Melsom, A., Vikebø, F., 2013. Evaluation of a nordic seas 4 km numerical ocean model archive. Fisken og Havet 7, 7:79.

Marchesiello, P., McWilliams, J., Shchepetkin, A., 2001. Open boundary conditions for long-term integration of regional oceanic models. Ocean Model. 3, 1–20. http://dx.doi.org/10.1016/S1463-5003(00)00013-5.

McKenna, C., Berx, B., Austin, W., 2016. The decomposition of the faroe-shetland channel water masses using parametric optimum multi-parameter analysis. Deep Sea Res. Part I 107, 9–21. http://dx.doi.org/10.1016/j.dsr.2015.10.013.

Myksvoll, M., Sandvik, A., Albretsen, J., Asplin, L., Johnsen, I., Karlsen, O., Kristensen, N., Melsom, A., Skardhamar, J., Ådlandsvik, B., 2018. Evaluation of a national operational salmon lice monitoring system—From physics to fish. PLOS ONE 13, e0201338. http://dx.doi.org/10.1371/journal.pone.0201338.

Myksvoll, M., Sandvik, A., Skaròhamar, J., Sundby, S., 2012. Importance of high resolution wind forcing on eddy activity and particle dispersion in a norwegian fjord. Estuar., Coast. Shelf Sci. 113, 293–304. http://dx.doi.org/10.1016/j.ecss.2012.08.019.

Patursson, E.J., Simonsen, K., Visser, A.W., Patursson, Ø., 2017. Effect of exposure on salmon lice lepeophtheirus salmonis population dynamics in faroese salmon farms. Aquac. Environ. Interact. 9, 33–43.

Rasmussen, T., Olsen, S.M., Hansen, B., Hátún, H., Larsen, K.M., 2014. The faroe shelf circulation and its potential impact on the primary production. Cont. Shelf Res. 88, 171–184. http://dx.doi.org/10.1016/j.csr.2014.07.014.

Rossby, T., Flagg, C.N., 2012. Direct measurement of volume flux in the faroe-shetland channel and over the iceland-faroe ridge. Geophys. Res. Lett. 39 (7), http://dx.doi.org/10.1029/2012GL051269.

Sandvik, A., Bjørn, P., Ådlandsvik, B., Asplin, L., Skaròhamar, J., Johnsen, I., Myksvoll, M., Skogen, M., 2016. Toward a model-based prediction system for salmon lice infestation pressure. Aquacult. Environ. Interact. 8, 527–542. http://dx.doi.org/10.3354/aei00193.

Shchepetkin, A.F., McWilliams, J.C., 2005. The regional oceanic modeling system (ROMS): A split-explicit, free-surface, topography-following-coordinate oceanic model. Ocean Model. 9 (4), 347–404. http://dx.doi.org/10.1016/j.ocemod.2004.08.002.

Simonsen, K., Joensen, E., Erenbjerg, S., 2018. Sundalagiò - Samandráttur av hydrografiskum mátingum árini 2013-2017. In: Fiskaaling Rit. Technical Report, number 01, Fiskaaling P/F, Tórshavn, Faroe Islands, pp. 1–50.

Simpson, J.H., Sharples, J., 2012. Introduction to the Physical and Biological Oceanography of Shelf Seas. Cambridge University Press, http://dx.doi.org/10.1017/CBO9781139034098.

Skogseth, R., Asplin, L., Sandvik, A.D., 2007. Wind and tidal forcing on the mesoscale circulation in storfjorden, svalbard. Cont. Shelf Res. 27 (2), 208–227. http://dx.doi.org/10.1016/j.csr.2006.10.001.

Ullgren, J., Fer, I., Darelius, E., Beaird, N., 2014. Interaction of the faroe bank channel overflow with iceland basin intermediate waters. J. Geophys. Res.: Oceans 119 (1), 228–240. http://dx.doi.org/10.1002/2013JC009437.

Umlauf, L., Burchard, H., 2003. A generic length-scale equation for geophysical turbulence models. J. Mar. Res. 61, 235–265. http://dx.doi.org/10.1357/002224003322005087.

Supplement for Paper I

Erenbjerg, S. V., Albretsen, J., Simonsen, K., Sandvik, A. D., & Kaas, E. (2020). A step towards high resolution modeling of the central Faroe shelf circulation by FarCoast800. Regional Studies in Marine Science, 40, 101475. https://doi.org/https://doi.org/10.1016/j.rsma.2020.101475

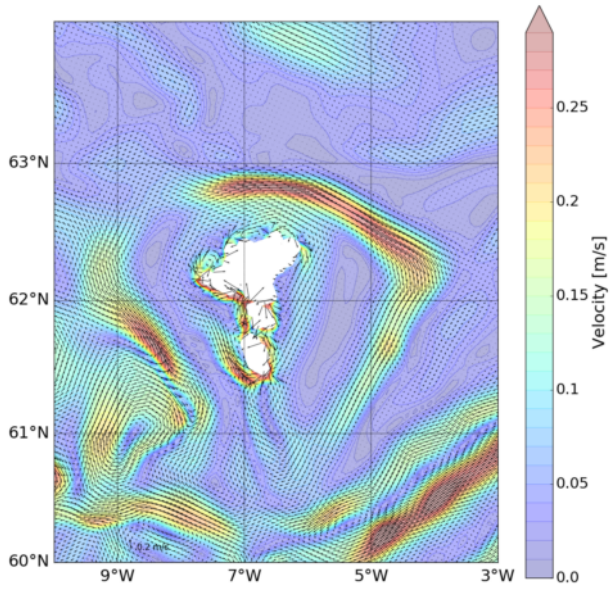

Figure S1: The 2013 average current from SVIM used as boundary forcing.

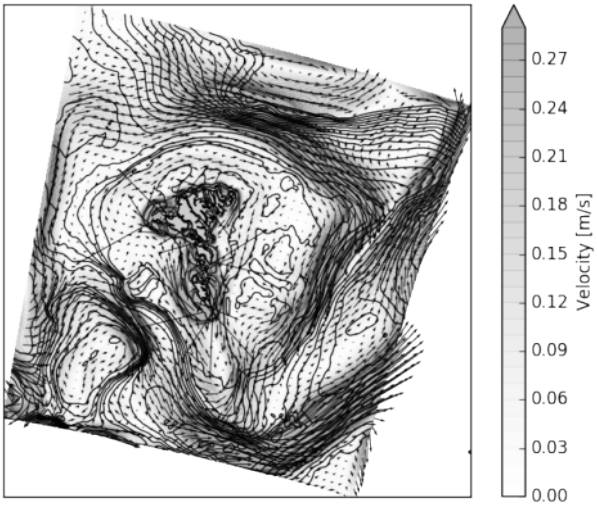

Figure S2: The 2013 average current from FarCoast800 upper 10 layers.

1. Supplementary material

Here we include all of the seasonal section plots for both sections WesternS and EasternS, as well as average current plots from the boundary forcing (SVIM), and upper and lower FarCoast800 layers respectively.

1.1. Seasonal sections

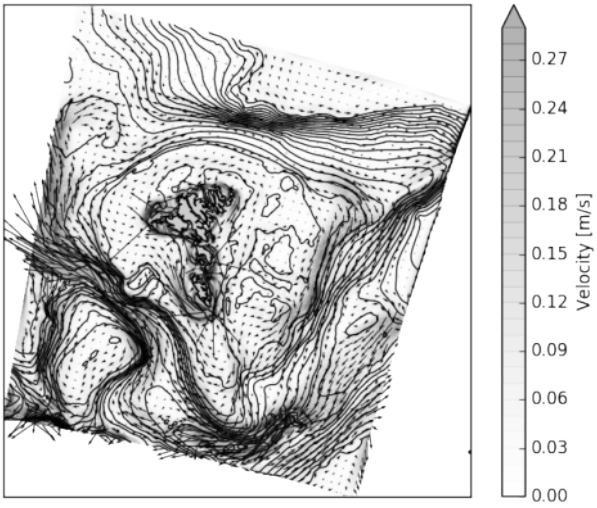

Figure S3: The 2013 average current from FarCoast800 bottom 2 layers.

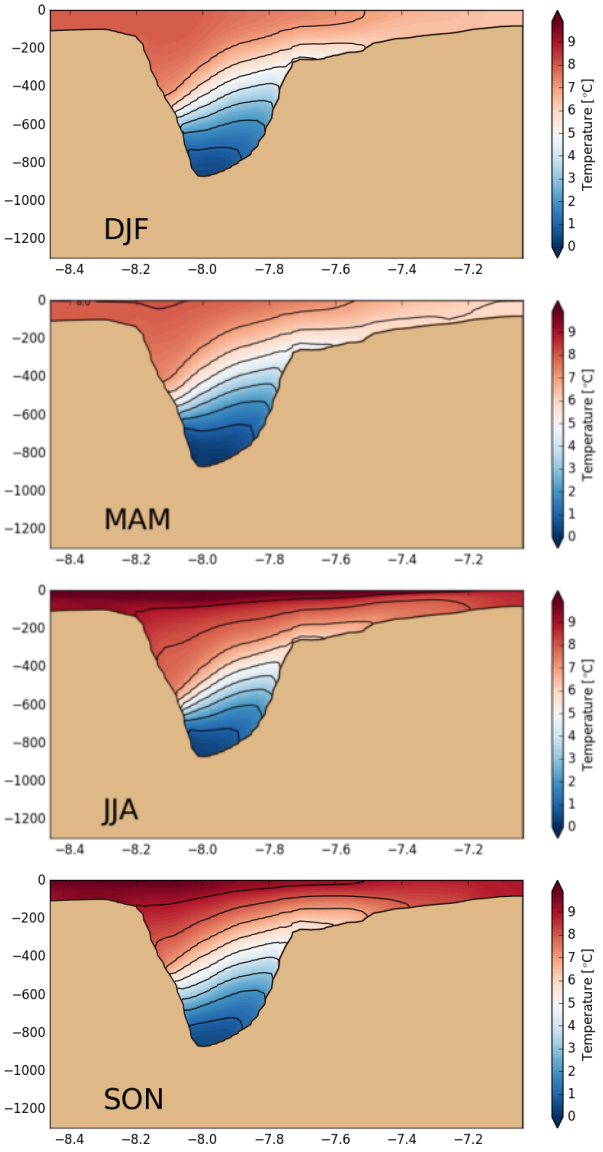

Figure S4: Seasonal temperature average from December, January, Febuary (DJF), March, April, May (MAM), June, July, August (JJA), September, October, November (SON) in western section in Figure 2

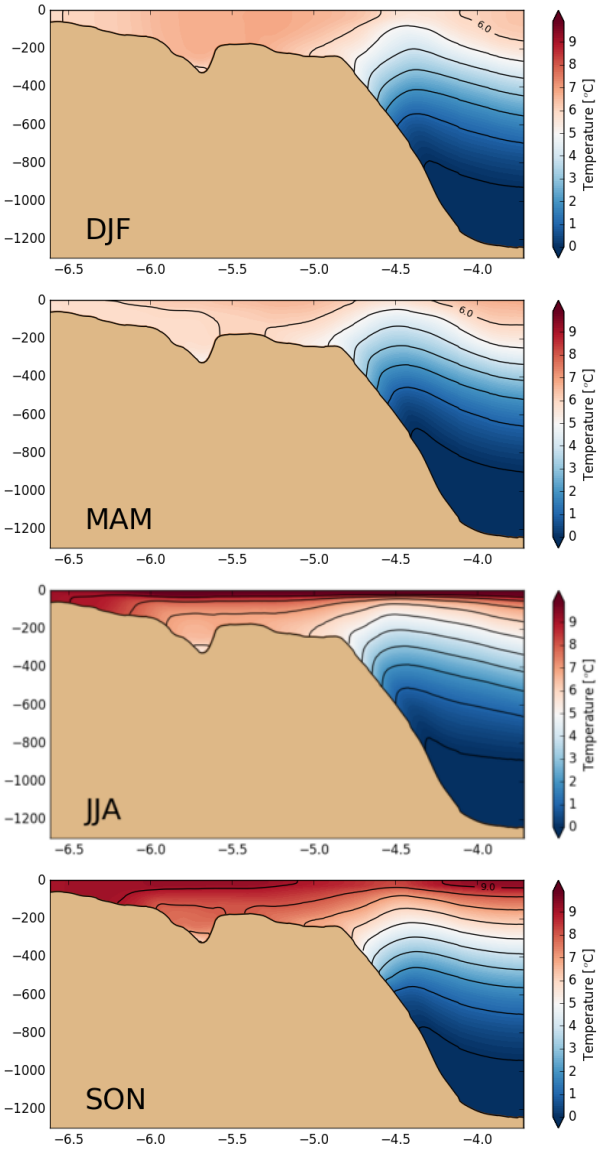

Figure S5: Seasonal temperature average from December, January, Febuary (DJF), March, April, May (MAM), June, July, August (JJA), September, October, November (SON) in eastern section in Figure 2

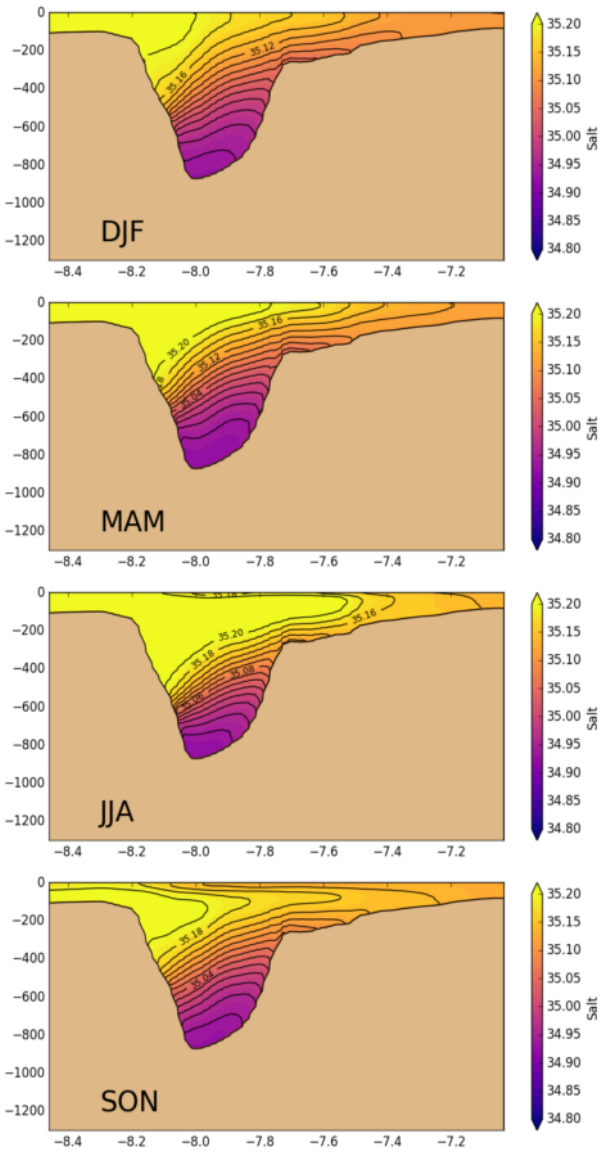

Figure S6: Seasonal salinity average from December, January, Febuary (DJF), March, April, May (MAM), June, July, August (JJA), September, October, November (SON) in the western section in Figure 2

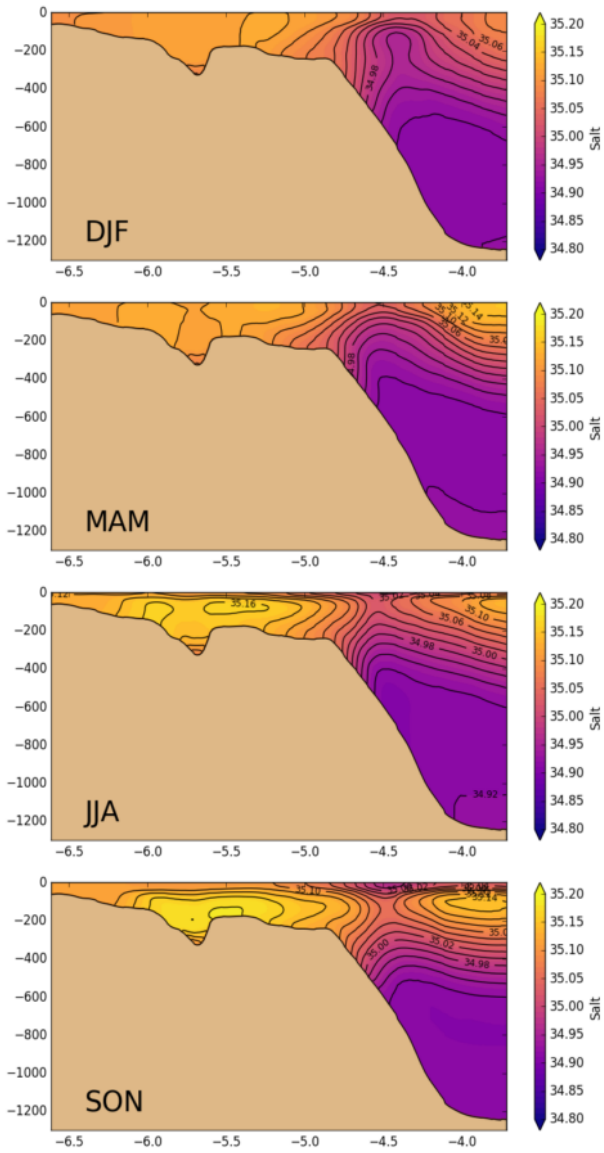

Figure S7: Seasonal salinity average from December, January, Febuary (DJF), March, April, May (MAM), June, July, August (JJA), September, October, November (SON) in the eastern section in Figure 2

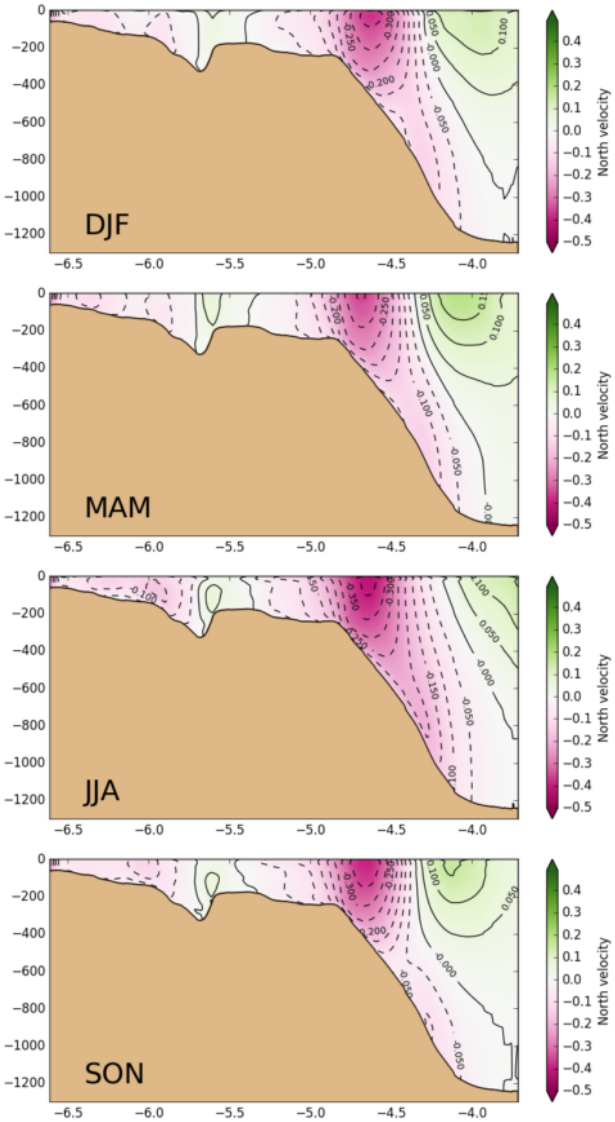

Figure S8: Seasonal averages of Northward velocities at section East in Figure 2.

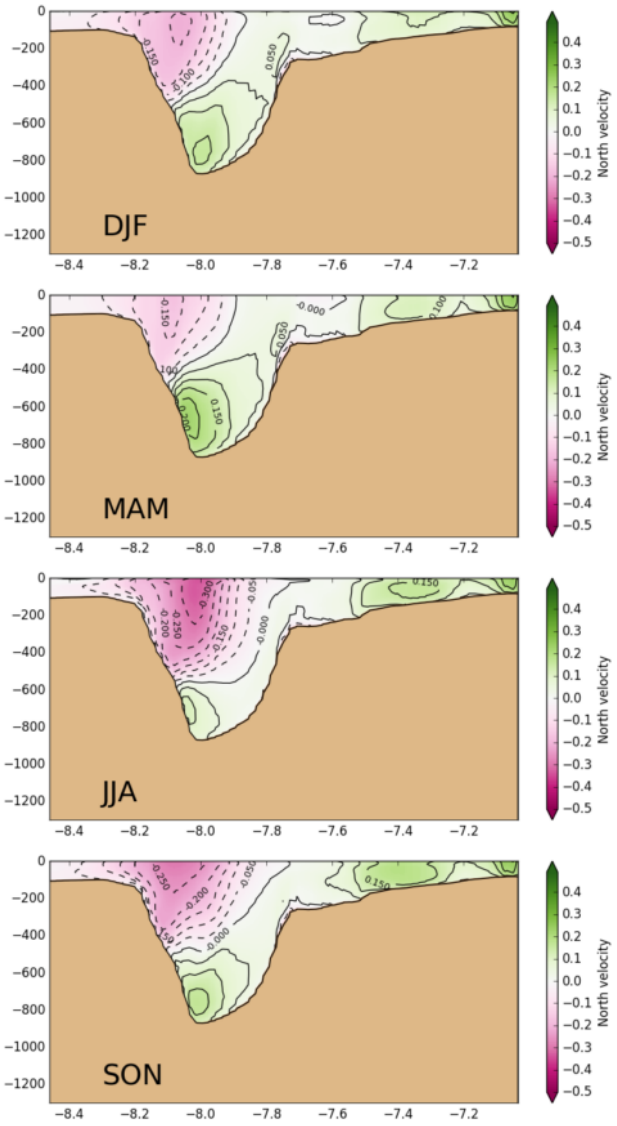

Figure S9: Seasonal averages of speed of the northward constituent at section WesternS (Figure 2). The green color is northward flowing currents and the purple color is southward flowing currents.

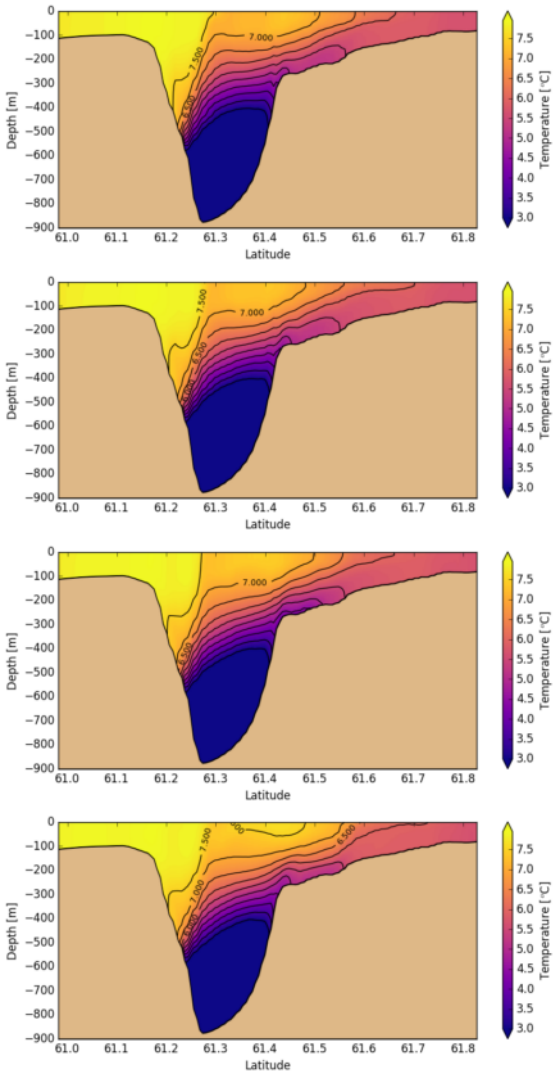

Figure S10: Daily temperature averages modeled by FarCoast800. Top figure is from the 14th of February and last figure is from the 17th of February. The same period as CTD was conducted by Havstovan in figure 6a.

Paper II

Erenbjerg, S. V., Albretsen, J., Simonsen, K., Olsen, E., Kaas, E., & Hansen, B. (2021). A tidally driven estuary close to an amphidromy. Ocean Sci. Discuss., 2021, 1-23. https://doi.org/10.5194/os-2021-23

II

A tidally driven fjord-like strait close to an amphidromic region

Sissal Vágsheyg Erenbjerg[1,2], Jon Albretsen[3], Knud Simonsen[4], Erna Lava Olsen[1], Eigil Kaas[2,5], and Bogi Hansen[6]

[1]Dept. of Fjord Dynamics, Fiskaaling A/S, við Áir 11, FO-430 Hvalvík, Faroe Islands
[2]Niels Bohr Institute, Copenhagen University, Juliane Maries Vei 30, DK-2100 Copenhagen, Denmark
[3]Institute of Marine Research, P.O. box 1870 Nordnes, NO-5817, Bergen, Norway
[4]Dept. of Science and Technology, University of the Faroe Islands, J. C. Svabosgøta 14, FO-100 Tórshavn, Faroe Islands
[5]National Center for Climate Research, Danish Meteorological Institute, Lyngbyvej 100, DK-2100 Copenhagen, Denmark
[6]Faroe Marine Research Institute, P.O. 3051, FO-110 Tórshavn, Faroe Islands

Correspondence to: Sissal Vágsheyg Erenbjerg (sissal@fiskaaling.fo)

Abstract. The strait, "Sundalagið Norður", is the northern part of a narrow body of seawater separating the two largest islands in the Faroe Islands (Faroes). It has shallow sills in both ends and considerably deeper waters in-between. South of the southern end of the strait there is an amphidromic region for the semidiurnal tides so that the tidal range is much lower south of the strait than north of it. The resulting tidal forcing generates periodically varying inflow of seawater across the northern sill, but only a part of that manages to cross the narrow and shallow southern sill. Combined with a large input of freshwater, this gives the strait a fjord-like character. To investigate how this fjord-like character affects the circulation within the strait and its exchanges with outside waters, a pilot project was initiated to simulate the dynamics of the strait with a high-resolution ocean model for a month. The model simulations show clearly the dominance of tidal forcing over freshwater (estuarine) and wind on time scales up to a day. On longer time scales, the simulations indicate systematic variations in the net flows (averaged over a diurnal tidal period) through both the upper and deeper layers. These long-period variations of net flow in the model simulations are forced by sea level differences between both ends of the strait generated by the dominant fortnightly and monthly tidal constituents (Mf, MSf, Mm, MSm). Harmonic analysis of sea level records from two tide gauges located off each end of the strait verifies that this behaviour is not a model artefact and it has pronounced effects on the strait. Not only does it induce long-period – mainly fortnightly - variations in the net flow through the strait, but it also generates variations in the estuarine characteristics. According to the model simulations, periods with net southward flow – typically lasting a week - have a strait-like character with net southward flow almost everywhere. Periods with net northward flow, in contrast, have a more fjord-like character with stronger salinity stratification and a southward counter-flow in the deep layer. This also induces a large difference in renewal rate of the deep water between the two periods, which is important to consider for human utilization of the strait, especially the local aquaculture plant. The combination of topographic, freshwater, and tidal characteristics creating these long-period variations is rather unusual and it is not known whether similar systems exist elsewhere, but the long-period variations tend to be masked by the stronger semidiurnal and diurnal variations and may easily be overlooked.

1 Introduction

This study presents results from a strait, "Sundalagið Norður" [pronounced: ˈsʊntaˌlɛaːjɪ ˈnoːɹʊɹ], located in the Faroe Islands (hereafter: Faroes), in the North East Atlantic (Fig. 1a). When compared to better known narrow straits (Gibraltar Strait, Sunda Strait, Strait of Dover, etc.), the strait treated here is considerably smaller, both in terms of physical extent and volume transport. A priori, Sundalagið Norður therefore might not seem worthy of much interest, but it does have some features that distinguish it from a typical shallow strait and make it difficult to put into established classification systems (e.g., Li et al., 2015):

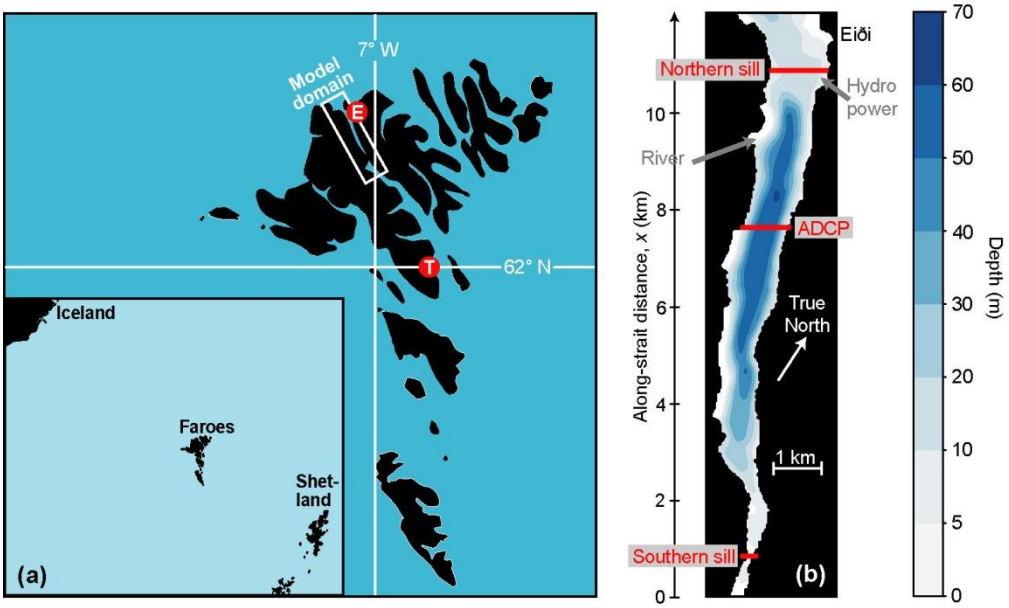

Figure 1. (a) The strait studied in this paper is located within the white rectangle, which defines the domain of a high-resolution model used in the study. The Faroes are situated between Iceland and Shetland (inset map). The red circles show two sites: Tórshavn (T) [pronounced: ˈtʰɛuːɻʂ ˌhavn] and Eiði (E) [pronounced: aiːjɪ] referred to in the text. **(b)** Bottom topography of the strait. Freshwater supply from a river and a hydro-power plant are shown by grey arrows. Red lines indicate three cross-strait sections discussed in the manuscript. The vertical x-axis indicates along-strait distance.

Firstly, the strait has sills in both ends that are considerably shallower (sill depths: 4 and 11 m, respectively) than the central parts (up to more than 60 m). The cross-sectional area at the southern sill (Fig. 1b) is much smaller (670 m^2) than the cross-sectional area at the northern sill (> 12 000 m^2). As will be shown, this has the consequence that less than half of the water entering the strait across the northern sill during the rising tide passes across the southern sill, on average. The remainder leaves the strait again across the northern sill during the ebbing tide as in a typical tidally driven fjord.

Secondly, the high mountains on both sides of the strait induce high precipitation rates and high runoff into the strait. On average, the naturally occurring daily runoff into the strait is 0.13 % of the volume between the sills. If the water in the strait were not continually replenished by saline ocean water, this amount of freshwater would lower the salinity by 0.3 psu per week, averaged over the total volume of the strait. Since the freshwater will tend to be concentrated in the uppermost

brackish layer, the effect on that layer will be even more and the runoff from a hydropower station adds to this natural freshwater supply. These features indicate that this body of water might behave more like an estuary than a strait, and hydrographic observations in the 1980s revealed that the stratification of the strait was highly variable, but often with a pronounced brackish top layer. This layer, which was typically 10 – 20 m deep, could be less saline than the oceanic water north of the strait by one psu or more. Also, it was observed that the bottom waters of the strait would often become stagnant during summer with reduced oxygen concentrations near the bottom as is common for Faroese sill fjords (Hansen, 1990). These characteristics were the motivation for using "fjord-like strait" in the title of this manuscript.

Thirdly, there is an amphidromic region on the Faroe shelf that is located close to Tórshavn (Fig. 1a), close to the southern sill of the strait (Hansen, 1978). Most of the attention has been given to the M_2-tide (Simonsen, 1992; Simonsen and Niclasen, 2021), but the amphidromic character of the region close to Tórshavn includes the other main semidiurnal constituents. Also the dominant diurnal constituents are low in this region (Supplementary Fig. S1). With a large difference in tidal amplitude between both ends of the strait, strong tidal currents should be expected and the flow across the southern sill may reach very high speeds according to local fishermen.

Thus, this strait experiences strong tidal forcing as well as estuarine (freshwater) forcing. In addition, the winds may be quite strong and might also affect the flow considerably. A priori, it is not clear, which of these forcing mechanisms dominate the flow and exchange within the strait, as well as with the surrounding waters. Although small compared to most other straits, Sundalagið Norður may therefore present an interesting case to study from a purely academic point of view. Added to that are questions of a more societal character. Along the coasts on both sides of the strait, a number of villages release sewage and other effluents into the water that may affect the natural biota in various ways. The strait is also hosting a fish farm and there is a potential for negative effects both on and from this activity, as well as interactions with other Faroese fish farming sites.

On this background, the main aim of this study was to understand how the different forcing mechanisms (freshwater, tidal, wind) combine to generate the physical conditions in the strait. More specifically, the aims are to clarify: 1) How the forcing mechanisms control the flow through the strait and its exchanges with waters outside the strait. 2) How the stabilizing effect of freshwater input competes with the de-stabilizing effects of tidal and wind forcing to affect the stratification in the strait. 3) What controls the renewal (flushing) rate of the waters in different parts of the strait.

To answer these questions, a numerical model is essential. Previous modelling efforts of the region have mainly been based on barotropic two-dimensional models (Simonsen and Niclasen, 2021; Kragesteen et al., 2018). Rasmussen et al. (2014) and Erenbjerg et al. (2020) have also reported results from full three-dimensional model simulations of the Faroe shelf, but both those models were too coarse to resolve the conditions in the strait.

We have therefore implemented a high-resolution model (32 m × 32 m horizontal, 35 vertical layers) that is one-way triply-nested (Supplementary Fig. S2) within a ROMS (Regional Ocean Model System) model covering a larger region (Lien et al., 2013). Due to limited computing resources, the high-resolution model was only run for 29 days. This period is too short to simulate the generation and decay of bottom layer stagnation. Instead, a period in January-February 2013 was

chosen, mainly because current velocity observations from two ADCP (Acoustic Doppler Current Profiler) deployments in the strait were available. The model was run for this period with realistic atmospheric forcing, but detailed runoff data were not available, so a constant freshwater supply was prescribed.

2 Material and methods

We define our "strait" to be the region between the two sills. The sills are defined by minimum cross-sectional (east-west) area and located at the red lines in Fig. 1b. The total volume between the sills is $2.31 \cdot 10^8$ m^3 with a surface area of $8.75 \cdot 10^6$ m^2.

2.1 Observations

During the simulation period, two upward-looking Acoustic Doppler Current Profilers (ADCPs) were deployed on the bottom of the strait (Fig. 1b). Details are documented in Larsen et al. (2014a, b). From 2012 to 2018 there were a high number of CTD (Conductivity Temperature Depth) observations in the strait, most of them documented in Simonsen et al. (2018). Unfortunately, no hydrographic observations were made during the simulation period. Sea level measurements are available from tide gauges at two sites "Eiði" and "Tórshavn" (Fig. 1a) from the Faroese Office of Public Works (Landsverk). These were sampled every ten minutes from 2009 to 2014.

2.2 The model

We have applied a model setup based on the open-source ROMS model (http://myroms.org, Shchepetkin and McWilliams, 2005; Haidvogel et al., 2008). This is a state-of-the-art three-dimensional hydrostatic, free-surface, primitive equation solving ocean model. ROMS applies generalized terrain following s-coordinates in the vertical and regular horizontal grids. This setup applies 32 m × 32 m resolution in the horizontal and 35 vertical layers. The triply-nested setup (Supplementary Fig. S2) is forced along the four open boundaries by SVIM (4 km × 4 km horizontal resolution, Lien et al., 2013). The first nesting has a resolution of 800 m in the horizontal and was run for the whole of 2013 (Erenbjerg et al., 2020). The second nesting contains a 160 m horizontally resolved grid and is run for five months in 2013. This second nesting is used as forcing for the ultra-high-resolution (32 m) setup used in our current study. The 32 m model has 682 grid point along the strait and 187 points in the perpendicular direction and covers a wider area, but we will focus on the region of the strait (Supplementary Fig. S3).

Atmospheric forcing is provided by the Weather Research and Forecasting (WRF) model on the surface. The WRF-model is set up with a configuration that has a resolution of 9-3-1 km in the horizontal and the area with 1 km × 1 km resolution covers the entire Faroe Islands. More detail on configuration can be found in Myksvoll et al. (2012).

No time series of runoff were available for the simulation period. Therefore, freshwater input to the strait from runoff is assumed to be constant in time and based on two reports: Erenbjerg (2020) and Davidsen et al. (1994) as well as data from

the local energy supplier. The two main freshwater sources are a hydropower plant on the eastern coast with average runoff 5.5 $m^3 s^{-1}$ and a river on the western coast with average runoff 2.0 $m^3 s^{-1}$ (Fig. 1b). These values were used as input to set up ROMS.

The computationally demanding high-resolution (32 m) model was run from the 11th of February until the 12th of March 2013. The starting date was two weeks after the start of the 160 m model, which started four weeks after its parent (800 m) model. Since the 160 m model has many mesh points within the strait, the starting conditions for the 32 m model should be approximately realistic so that the spin-up period ought to be relatively short. This is verified by inspection of the temporal evolution of parameters (especially kinetic energy) during the start period of the 32 m model. To avoid any remaining spin-up effects, results from the first day have nevertheless been omitted. Thus, the model output comprises 672 hourly values (from 12 February 01:00 to 12 March 00:00) of velocity and hydrographic parameters for each grid cell as well as sea level. This period will in the following be referred to as the "simulation period".

2.3 Model validation

2.3.1 Validation of tidal characteristics

The tidal forcing is an essential component of the dynamics of the strait and verification that the tides are adequately simulated is an important part of model validation. To check this, the characteristics (Amplitudes and Greenwich phase-lags) of the main tidal sea level constituents were determined from tide gauge observations at two locations, Tórshavn and Eiði (Fig. 1a), by harmonic analysis and compared with characteristics from simulated sea level close to these locations. One of the locations (Tórshavn) is outside the domain of the high-resolution (32 m) model. Therefore, the comparison was made with the 800 m parent model, which was run for a longer period and therefore also more suitable for harmonic analysis than the 32 m model. The U_TIDE software package, which is the Python adaption of the T_TIDE Matlab version (Pawlowicz et al., 2002), was used for the harmonic analysis. For better comparability, the analysis of the observed sea level data was made for the same period as for the simulated data.

For the observation-model comparison, the dominant three semidiurnal, two diurnal, two fortnightly, and two monthly constituents were selected (Table 1). At the location Eiði, there was good correspondence between observations and model for the two strongest constituents, M_2 and S_2, in strength (amplitude) as well as timing (Greenwich phase-lags). The correspondence for the other constituents at Eiði was not impressive. At Tórshavn, none of the constituents was very accurately simulated.

A priori, this might be used to conclude that the model does not simulate the tidal sea level variations in the area well. For the tidal forcing of the strait, the important aspect is, however, not the ability of the model to simulate individual constituents, but rather the strength and timing of the sea level difference between both ends of the strait. This difference will to a large extent be determined by the strength and timing of M_2 and S_2 at Eiði since the amplitudes of these constituents are much larger than the other amplitudes in Table 1. For our purposes, the tidal forcing of the strait, thus, is fairly accurately

simulated by the model, although the difference in Greenwich phase-lag for M_2 at Eiði (19° equivalent to 39 minutes) and other differences imply a timing bias in the model, which ought usually not to exceed one hour.

Table 1. Amplitudes and Greenwich phase-lags, as determined by harmonic analysis, for nine tidal constituents (Const.) of sea level variation at two locations (Tórshavn and Eiði, Fig. 1a) as observed at tide gauges (Obs.) and as simulated at grid points close to the locations by the 800 m parent model (Model). The harmonic analysis was for the period 1 January 2013 to 1 October 2013 for both the observed and the simulated sea level. For the semidiurnal and diurnal constituents, the periods are listed in hours (h.). For the long-period constituents, they are listed in days (d.).

Const.	Period	Tórshavn				Eiði			
		Amplitude		Greenw. phase-lag		Amplitude		Greenw. phase-lag	
		Obs.	Model	Obs.	Model	Obs.	Model	Obs.	Model
M_2	12.42 h.	9.3 cm	3.2 cm	195°	162°	57.9 cm	59.6 cm	249°	268°
S_2	12.00 h.	5.1 cm	4.0 cm	214°	193°	19.9 cm	21.1 cm	283°	285°
N_2	12.66 h.	1.8 cm	0.1 cm	170°	277°	12.2 cm	4.0 cm	225°	10°
K_1	23.93 h.	4.4 cm	2.6 cm	139°	251°	9.3 cm	7.3 cm	159°	289°
O_1	25.82 h.	7.2 cm	3.9 cm	52°	315°	7.2 cm	3.5 cm	12°	269°
Mf	13.66 d.	2.7 cm	2.0 cm	179°	213°	2.0 cm	1.9 cm	173°	215°
MSf	14.78 d.	3.1 cm	2.2 cm	172°	190°	2.9 cm	2.4 cm	146°	193°
Mm	27.59 d.	3.2 cm	1.2 cm	186°	163°	2.9 cm	1.2 cm	184°	153°
MSm	31.81 d.	4.0 cm	2.3 cm	269°	249°	4.1 cm	2.0 cm	262°	247°

2.3.2 Comparison of simulated and observed current velocity

The two ADCPs were located on a transect crossing the strait (Fig. 1b), but high-quality data (Larsen et al., 2014a, b) were only obtained for the deep parts of the velocity profiles (Fig. 2a). When averaged over the simulation period, simulated and observed cross-strait profiles are similar and close to zero (Fig. 2b and 2c). For mooring site BW (Fig. 2b), the average simulated and observed along-strait profiles are also fairly similar for the depths reached by the ADCP. For mooring site BE (Fig. 2c), the discrepancy is larger.

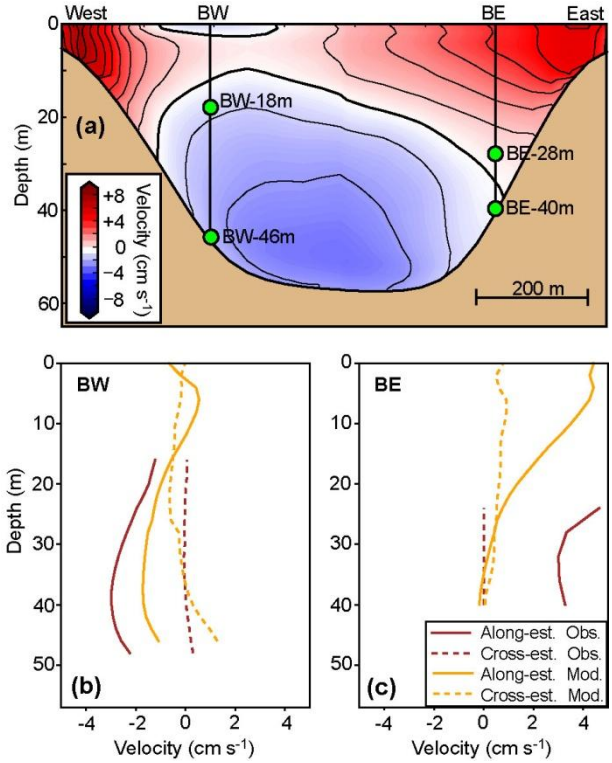

Figure 2. (a) The background colours show simulated northward velocity along transect labelled "ADCP" in Fig. 1b averaged over the simulation period. The two vertical lines labelled "BW" and "BE" indicate the locations of two ADCPs moored on the bottom and green circles indicate the uppermost and lowermost depths with high-quality measurement for each of the ADCPs. **(b)** and **(c)** Velocity profiles along the strait (continuous curves, positive towards north) and across it (dashed curves, positive towards east) from the ADCP measurements (dark curves) and the model (light curves) at the two mooring sites averaged over the simulation period.

To evaluate the simulation of temporal velocity variations, Hovmøller diagrams may be used to illustrate the hourly variations of along-strait velocity with depth and time at the two ADCP sites (Supplementary Fig. S4). These diagrams show some similarities between observations and model, but also some differences. A more objective evaluation is presented in Fig. 3, which compares along-strait velocities at two depths for each ADCP site. Although the strength of the tidal forcing is well simulated by the model, as argued above, the timing of flood and ebb may be off by roughly an hour (Table 1). This is not important for understanding the dynamics of the strait, but will affect a direct comparison (correlation) of observed and simulated hourly velocities negatively.

Figure 3, therefore, does not compare hourly velocities directly. Instead, the top panels in the figure compare observed and simulated along-strait velocities averaged over consecutive 25-hour periods while the bottom panels compare the standard deviations within the same 25-hour periods. The length of this period is roughly twice the period of the M_2 constituent and intermediate between the K_1 and O_1 constituents. The top panels of the figure, thus, compare the long-term (longer than daily) variations of along-strait velocity averaged over a diurnal tidal period, while the bottom panels compare

the magnitudes of the variations within a diurnal tidal period, which include the neap-spring variations in the strength of the tidal current.

The observed and simulated velocities in Fig. 3 are certainly not identical, but they are generally of the same magnitudes. All of the correlation coefficients are also positive and six out of eight are significantly higher than zero at the 95 % level ($p < 0.05$). Although the observations do not validate the model in detail, they do exhibit similarity to the simulations and there is no indication that the model generates unrealistic velocities. Since the ADCP data did not reach into the upper layers with strong tidal currents, they do not provide a strong test of the simulations.

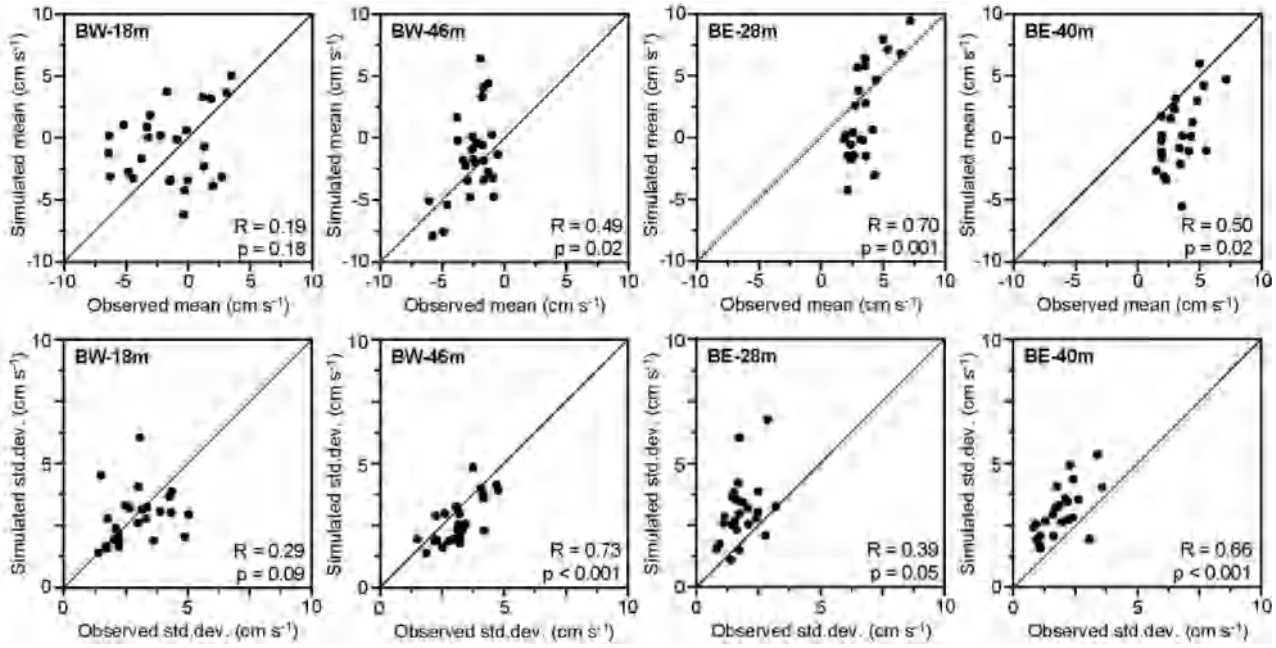

Figure 3. Comparison between observation and model for averages (top panels) and standard deviations (bottom panels) of along-strait velocity for consecutive 25-hour periods at two measurement depths for each of the ADCP sites (Fig. 2a) during the simulation period. Correlation coefficients (R) and their statistical significances (p) are listed in the lower right corner of each plot. Diagonal lines indicate equality between model and observation.

2.3.3 Comparison of simulated and observed salinity

No hydrographic observations were made during the simulation period. Instead, the data from all the CTD observations in the strait 2012 – 2018 were collected (Simonsen et al., 2018). In the shallow regions on either side of the strait, detailed bottom topography and proximity to a river outlet may affect the salinity disproportionately. We therefore considered only CTD casts with bottom depth at least 50 m. To exclude situations with a stagnant bottom layer, only observations from winter (November – April) were used (Supplementary Fig. S5).

At a first glance, the correspondence between observed and simulated salinity is not impressive and might indicate too strong mixing in the model. The model was, however, run with nearly constant freshwater supply. Therefore, it cannot be

expected to simulate periods with excessive runoff that are frequent in the Faroese winter and likely to have caused the observed CTD profiles in the figure with very low salinities in the top 10-20 m layer.

2.4 Statistical methods

The statistical significance of correlation coefficients has been corrected for serial correlation by the "modified Chelton" method recommended by Pyper and Peterman (1998).

3 Results

3.1 Hourly variations

To structure the presentation, Fig. 4a defines a few key time series of volume transport and sea level that are sampled hourly. The volume transports are across the northern sill, q_N, and the southern sill, q_S, respectively, where positive values indicate northward volume transport and negative values indicate southward transport. They are calculated by integration of simulated northward velocity across each of the sill sections taking sea level variations into account. The sea level time series are all cross-strait averaged.

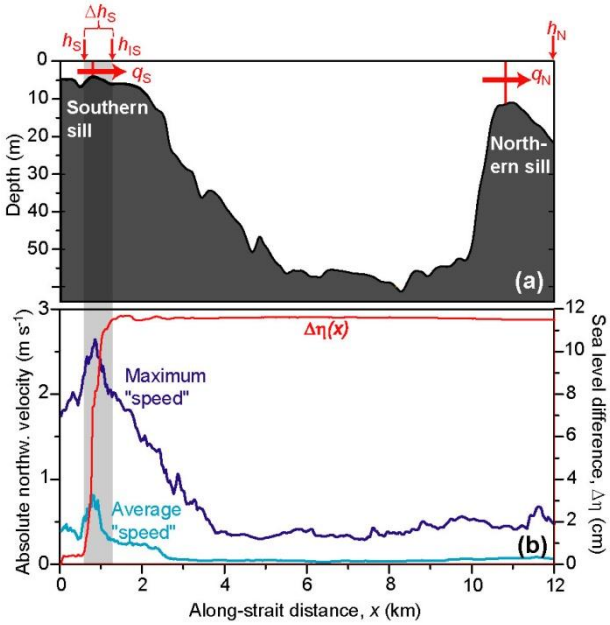

Figure 4. (a) Locations for sampling key time series. **(b)** The cyan and dark blue curves show the along-strait variation of maximum (dark blue) and (temporally) averaged "speed", defined as the absolute value of the cross-strait averaged along-strait velocity component. The red curve shows the standard deviation, $\Delta\eta(x)$, of the sea level difference between the southernmost part ($x = 0$) and a given location, x.

On hourly time scales, the flow through the strait is clearly dominated by the tides. This is evident in Fig. 5a, which shows the simulated hourly variations of volume transports across both the northern, q_N, and the southern, q_S, sill during the

4-week simulation in 2013. The semidiurnal variation is clear in the hourly values, as is a fortnightly variation in the amplitude of the transport. The amplitude of the transport across the northern sill is much higher than the amplitude in transport across the southern sill. From a regression analysis, the highest correlations are found when q_S lags one hour after q_N, and the amplitude ratio is then 0.46 (Table 2). As mentioned in the introduction, this implies that most of the water entering the strait from the north will return northwards like in a tidally driven fjord.

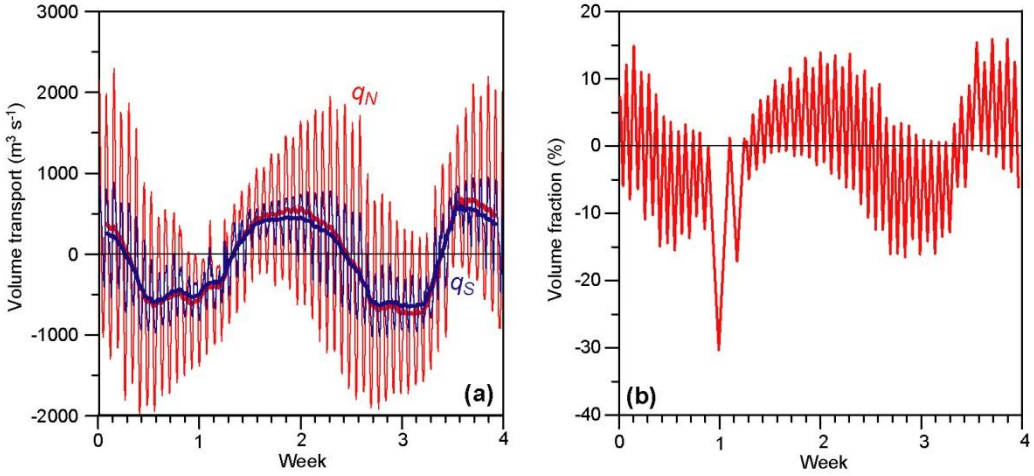

Figure 5. (a) Hourly (thin lines) and 25-hour averaged (thick lines) simulated northward volume transport across the northern sill, q_N, (red) and across the southern sill, q_S, (blue). **(b)** Fraction of total volume transported into (positive) or out of (negative) the strait across the northern sill during each uni-directional period.

Most of the time, the volume transport changes sign four times a day, as would be expected with semidiurnal tidal forcing, although there are a few cases with unidirectional flow lasting more than a day. Adding up all the water flowing into or out of the strait across the northern sill during one of these tidal phases, we find that this typically is around 10 % of the volume, but occasionally the phases may last longer and transport more water, such as the period by the end of the first week of simulation where an episode of excess southwards flow flushes 30 % of the volume out (Fig. 5b).

Sea-level variations also follow the tidal cycle. Figure 4a shows three locations, from which hourly sea level time series have been sampled: h_N is sea level north of the northern sill. h_S is sea level south of the southern sill. h_{IS} is sea level just north of the southern sill. In addition, h_I is sea level averaged over all surface grid points between the two sills.

Correlation coefficients (R) between some of these time series are listed in Table 2. Average sea level between the two sills, h_I, is very highly correlated with sea level north of the strait, h_N, with zero lag (less than one hour) and a regression coefficient (α) close to one. Even h_{IS}, just north of the southern sill (Fig. 4a), follows h_N almost identically. Thus, sea level within the strait responds more or less instantaneously to the sea level north of the strait. Sea level south of the strait, h_S, is also highly correlated with h_N, but with a smaller regression coefficient (Table 2).

Hourly values for volume transport across the two sills are fairly well correlated with the difference in sea level between both ends of the strait, $h_N - h_S$, consistent with the idea that this difference drives the flow through the strait. The

regression factor, α_{max}, is considerably smaller for q_S than for q_N, which again is consistent with weaker flow across the southern sill than the northern. This difference may be linked to the energy balance in the strait as illustrated in Fig. 4b. The cyan and dark blue curves in that figure demonstrate that the cross-strait averaged speed (and kinetic energy) is much higher over the southern sill than elsewhere in the strait. The red curve shows the along-strait variation of the parameter $\Delta\eta(x)$, which is defined as the typical value (standard deviation) of the sea level difference between the southern end of the strait and the location x. This value should be proportional to the typical difference in potential energy between the two locations. As seen in Fig. 4b, this difference remains almost constant throughout most of the strait with most of the change occurring over a relatively short distance over the southern sill with the highest speeds.

Table 2. Lagged correlation and regression analysis of relationships between hourly values of various simulated time series where t represents time. R_0 is the correlation coefficient for zero lag. Lag_{max} is the lag (in hours) that gives the numerically highest correlation coefficient. R_{max}, α_{max}, and β_{max} are the correlation coefficient and the regression coefficients for that lag.

Regression equation	R_0	Lag_{max}	R_{max}	α_{max}		β_{max}	
$q_S(t+lag)=\alpha \cdot q_N(t)+\beta$:	0.84	1	0.87	0.46		-36	$m^3\ s^{-1}$
$h_I(t+lag)=\alpha \cdot h_N(t)+\beta$:	>0.99	0	>0.99	1.01		0.04	m
$h_{IS}(t+lag)=\alpha \cdot h_N(t)+\beta$:	>0.99	0	>0.99	1.01		0.01	m
$h_S(t+lag)=\alpha \cdot h_N(t)+\beta$:	0.96	0	0.96	0.89		0.00	m
$q_N(t+lag)=\alpha \cdot [h_N(t)-h_S(t)]+\beta$:	-0.88	0	-0.88	-7606	$m^2\ s^{-1}$	346	$m^3\ s^{-1}$
$q_S(t+lag)=\alpha \cdot [h_N(t)-h_S(t)]+\beta$:	-0.94	0	-0.94	-4349	$m^2\ s^{-1}$	165	$m^3\ s^{-1}$

It seems likely that the high kinetic energy over the southern sill is fed by this loss in potential energy. In a simple conceptual model where the speed over the southern sill at any given time, v_S, is assumed not to vary spatially on the cross-section, energy conservation may be expressed more rigorously by a modified Bernoulli equation:

$$½ \cdot \rho \cdot v_S^2 = ½ \cdot \rho \cdot v_U^2 + g \cdot \rho \cdot \Delta h_U - W_{friction} \qquad (1)$$

where the first term on the right hand side of Eq. (1) is the kinetic energy upstream, which is small and may be ignored. In the next term, Δh_U is the sea level difference between the sill and the region upstream, which is either north of or south of the sill, depending on the direction of flow. The last term, $W_{friction}$, is the work done by friction on a water parcel of unit volume. The volume transport is given as $q_S = A \cdot v_S$, where A is the cross-sectional area over the sill, which is assumed to be constant (= 670 m^2). If no energy is lost to friction ($W_{friction} = 0$), this leads to the equation in the upper right hand corner of Fig. 6.

To get a common framework for both flow directions, Δh_U may be expressed in terms of the sea level difference across the entire southern strait, Δh_S (Supplementary Fig. S6). The locations for defining Δh_S are chosen from Fig. 4 as the interval over which $\Delta\eta(x)$ and therefore also the potential energy typically exhibit their main change. This energy-based framework is tested in Fig. 6. Each black point in that figure represents simulated values for Δh_S and q_S for one hour, while the red curve is a least squares fit of the equation in the figure to the simulated values where the parameter γ has been varied to minimize the squared error.

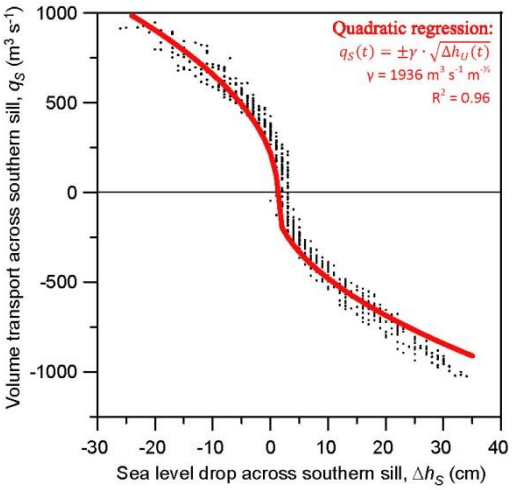

Figure 6. Volume transport across the southern sill, q_S, plotted against sea level change across the southern sill, Δh_S. Each black point represents one hour in the model simulation. The red curve represents the result of a least squares fit to the red equation shown in the upper right hand corner (quadratic regression). The quadratic fit (red curve and equation) explains 96 % of the variance of q_S.

The fitted expression (red curve) in Fig. 6 appears to represent the simulated values (black points) fairly well, but the value for γ that gives the best fit, 1936 $m^3\ s^{-1}\ m^{-½}$, is considerably smaller than given by theory with no friction, $\gamma = A \cdot \sqrt{2g}$ = 2969 $m^3\ s^{-1}\ m^{-½}$, which indicates that friction cannot be ignored. In the model setup, bottom stress was parameterized to depend on the square of the speed. The work done by bottom friction over a given distance may therefore also to a good approximation be proportional to v_S^2 just as the kinetic energy. In that case, the red equation in Fig. 6 will remain valid with a lower value for γ. In this interpretation, only 43 % of the potential energy is converted to kinetic energy with the rest lost to friction over the southern sill, although this result will depend on the model setup.

3.2 Long-period variations

The fortnightly variation of tidal transport amplitude seen in Fig. 5a is a normal phenomenon in Faroese waters (Hansen, 1978), reflecting the variation between neap and spring tides. The net volume transports, averaged over a diurnal tidal period of 25 hours do, however, also exhibit fairly large long-period (dominant fortnightly) variations (thick lines in Fig. 5a). These variations are further illustrated in Fig. 7, which shows two types of parameters. The symbols that are enclosed in brackets (< >) have been averaged over 25 hours, whereas those that are labelled "std( )" show standard deviations within each 25 hour interval, which should reflect the amplitude of the combined tidal variations from all the semidiurnal and diurnal constituents.

As seen in Fig. 7a, the simulation period includes two full periods with net southward flow and one period with net northward flow, all of them lasting about one week. This figure also has a curve (black) that shows the variation of the standard deviation of q_N over consecutive 25-hour intervals. It shows that the 25-hour average transport does not reach its extremes during spring tide, but rather a few days out of phase (Fig. 7a).

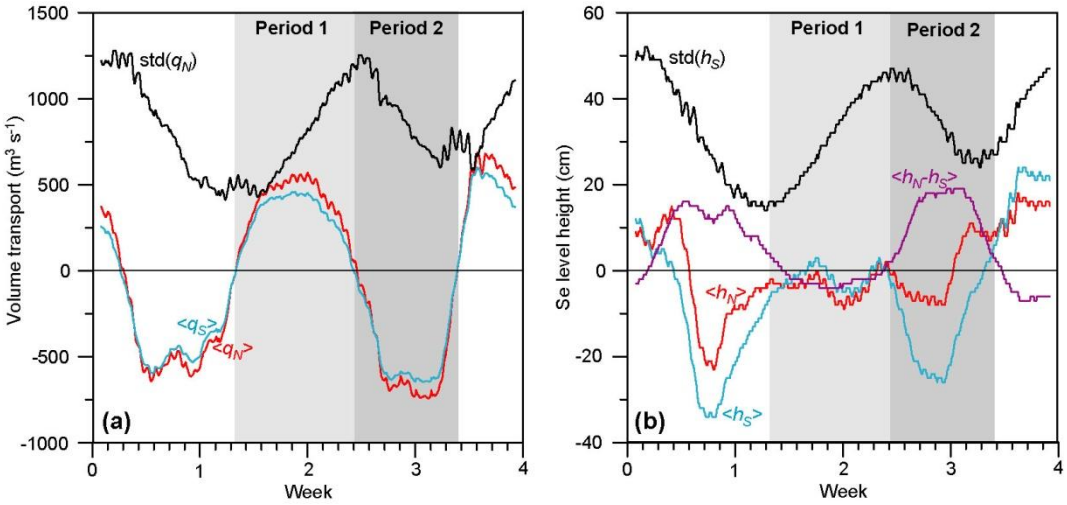

Figure 7. Daily (25-hour) averages (<>) and standard deviations (std) within each 25-hour period for **(a)** volume transports and **(b)** sea level heights. The standard deviations ought to be dominated by the strength of the tidal amplitudes and should therefore reflect the variation between spring and neap tides. The shaded areas indicate two periods discussed in the text: "Period 1" lasting 188 hours from 21 February 08:00 to 1 March 03:00 and "Period 2" lasting 158 hours from 1 March 04:00 to 7 March 17:00.

To help understand the long-period transport variations, Fig. 7b shows 25-hour averages and standard deviations of sea level height. During the periods with average southward transport, average sea level is higher north of the strait. When the average transport is northward, the average sea level is higher south of the strait. Consistent with Table 2, the volume transport through the strait may be seen as forced by the sea level difference between both ends. In this paradigm, the reason for the long-period variations in volume transport is the variation in this sea level difference.

Figure 8 shows the selected two full periods of northward and southward flow, respectively. Period 1 is the first full period with average northward flow, whereas Period 2 is the following period with average southward flow. To illustrate the differences between these two periods (and to the whole-period averages, Supplementary Fig. S7), northward velocity and salinity are averaged over each period and across (east-west) the strait and then plotted against along-strait distance and depth in Fig. 8.

During period 1 (upper panels in Fig. 8), the average flow is northwards through the upper parts of the strait, down to 20−30 m depth except for the water over the northern sill. This indicates that during this period the upper parts of the strait are refilled by the water entering from the south. In the bottom part of the strait, Period 1 has average southward flow. Across the northern sill a thin layer of seawater is entering the sill with a velocity of up to 2 cm s^{-1} on average. This denser water manages to descend towards the bottom of the basin before losing its excess density due to mixing and continues southwards at depth.

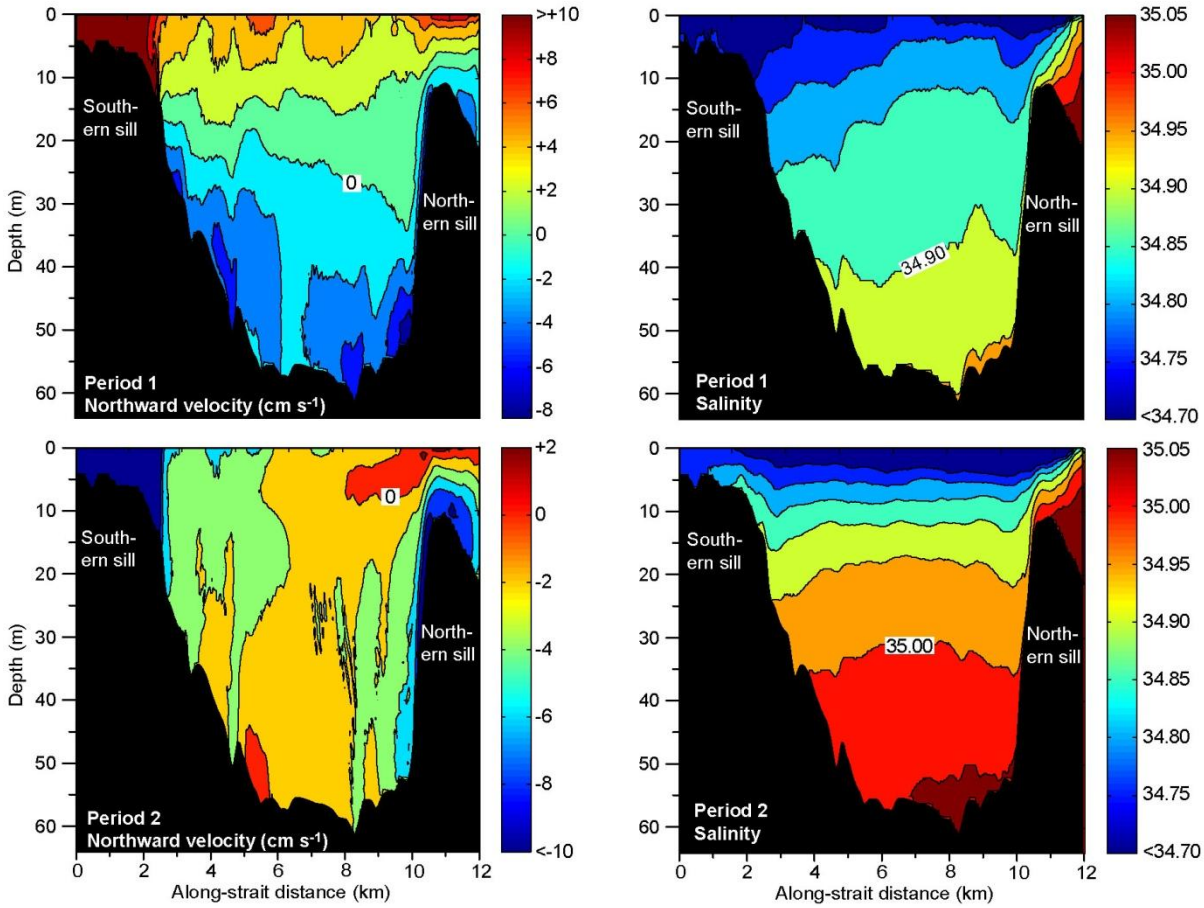

Figure 8. Cross-estuary averaged northward velocity and salinity plotted against along-strait distance for the two different periods defined in Fig. 7. For velocity, the most positive (top left panel) or negative (bottom left panel) values are grouped together. Note different velocity scales. For salinity, the lowest values are grouped together. The bottom depth indicated by the black areas is the maximum depth along each section crossing the estuary.

During Period 2 (lower panels in Fig. 8), the average velocity is southwards throughout most of the strait and does not exhibit the fjord-like two-layer circulation of Period 1. The salinity distribution during Period 2 also differs markedly from that of Period 1 with stronger salinity stratification. Since the high-salinity source north of the north of the strait and rate of freshwater supply are almost identical, these differences must be caused by the differences in circulation and mixing.

The difference between the deep flows during the two periods is illustrated in the period-wise averages in Fig. 9, showing volume transport below sill depth of the northern sill (11 m). From this figure it is clear that the volume transport through the deep parts of the strait is much greater during Period 2. This difference is likely one of the main causes of the difference in salinity distributions between the two periods (Fig. 8) and will have a substantial effect on the flushing rate of the deep waters in the strait as will be discussed in Sect. 4.

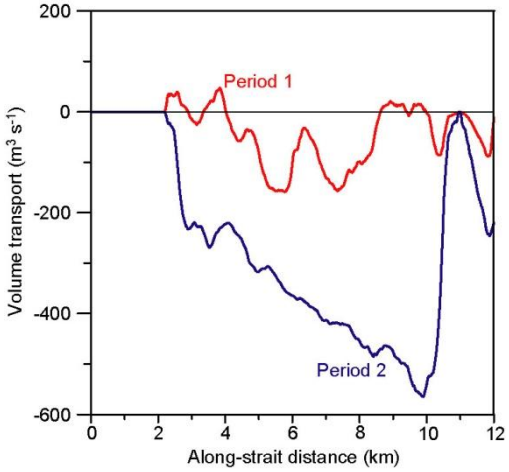

Figure 9. Northward volume transport through (east-west) cross-sections below sill depth of the northern sill (from 12 m, downwards) for the two different periods indicated in Fig. 7.

3.3 Observational validation of long-period variations

To check that the long-period variations in average transports and sea level differences (Fig. 7) are not purely an artefact generated by the model, we have used the characteristics (amplitudes and Greenwich phase-lags) of tidal constituents derived from tide gauge observations at Eiði and Tórshavn (Fig. 1a) in Table 1 to calculate time series of sea level at the two locations. When averaged over 25 hours, the sea level at both sites is dominated by atmospheric pressure variations (Supplementary Fig. S8), but this effect is strongly reduced when the difference between both locations is considered.

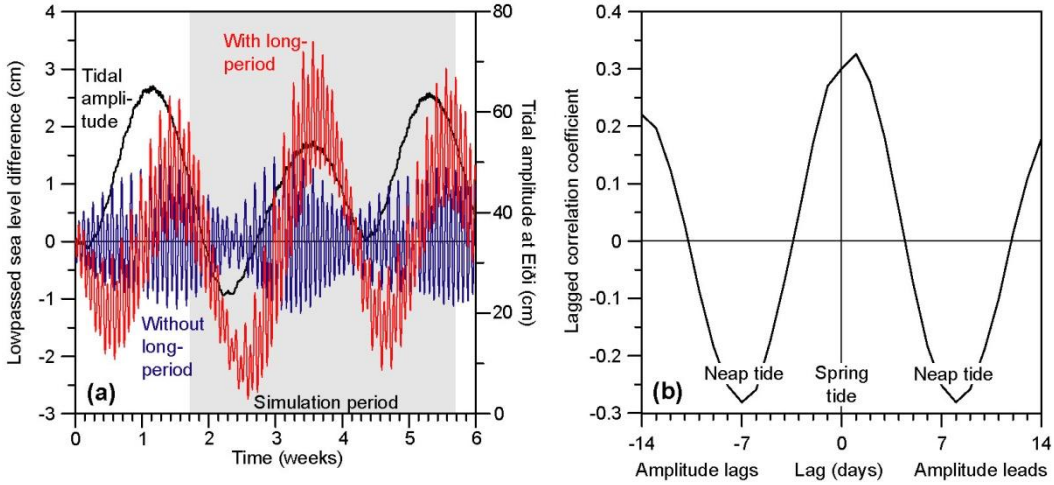

Figure 10. (a) Lowpassed (25-hour averaged) sea level difference between Eiði and Tórshavn (Eiði minus Tórshavn) calculated from the "observed" amplitudes and Greenwich phase-lags in Table 1 for a six-week period starting 1 February 2013. The blue curve (left y-axis) is generated by using only the five semidiurnal and diurnal constituents in the table. The red curve (left y-axis) is based on all the constituents including the four long-period constituents. The black curve (right y-axis) shows the tidal amplitude at Eiði defined as the standard deviation of sea level for each 25-hour interval. The gray-shaded area indicates the simulation period. **(b)** Lagged correlation coefficient between 25-hour averaged difference in observed sea level between Eiði and Tórshavn and the tidal amplitude in Eiði based on observed sea level (tide gauge measurements) for the 2009-2014 period.

345

The sea level difference between Eiði and Tórshavn generated in this way therefore ought to be a fair representation of the tidal forcing of the strait and the 25-hour average of this difference (Fig. 10) should reflect the forcing of long-term (longer than a day) variations based on observations. When only semidiurnal and diurnal constituents are used to generate
350 the sea level difference (blue curve in Fig. 10a), the 25-hour averaged difference exhibits long-period variations. They are the residuals of the averaging that come because none of the constituents have periods exactly equal to 25 hours or half of that. The long-period variation of these residuals is, however, only in the magnitude of their deviation from zero and they change sign several times over a day. Only when the long-period constituents are included (the red curve in Fig. 10a), does the difference exhibit a similar behaviour to Fig. 7b with week-long periods of the same sign.

355 Ideally, the curve for $<h_N - h_S>$ in Fig. 7b should be identical to the red curve in Fig. 10a within the shaded area (simulation period), but there are clear differences both in timing and magnitude. This was to be expected from Table 1, which shows substantial differences between observed (Obs.) and simulated (Model) values for both amplitudes and Greenwich phase-lags for the long-period constituents. In the harmonic analyses of Table 1, the relative uncertainties in amplitude for the long-period constituents are typically 50 % or higher while the uncertainties of the Greenwich phase-lags
360 range between 30° and 90°. The differences between observation and model for the long-period constituents are therefore within the uncertainties of the harmonic analyses.

With so large uncertainties, we should not expect identical curves in Fig. 7b and Fig. 10a, but they also raise the question whether the signal is real. To address that question, Fig. 10b shows a lagged correlation plot between the observed 25-hour averaged sea level difference between Eiði and Tórshavn and the amplitude of the tidal variation at Eiði based on
365 tide gauge observations from the two locations for the whole 2009-2014 period. For zero lag, the correlation coefficient is positive (R = 0.30). This may perhaps be explained by the residuals from 25-hour averaging of semidiurnal and diurnal constituents, which should be in phase with the amplitude of the tidal variation at Eiði. The correlation coefficient is slightly higher (R = 0.33) for a positive lag of one day, which is similar to the red curve in Fig. 10a where the highest positive values of low-passed sea level difference lag after the largest tidal amplitude. Most notable are, however, the negative correlation
370 coefficients for lags of ± 7 days, which again is consistent with the red curve in Fig. 10a. All of these correlation coefficients are highly significant ($p << 0.001$) and verify that the long-period variation illustrated by the red curve in Fig. 10a is not generated by uncertainties in the harmonic analyses.

From this, it seems clear that the long-term variations in Fig. 7 are real and that they are caused by the long-period constituents, mainly the four that are listed in Table 1. Possibly, these variations are enhanced in the model simulations
375 relative to nature, but that is difficult to assess without better observational evidence of the sea level variations, especially for the amphidromic region south of the strait.

3.4 Density inversions downstream from the northern sill

From the salinity distributions in the right hand panels of Fig. 8, it seems that the seawater entering the strait across the northern sill is flowing downwards and is then mixed with the water inside the strait just downstream of the sill. To study this in more detail, the density structure was plotted along a track (Fig. 11a). The track was chosen based on the average maximum velocity close to the bottom, beginning on the shallow part of the sill (track number 0) down-slope to 55 m depth (track number 35). The average velocity during the entire simulation period is more than 10 cm s^{-1} southwards in the bottom layer on the steep slope of the track (Fig. 11d).

As long as turbulent mixing is weak, the density structure is normally stable with density increasing downwards. Density inversions with density decreasing downwards may therefore be used as a sign of mixing. To utilize this, we define a "density inversion" as the density difference between the third lowest layer and the bottom layer (upper minus deeper) when this value is positive. Under stable conditions, when this value is negative, it is set to zero. The spatial and temporal variations of density inversions along the selected track are illustrated on the Hovmøller diagram in Fig. 11b.

If the density inversions are averaged over the track and temporally smoothed, they exhibit systematic variations (red curve in Fig. 11c). Most pronounced is the rather frequent occurrence of inversions in the first part of the simulation from day two to nine. From day nine to fifteen, the density inversions are less frequent for most part of the track except for track points 20-25. These variations show some similarity to the variations in Fig. 7a as verified by the blue curve in Fig. 11c. Strong southward flow across the northern sill seems to be a necessary – but not sufficient – condition for density inversion. When averaged over time, the density inversions mainly occur on the down-hill slope, and are maximal right before the bottom slope levels off at track number 20, Fig. 11e.

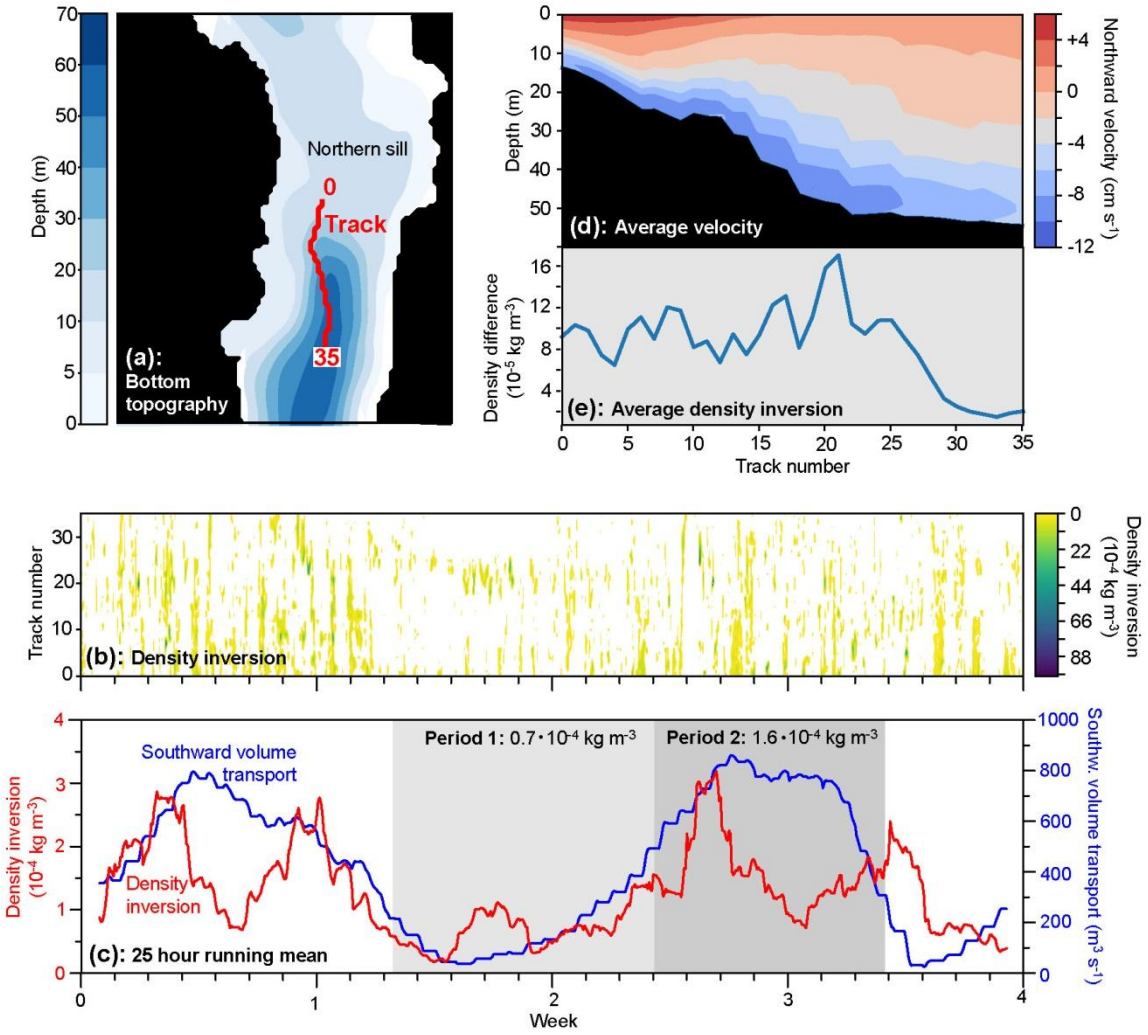

Figure 11. (a) Bottom topography around the northern sill. The red line shows a track with numbers ranging from 0 to 35, which are used in the other panels. **(b)** Density inversion, defined as density (σ_θ) difference between the deepest layer and two layers above (layer 2 minus layer 0) along the track every hour. Only positive values are shown (negative values white). **(c)** The red curve shows the density inversion in the panel just above averaged over all track numbers and 25-hour running mean. The blue curve is 25-hour running mean of southward-directed volume transport (positive towards the south) across the northern sill (set to zero for hours with northward transport). The shaded areas indicate the two periods defined in Fig. 7 with average density inversion for each period shown. **(d)** Average northward velocity at various depths along the track. **(e)** Density inversion along the track averaged over the whole period.

4 Discussion

4.1 Model performance

The comparison between tidal constituent characteristics as observed by tide gauges and simulated by the parent (800 m) model verified that the main constituents, which dominate the tidal forcing, were well simulated. The average velocities in the simulation and in observations (Sect. 2.3) did not show identical values, but taking into account the spatial variation (Fig.

2a), the correspondence is as good as may be expected. For temporal velocity variations, most of the correlations between model and observations (Fig. 3) were significant at the 95 % ($p < 0.05$) level, which again is encouraging.

For the 800 m parent model, a comprehensive validation against hydrographic observations was performed (Erenbjerg et al., 2020), but no hydrographic (CTD) observations were made during the simulation period of the 32 m model. Instead, salinity profiles from the simulation and from historical CTD data were compared (Supplementary Fig. S5). The correspondence between these two data sets was not impressive and may perhaps indicate that the model has too strong mixing. The model was, however, run with constant runoff rate and can therefore not be expected to reproduce the periods with excessive runoff that occur in nature. This aspect of the model setup was unfortunate in terms of model validation, but it has the benefit that it excludes variations in freshwater supply as cause of the long-period variations in salinity distribution (Fig. 8) and estuarine characteristics.

4.2 Hourly variations

On short time scales, the flow through the strait is clearly of tidal character with semidiurnal dominance (Fig. 5a) and we expect sea level differences between both ends to be the main driving force. This is supported by the high correlations between volume transports across the sills, q_N and q_S, and sea level difference $h_N - h_S$ (Table 2).

As the tidal wave enters the strait from the north, it should propagate southwards as a barotropic wave with sufficient speed to pass through the strait in less than half an hour. This is verified by the high zero-lag correlations between h_N, h_I, and h_{IS} (Table 2). The indication of a one-hour lag between q_N and q_S in Table 2 seems strange when all the other time series in the table vary in phase. With data that are sampled every hour, an apparent one-hour difference in lag may, however, be much smaller.

In the model simulations, most of the sea level change occurs over a fairly short distance over the southern sill and this is where the highest speeds are observed (Fig. S4b). Speeds exceeding 2.5 m s^{-1} might seem excessive, but according to local sailors, the speeds over the southern sill may occasionally be considerably higher. From the arguments supporting the quadratic fit in Fig. 6, it appears that roughly half the potential energy in the sea level is lost to friction and from the red curve in Fig. 4b, this loss is over a short distance across the southern sill. Thus, friction over the southern sill probably controls how much water the tides can push through the strait and gives the strait its fjord-like character.

4.3 Long-period variations

As demonstrated in Fig. 5 and Fig. 7, long-period (dominant fortnightly) variations are seen; not only in the tidal amplitude, but also in 25-hour averaged volume transport. Is this an artefact of the processing? On the Faroe shelf, the tides are dominated by semidiurnal and diurnal variations that vary in amplitude over a fortnightly period, mainly as an interference between the M_2 tide (period 12.42 hours) and the S_2 tide (period 12 hours). For these variations, a 25-hour mean will average out close to zero. There will be a residual, but it should not exceed the maximum tidal amplitude divided by 25. We expect this residual to vary in phase with the strength of the tidal amplitude.

The simulated variations in 25-hour averaged volume transport are much larger than this expected residual. At times, the 25-hour averaged transport equals the standard deviation of the transport during the same 25 hours and the average transport is not in phase with the amplitude (Fig. 7a). In Sect. 4.2, we argued that the hourly variations in volume transport were forced by sea level differences between the northern and southern ends of the strait. From Fig. 7b, it appears that the same mechanism may be invoked for the 25-hour averaged transport. Periods with average southward transport have average sea levels higher north of the strait than south of it and vice versa.

With this interpretation, the problem is transferred to explaining why there are long-period variations in the 25-hour averaged sea level difference between both ends of the strait. A priori, this might be an artefact generated by the model, but Fig. 10a verifies that the long-period variations are real and caused by the dominant fortnightly and monthly tidal constituents (Mf, MSf, Mm, MSm). The similarity between Fig. 7b and Fig. 10a is not perfect. The observed signal in sea level difference (Fig. 10a) is smaller than indicated by the model (Fig. 7b). We should, however, not expect perfect similarity, because Tórshavn is rather far south of the southern end of the strait (Fig. 1a) and in an amphidromic region with large spatial changes.

According to the 800 m parent model simulations, the amplitudes of all the dominant long-period constituents exhibit considerable spatial variations over the Faroe shelf and surrounding areas (Supplementary Fig. S10). To some extent, these variations may be artificial and caused by atmospheric pressure variations that may contaminate the harmonic analysis of long-period constituents for short time series. The lagged-correlation analysis of observed sea level difference between Eiði and Tórshavn (Fig. 10b) does, however, verify the signal independently of harmonic analysis. The positive zero-lag (spring tide) correlation in Fig. 10b could conceivably be caused by residuals from the semidiurnal and diurnal constituents, but the highly significant negative correlations at lags of ± 7 days (neap tide) are hard to explain without involving the long-period constituents. We therefore conclude that the effects of the long-period tides on the strait are real, although possibly enhanced in the model simulations.

Since southward flow across the southern sill occurs during flood, it has been suggested that the cross-sectional area over the sill – and therefore also volume transport – should be higher during southward than northward flow, which would lead to a net southward volume transport varying between 50 and 175 $m^3 s^{-1}$ in phase with the strength of the tidal amplitude (VandKvalitetsInstitutet, 1983). To check whether this is supported by the model simulations, volume transport across the southern sill was calculated from the simulated velocities and sea levels with and without varying sea level. On average, the difference was 14 $m^3 s^{-1}$. Thus, the effect is real, but much smaller than expected and swamped by the long-period variations.

4.4 Exchange rates/ flushing rates

For a water body that is affected by human activity, one of the most important parameters is the flushing rate, i.e., how fast the waters (and dissolved contaminants or planktonic organisms) are flushed out of it. An often used measure of this is the "flushing time", defined as the volume of the water body (or parts of it) divided by the volume transport into or out of it.

Combining CTD observations from our strait with estimated freshwater supply, Hansen (1990) estimated a typical flushing time of 5 days for this strait, but noted the high uncertainty of this value.

From the present model results, there are several ways of obtaining alternative estimates. One way is to use Fig. 5b, which implies that between 5 and 10 % of the volume is typically flushed in and out over the northern sill every 12 hours. If one assumes no mixing between in-flowing and out-flowing waters, this method gives an average flushing time for the strait as a whole of around one week, ranging between less than four days and more than 11 days over the simulation period (Supplementary Fig. S9).

Alternatively, one could use the average salinity distribution (Supplementary Fig. S7) to estimate the average total freshwater content in the strait and combine that with the (almost constant) freshwater supply to calculate a flushing time. This method is, however, very sensitive to the choice of salinity for the "pure" seawater that enters the strait across either of the sills and also assumes stationary conditions.

An extra challenge when trying to estimate a "typical" flushing time is the long-period variation in the net flow through the strait (Sect. 4.3). Considering the two periods defined in Fig. 7, Figure 12 illustrates the two different exchange regimes that the strait regularly shifts between.

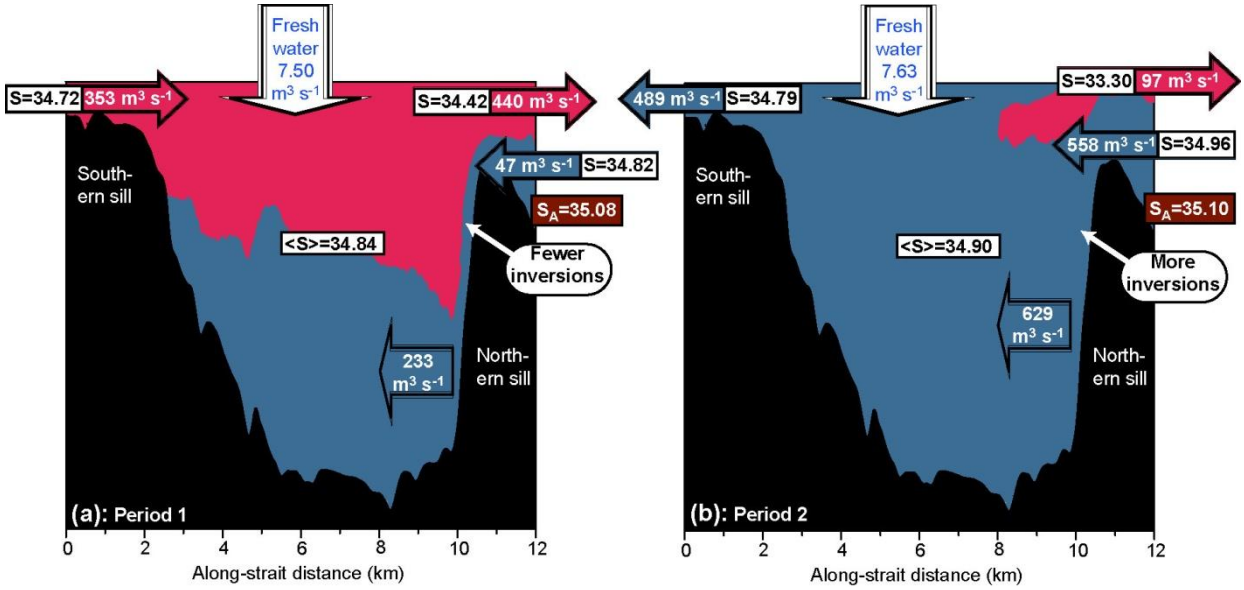

Figure 12. Schematic flow patterns and exchanges for the two periods defined in Fig. 7. Red and blue areas show north- and south-going (cross-estuary averaged) flow, respectively (based on Fig. 8). Horizontal arrows over the two sills show average volume transport and (transport-averaged) salinity over the sills for each period. The wide south-going arrow at depth for each period shows the total south-going volume transport just south of the northern sill (along-strait distance ≈ 10 km). Vertical arrows show average freshwater supply to the estuary for each period, including river and hydropower supply (constant) as well as precipitation (variable). The values for <S > are the salinities averaged over the whole strait for each period. Brown boxes show the salinity, S_A, for the Atlantic water at depth north of the northern sill. Differences of the frequency of density inversions over the slope south of the northern sill (white arrows) are based on Fig. 11. Note that the transport values are based on averages for each period with sea level kept constant, which explains why they do not balance.

The background colours in Fig. 12 indicate net (i.e., period-wise averaged) flow through the strait. The red areas in Fig. 12a show that the upper layers have a net northward flow during Period 1. On an hourly time scale, water flows back and forth across the sills, but on average, there is a net flow from the region south of the southern sill, through the strait, and out across the northern sill. The total volume of water carried through the strait by this net flow during the 188 hours of Period 1 is slightly more than the volume of the strait. Based on this, the flushing time for the whole strait during Period 1 is 7.6 days.

During Period 2, the net flow is quite different. Now, the blue colour in Fig. 12b indicates net southward flow through almost the entire strait. Only a small near-surface region close to the northern sill has net northward flow. Even though Period 2 (158 hours) is shorter than Period 1 (188 hours), the net amount of water flowing through the strait is somewhat higher and the flushing time for the whole strait is only 5.5 days during Period 2.

The most pronounced difference between the two periods lies in the net inflow from the north and its passage through the deep parts of the strait. The net southward flow of seawater across the northern sill along the bottom was more than ten times higher during Period 2 (558 $m^3 s^{-1}$) than Period 1 (47 $m^3 s^{-1}$) and it was less diluted by the fresher waters on top. This is seen by comparing the transport-averaged salinity of the southward inflow (values in arrows) with the salinity S_A of the "pure" Atlantic water found at depth north of the strait (values in brown boxes).

After passing over the northern sill, the dense seawater from the north tends to stay close to the bottom as it flows over the southern slope of the sill (Fig. 11d). This is the case during both periods, but more so during Period 1 (Fig. 8). During this descent, the seawater entrains and is diluted by water already in the strait. Thus, the 47 $m^3 s^{-1}$ that crossed the sill during Period 1 increased to 233 $m^3 s^{-1}$ at depth (Fig. 12a).

For Period 2, the deep arrow in Fig. 12b (showing 629 $m^3 s^{-1}$) represents net southward flow through the whole water column just south of the northern sill, but most of that is below sill level of the northern sill. This is evident from Fig. 9, which also illustrates that the volume transport below sill level of the northern sill and hence flushing rates of deep areas was two to three times higher during Period 2 than Period 1.

During Period 2, the seawater from the north seems to experience a higher frequency of density inversions (Fig. 11c) and to be more spread out through the water column (Fig. 8) than during Period 1. This might indicate different mixing regimes during the two periods but the model is hydrostatic and was not set up for detailed mixing studies. Thus, the simulations do not allow definite conclusions on this question.

According to the simulations, the strait, thus, switches between periods (such as Period 1) of a fjord-like behaviour with a two-layer, estuarine-type, circulation system and more strait-like periods (such as Period 2) with uni-directional (southward) flow at all depths except for a small area over and close to the northern sill. These periods, which typically last a week each, are generated by the long-period tidal constituents of sea level variation and analyses of tide gauge data from Tórshavn and Eiði verify that they are real and not model artefacts (Fig. 10). Apparently, the variations are stronger in the model simulations than in nature, but this is difficult to assess on the basis of the available data since Tórshavn is located rather far south of the strait and large spatial changes are to be expected in an amphidromic region.

These features result from a combination of topographic, freshwater input, and tidal characteristics that seem to be rather unique for this strait. We have not been able to find any other region in the literature with a similar behaviour, but the signs may be rather subtle and in our case they would not have been identified without the help of the high-resolution model. Thus, there may be other areas with similar behaviour that has been overlooked.

5 Conclusions and recommendations

Although open in both ends – and thus by definition a strait – the water body treated in this study in many ways behaves like a fjord. Except for its southernmost parts, the strait is normally stratified with a surface layer that has reduced salinities from the large amount of freshwater entering as runoff. The stratified region includes the waters over the northern sill where brackish water flows out of the strait, mainly in the surface layer, while saline seawater flows in, mainly at depth. The southern sill is much narrower and shallower than the northern sill. This causes high velocities and vertical mixing to be generated over the southern sill by the strong tidal forcing. According to the simulations, the work done by the associated friction typically removes half the potential energy generated by the forcing and limits the amount of water passing southwards out of the strait. Thus, most of the water entering the strait across the northern sill during the rising tide also leaves the strait across the northern sill during the ebbing tide rather than passing through the strait.

The tidal forcing is dominated by semidiurnal sea level variations that are much stronger north of the strait than south of it due to the proximity of an amphidromic region. These variations control the flows within and through the strait on time scales up to a day, but the tidal forcing also includes variations with fortnightly and monthly periods, which generate slow variations in the flow field. According to the simulations, these long-term flow variations also induce variations in the hydrographic structure so that the strait switches between periods of a more strait-like and a more fjord-like character with each period typically lasting one week. Associated with these switches there are pronounced changes in the flow between the strait and the area south of it. Also the flushing rate of the deep water in the strait is affected by these switches and they need to be taken into account for the management of aquacultural and other activities. Analyses of tide gauge measurements off both ends of the strait verify that these long-term variations in tidal forcing are real and not model artefacts. There are, however, indications that they may be enhanced in the model simulations and it is recommended that a new simulation is implemented together with a more targeted field experiment to provide a better foundation for evaluating the rather unique behaviour of this strait.

Code availability. The source code of ROMS is available from ROMS, http://myroms.org.

Data availability. Landsverk data of sea level are available upon request (www.landsverk.fo). Data from DMI surface air pressure and precipitation are available upon request (www.dmi.dk). Current measurements and CTD observations are available upon request from SVE. The data from local energy supplier (SEV) are available upon request (www.sev.fo). The model output from the FC32m model are available from SVE upon request.

Author contributions. SVE, JA and KS conceptualized the model study, JA set up the model and ran the model. SVE performed data analysis on model data, EO performed analysis on observations. KS, EK and BH provided supervision and guidance. SVE and BH wrote the manuscript with input from all the authors.

Competing interests. The authors declare that they have no conflict of interest.

Acknowledgements. Thanks to Lars Asplin, Institute of Marine Research, Norway, for providing the network and for the general introduction to ROMS. This paper is part of the PhD project by SVE with EK as main supervisor. The PhD project is financially supported by Statoil Faroes, Mowi Faroe Islands, P/F Bakkafrost and the Faroese Research Council (Grant no. 0445). We thank Manuel Diez-Minguito and two anonymous referees for very helpful comments.

References

Davidsen, E., Førland, E., and Madsen, H.: Orographically enhanced precipitation on the Faroe Islands, in: Nordic Hydrological Conference 1994, edited by Kern-Hansen, C., Rosbjerg, D., and Thomsen, R., no. 34 in Nordic Hydrological Program (NHP) Report, pp. 229–239, Nordic Association for Hydrology, Tórshavn, Faroe Islands, 1994.

Erenbjerg, S. V., Albretsen, J., Simonsen, K., Sandvik, A. D., and Kaas, E.: A step towards high resolution modeling of the central Faroe shelf circulation by FarCoast800, Regional Studies in Marine Science, 40, 101 475, https://doi.org/https://doi.org/10.1016/j.rsma.2020.101475, 2020.

Erenbjerg, S. V.: Avfall í Sundalagnum og hjáliggandi firðum, metingar og mátingar; Input til ROMS fresh water forcing, in: Fiskaaling rit, Technical Report, 02, pp. 1–10, Fiskaaling P/F, Við Áir, Faroe Islands, 2020.

Haidvogel, D., Arango, H., Budgell, W., Cornuelle, B., Curchitser, E., Lorenzo, E., Fennel, K., Geyer, W., Hermann, A., Lanerolle, L., Levin, J., McWilliams, J., Miller, A., Moore, A., Powell, T., Shchepetkin, A., Sherwood, C., Signell, R., Warner, J., and Wilkin, J.: Ocean forecasting in terrain-following coordinates: Formulation and skill assessment of the Regional Ocean Modeling System, Journal of Computational Physics, 227, 3595–3624, https://doi.org/10.1016/j.jcp.2007.06.016, 2008.

Hansen, B.: Sea Level Variations and currents on the Faroe Plateau and their relation to the hydrography, Ph.D. thesis, University of Copenhagen, Institute of physical Oceanography/University of Faroe Islands, 1978.

Hansen, B.: Oxygentrot og útskifting í botnvatninum á føroyskum gáttarfirðum, Fiskirannsóknir, 6, 188–258, Fiskirannsoknir_6.pdf (hav.fo), 1990.

Kragesteen, T. J., Simonsen, K., Visser, A. W., and Andersen, K. H.: Identifying salmon lice transmission characteristics between Faroese salmon farms, Aquaculture Environment Interactions, 10, 49–, https://doi.org/10.3354/aei00252, 2018.

Larsen, K. M. H., Mortensen, E., Øystein Patursson, and Simonsen, K.: Current measurements in the ASAF project, Deployment SUNB1212, ASAF Technical Report 14-02, 22 pp., Havstovan/Fiskaaling P/F, Tórshavn, Faroe Islands, 2014a.

Larsen, K. M. H., Mortensen, E., Øystein Patursson, and Simonsen, K.: Current measurements in the ASAF project, Deployment SUNC1212, ASAF Technical Report 14-03, 22 pp., Havstovan/Fiskaaling P/F, Tórshavn, Faroe Islands, 2014b.

Li, Y., Wolanski, E., and Zhang, H.: What processes control the net currents through shallow straits? A review with application to the Bohai Strait, China, Estuarine, Coastal and Shelf Science, 158, 1–11, https://doi.org/10.1016/j.ecss.2015.03.013, 2015.

Lien, V., Gusdal, Y., Albretsen, J., Melsom, A., and Vikebø, F.: Evaluation of a Nordic Seas 4 km numerical ocean model archive, Fisken og Havet, 7, 7:79, 2013.

Myksvoll, M., Sandvik, A., Skarðhamar, J., and Sundby, S.: Importance of high resolution wind forcing on eddy activity and particle dispersion in a Norwegian fjord, Estuarine, Coastal and Shelf Science,, 113, 293–304, https://doi.org/https://doi.org/10.1016/j.ecss.2012.08.019, 2012.

Pawlowicz, R., Beardsley, B., and Lentz, S.: Classical tidal harmonic analysis including error estimates in MATLAB using T_TIDE, Computers & Geosciences, 28(8), 929–937, https://doi.org/10.1016/S0098-3004(02)00013-4, 2002.

Pyper, B. J. and Peterman, R. M.: Comparison of methods to account for autocorrelation in correlation analyses of fish data, Canadian Journal of Fisheries and Aquatic Sciences, 55, 2127–2140, https://doi.org/10.1139/f98-104, 1998.

Rasmussen, T., Olsen, S. M., Hansen, B., Hátún, H., and Larsen, K. M.: The Faroe shelf circulation and its potential impact on the primary production, Continental Shelf Research, 88, 171 – 184, https://doi.org/10.1016/j.csr.2014.07.014, 2014.

Shchepetkin, A. F. and McWilliams, J. C.: The regional oceanic modeling system (ROMS): A split-explicit, free-surface, topographyfollowing-coordinate oceanic model, Ocean Modelling, 9, 347 – 404, https://doi.org/10.1016/j.ocemod.2004.08.002, 2005.

Simonsen, K.: The Tides on the Faroe 420 Shelf and an Attempt to Simulate the M_2-Tide in the Area, Master's thesis, Geophysical Institute, University of Bergen, 1992.

Simonsen, K. and Niclasen, B.: Analysis of the energy potential of tidal streams on the Faroe Shelf, Renewable Energy, 163, 834–844, https://doi.org/https://doi.org/10.1016/j.renene.2020.08.123, 2021.

Simonsen, K., Joensen, E., and Erenbjerg, S.: Sundalagið - Samandráttur av hydrografiskum mátingum árini 2013-2017, in: Fiskaaling rit, Technical Report, 01, pp. 1–50, Fiskaaling P/F, Tórshavn, Faroe Islands, 2018.

VandKvalitetsInstitutet: Biologiske effekter af vandkraft ved Vestmanna og Eiði Færøerne, in: Rapport til Overfredningsnævnet på Færøerne, Technical Report, pp. 1–22, VKI, Tórshavn, Faroe Islands, 1983.

Supplement for Paper II

Erenbjerg, S. V., Albretsen, J., Simonsen, K., Olsen, E., Kaas, E., & Hansen, B. (2021). A tidally driven estuary close to an amphidromy. Ocean Sci. Discuss., 2021, 1-23. https://doi.org/10.5194/os-2021-23

Supplementary figures

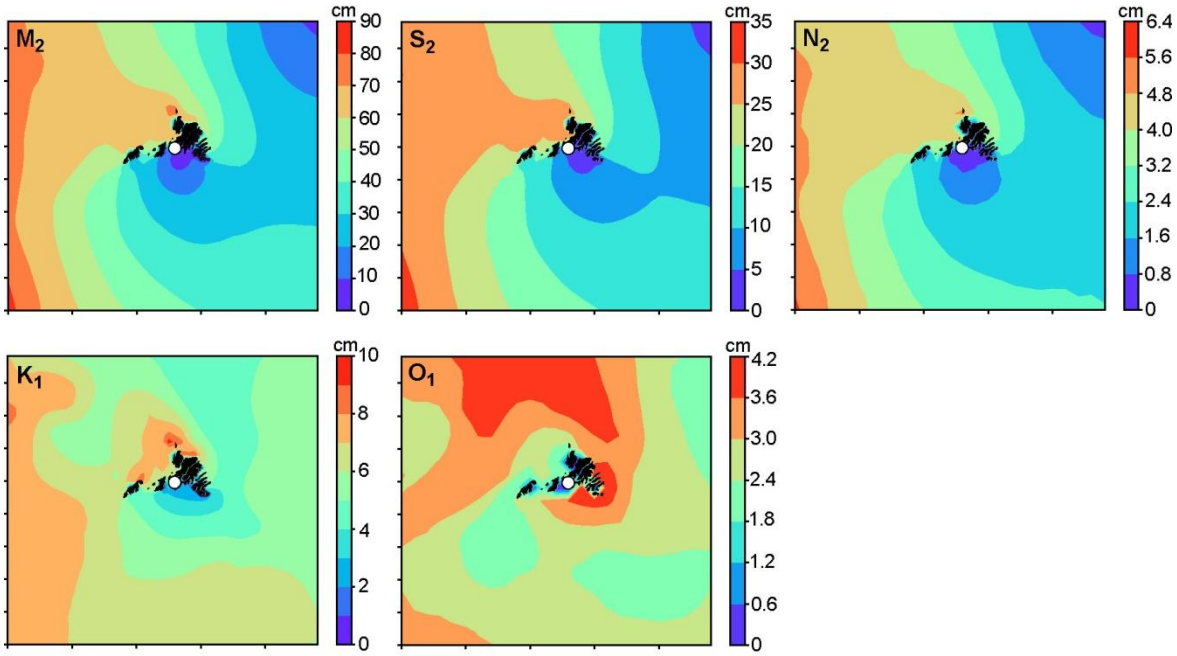

Figure S1. Amplitudes (in cm) of the three dominant semidiurnal and two dominant diurnal tidal constituents of sea level around the Faroes based on the 800 m parent model. The white circle indicates the area close to Tórshavn.

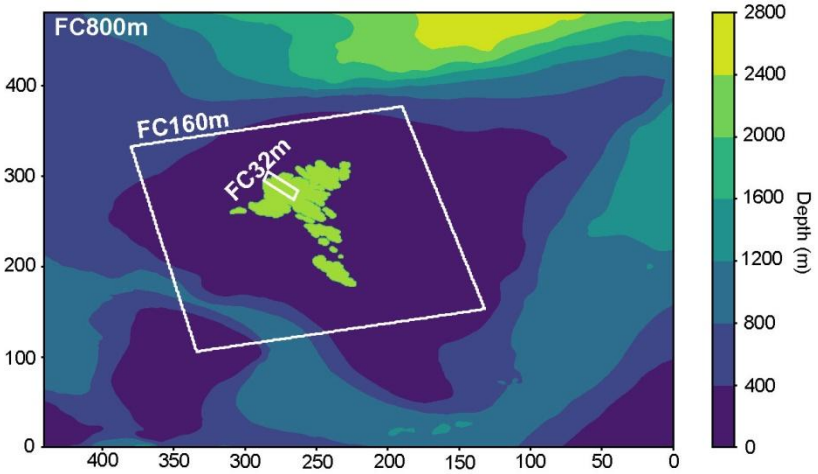

Figure S2. The model used in this study, FC32m, is nested within the FC160m model, which is nested within the FC800m model. The FC800m model is forced along its four open boundaries by the SVIM hindcast archive (4x4 km horizontal resolution, Lien et al., 2013).

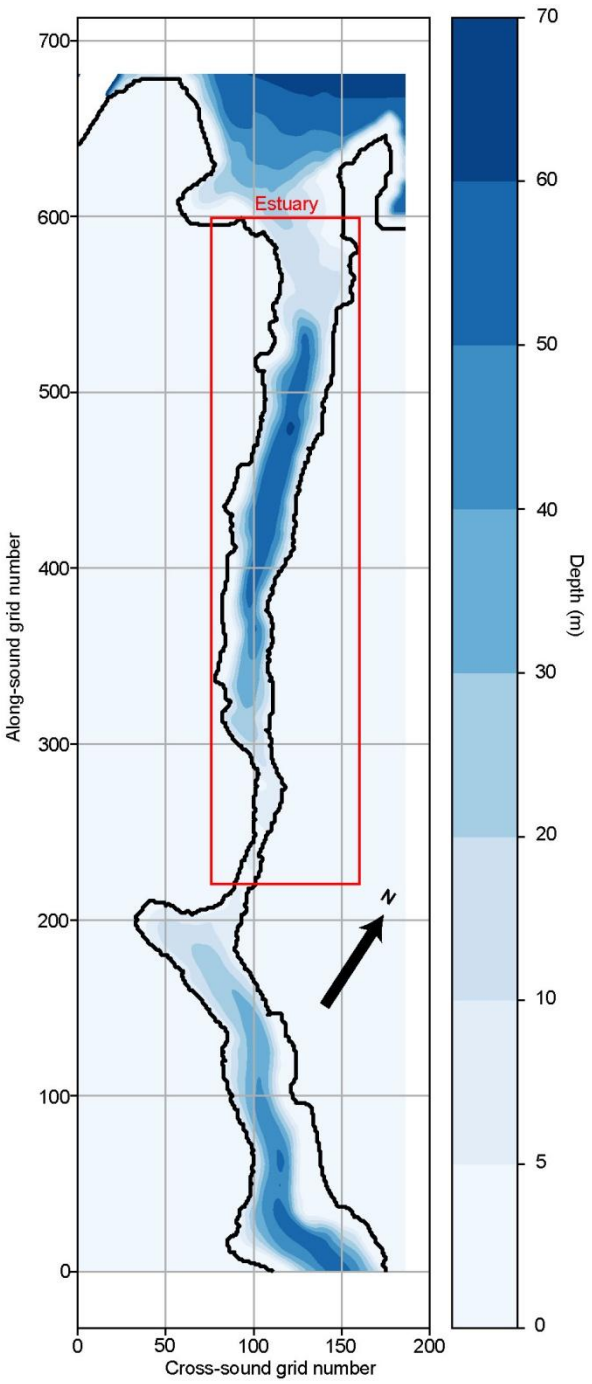

Figure S3. Model domain and bottom topography. The red rectangle labeled “Strait” defines the part of the model domain that is discussed in this study.

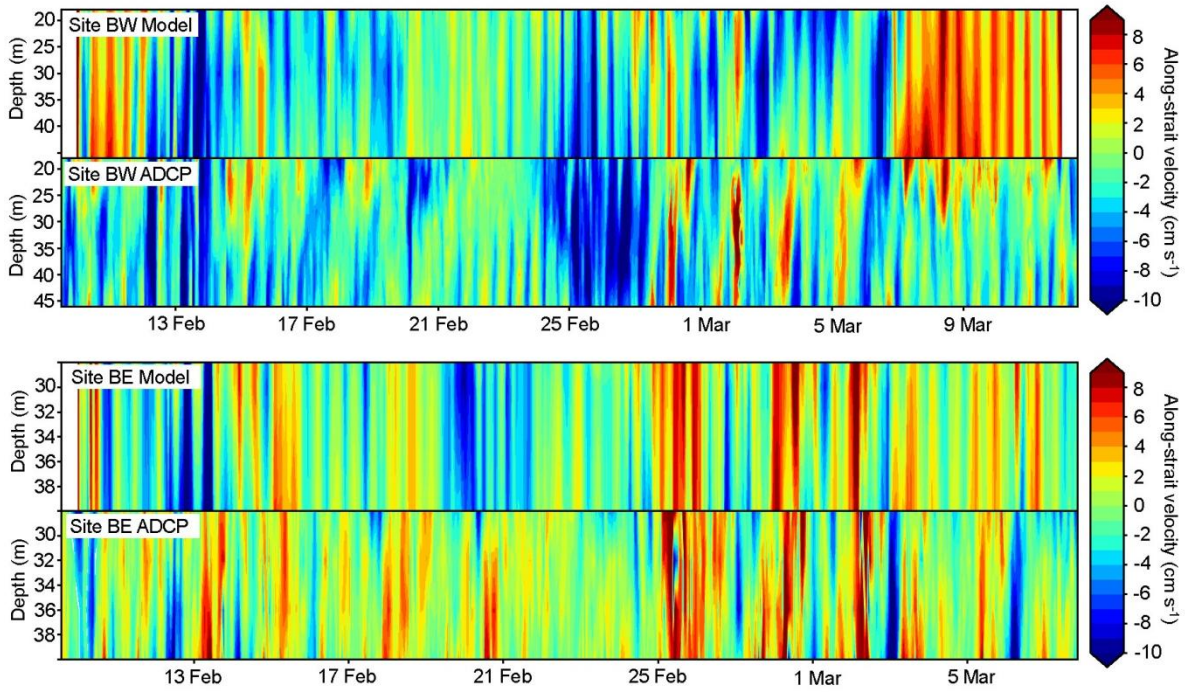

Figure S4. Hovmøller diagrams of along-strait velocities at the two ADCP mooring sites comparing observed (ADCP) and simulated (Model) velocity profiles for the depth intervals with acceptable ADCP data.

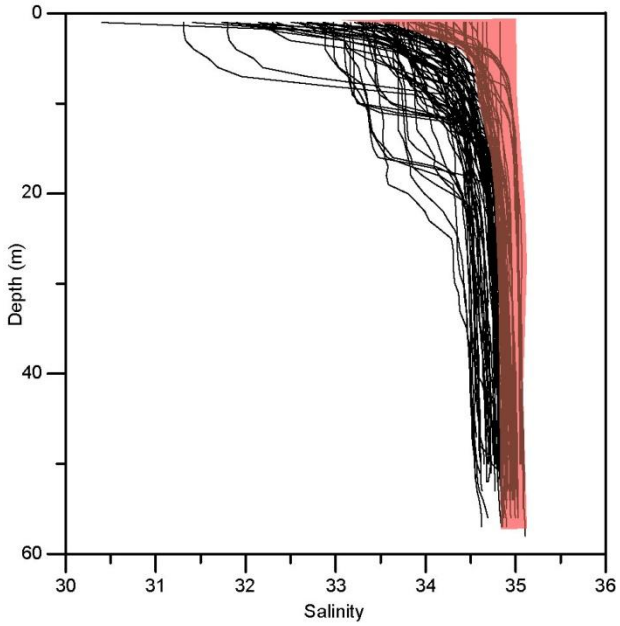

Figure S5. Comparison of salinity profiles from observations and model. The black lines show observed salinity profiles from 92 individual CTD casts at stations with bottom depth at least 50 m in winter (November – April). The semi-transparent red area in front is the simulated salinity range (minimum to maximum at each depth) of daily averaged salinity profiles for all grid cells in the model with a bottom depth of at least 50 m.

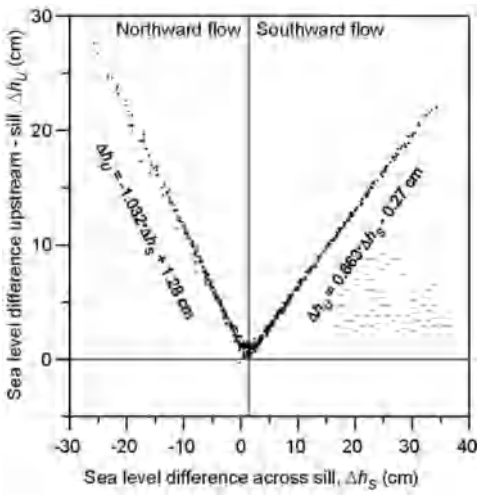

Figure S6. The sea level difference between the sill and the region upstream of it, Δh_U, plotted against the sea level difference, Δh_S, across the whole sill (Fig. 4a in main manuscript). Each point represents one hour and the regression equations are derived for each flow direction separately.

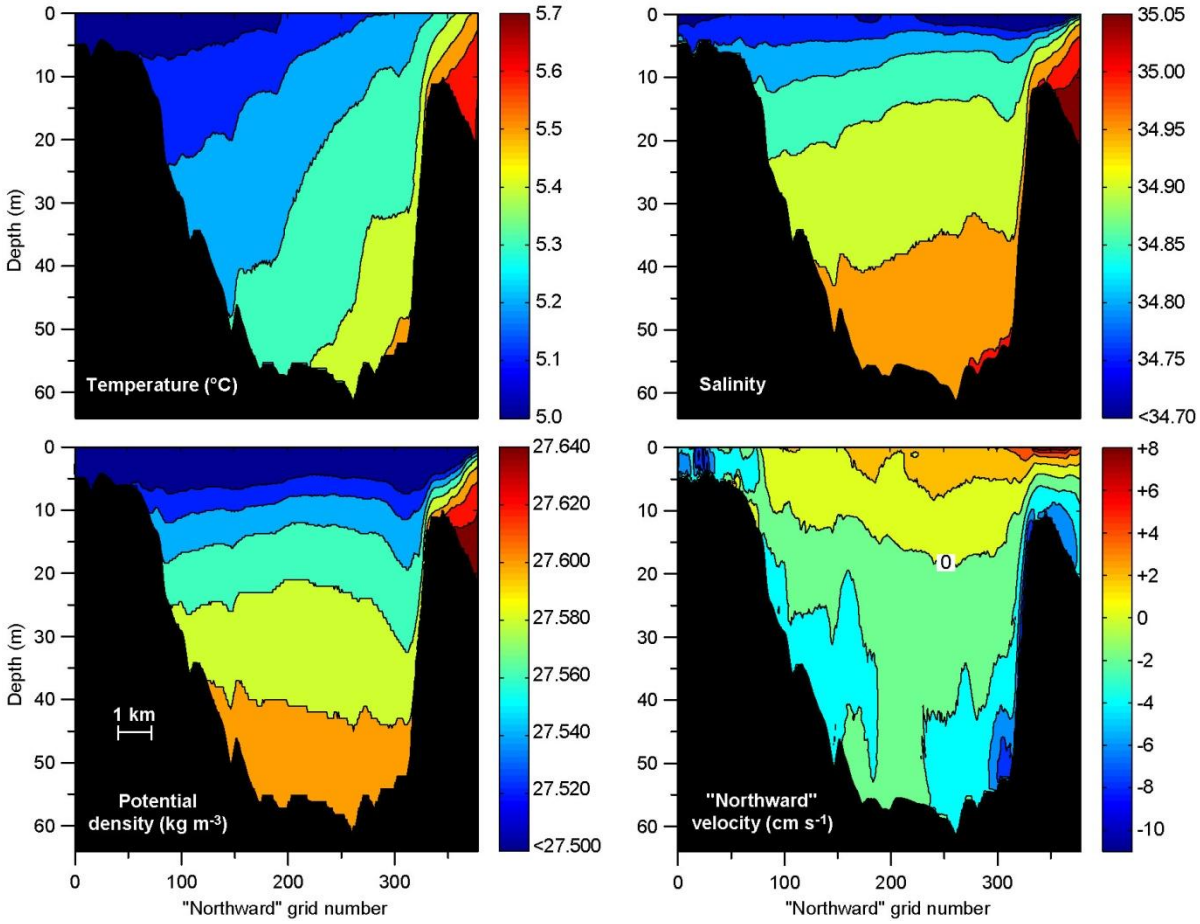

Figure S7. Cross-strait averaged temperature, salinity, potential density, and northward velocity plotted against northward grid number averaged over the whole simulation period. For salinity and potential density, the lowest values are grouped together. The bottom depth indicated by the black areas is the maximum depth along each section crossing the strait.

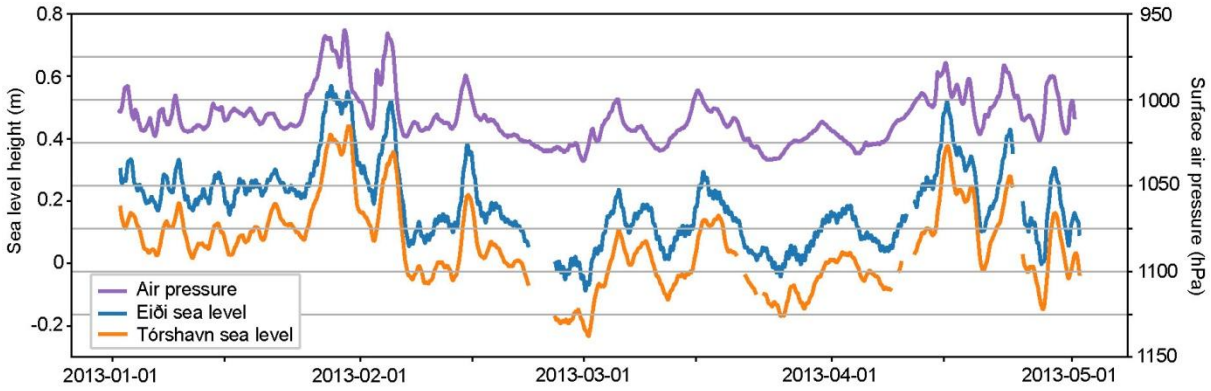

Figure S8. Variation of 25-hour averaged sea level height from Landsverk data from the stations Tórshavn (orange line) and Eiði (blue line) plotted with the Tórshavn surface air pressure provided by the Danish Meteorological Institute (DMI) (purple line) with an inverted y-axis.

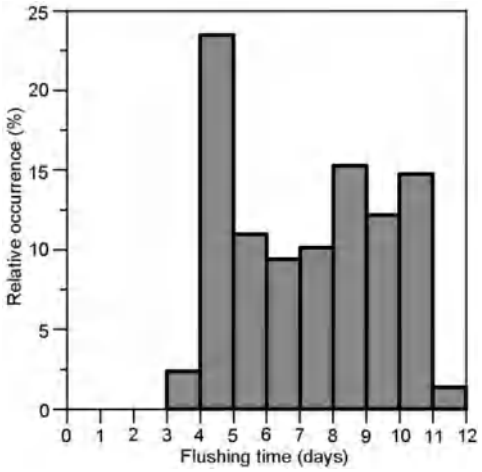

Figure S9. Relative occurrence of flushing times estimated as the number of hours with positive northward volume transport across the northern sill needed to flush out the total volume of the strait. The histogram was generated by starting every hour of the simulation and from that point adding up the outflow for every hour with positive volume transport until the total outflow equaled the volume of the strait.

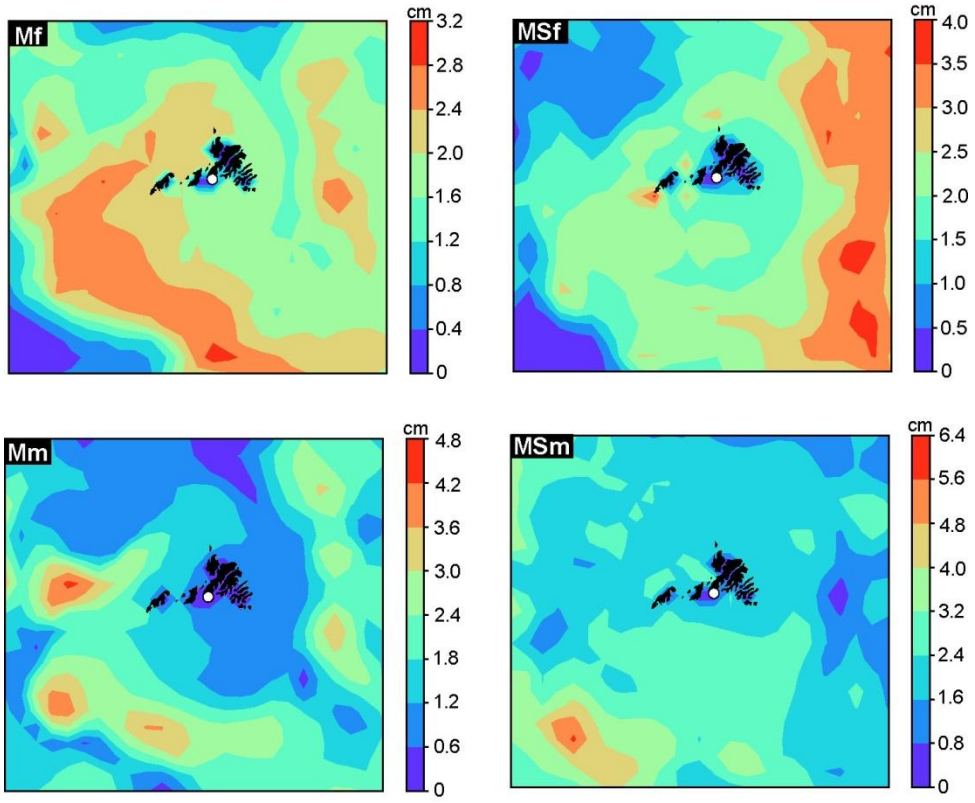

Figure S10. Amplitudes (in cm) of the four dominant long-period tidal constituents of sea level around the Faroes based on the 800 m parent model. The white circle indicates the area close to Tórshavn.

Paper III

Erenbjerg, S. V., Hansen, B. Et al. (2021). The effects of tidal mixing on stratification over the Faroe shelf.

III

The effects of tidal mixing on stratification over the Faroe shelf

Sissal V. Erenbjerg, Bogi Hansen and other authors

Abstract
To be completed

1 Introduction

Background on the Faroe shelf and its primary production, including importance for higher trophic levels and commercial fish stocks. The importance of stratification for primary production and background on the effect of tidal mixing on stratification. Objectives of the study and how to fulfill them.

2 The ROMS FC800m model

The ROMS model setup applying 800 m × 800 m horizontal resolution around the Faroe shelf, hereafter named FC800m, was originally adapted from the Norwegian Coastal model, NorKyst800 applying the same resolution. Our version covers the entire Faroe Shelf and the Faroe Bank to the west of the Faroe Islands and extends into the deep water surrounding the area to the east, north and west, and the Scottish shelf to the south.

FC800m is implemented using ROMS as the hydrodynamic model (e.g. Shchepetkin and McWilliams (2005) and Haidvogel et al. (2008). ROMS is a state-of-the-art, three-dimensional, free-surface, primitive equation numerical ocean model using a generalized terrain-following s-coordinate in the vertical. The FC800m model applies 35 vertical levels and was set up with enhanced resolution in the upper ~50 m. Lateral boundary conditions and initial fields conditions are retrieved from the Nordic Seas 4 km numerical ocean model hindcast archive (ROMS4KM) updated from Lien et al. (2013). The tidal forcing was applied along the open boundaries and interpolated from the global TPXO7.2 (Egbert and Erofeeva, 2002). The atmospheric forcing was obtained from simulations with the Weather Research and Forecasting (WRF) model (WRF, http: //www.wrf-model.org/).

The simulation was initialized January 1st, 2013 from the ROMS4KM state and was run for one year until December 31st, 2013. More details on the model and its validation are presented in Erenbjerg et al. (2020).

3 Observational material and methods

3.1 CTD standard stations

We will use CTD observations from six of the regularly monitored standard stations, which are located on the shallow parts of the shelf (Table 3.1 and Figure 3.1).

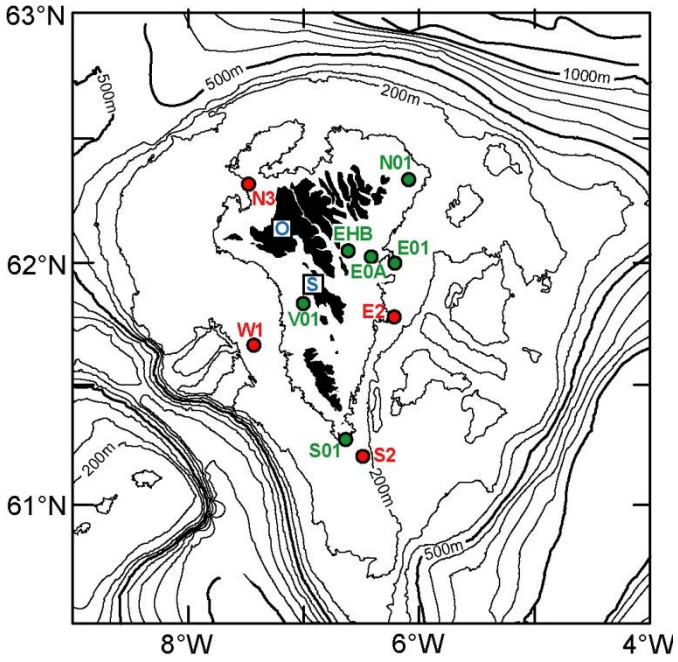

Figure 3.1. *Locations of four current meter deployment sites (red circles) and six CTD standard stations. The blue letters "O" and "S" indicate two coastal monitoring sites "Oyrargjógv" and "Skopun", respectively.*

Table 3.1. *Depth to bottom, reference depth, and number of CTD profiles for the six standard stations considered.*

Site:	V01	N01	S01	EHB	E0A	E01
Depth (m):	80	80	100	60	80	125
D_{Ref}(m):	50	50	50	40	50	50
Number:	153	148	92	80	19	105

3.2 Tidal speed cubed

Because of its importance for tidal mixing, we are mainly interested in tidal speed cubed (Simpson and Sharples, 2012). We have therefore generated one time series, which is based on tidal prediction from harmonic analyses of current measurements at three sites (Table 3.2 and Figure 3.1).

Table 3.2. *Characteristics of the three current meter deployments, on which the predictions are based. "Site" refers to Figure 3.1, "Bt.d" is the bottom depth (in m), "Min" is the interval between measurements (in minutes). The three last columns list average values for tidal current speed, $\langle U \rangle$ (in m s^{-1}), speed squared, $\langle U^2 \rangle$ (in m^2 s^{-2}), and speed cubed, $\langle U^3 \rangle$ (in m^3 s^{-3}). All the current meters were at 40 m depth.*

Series	Site	Lat	Lon	Bt.d	Deployment period	Min	Days	$\langle U \rangle$	$\langle U^2 \rangle$	$\langle U^3 \rangle$
2985_010	N3	62°19'	7°29'	98	19791002-19800519	60	230	0.565	0.378	0.289
2985_012	W1	61°40'	7°26'	145	19810303-19810926	30	207	0.270	0.082	0.027
6486_001	E2	61°47′	6°13	116	19820915-19830416	30	213	0.295	0.105	0.044

Each of the three prediction series contains hourly values for tidal current speed (and direction) for the period 1960-2020. From these series, three new series with daily values are generated by averaging the

tidal speed cubed for every hour over each day. Correlations between the series at the different sites (Table 3.3) document that sites N3 and E2 have very similar variations of the tidal speed. Site W1 is more different, but still fairly similar to the other two sites.

Table 3.3. *Correlation coefficients between daily averaged tidal speed to the first, second, and third power at the three measurement sites for the sixty years of the prediction period.*

Tidal speed			Tidal speed squared			Tidal speed cubed		
N3-W1	N3-E2	W1-E2	N3-W1	N3-E2	W1-E2	N3-W1	N3-E2	W1-E2
0.973***	0.991***	0.970***	0.963***	0.993***	0.968***	0.949***	0.993***	0.960***

As seen in Table 3.2, the three sites have different average tidal speeds (partly due to different bottom depths, perhaps) and they are even more different when cubed (last column in the table). To generate a composite time series, $U^3(t)$, that can represent the northern part of the inner Faroe shelf, the three prediction time series are therefore normalized before they are combined:

$$U^3(t) = \tfrac{1}{3} \cdot \left\{ \frac{U_1^3(t)}{\langle U_1^3 \rangle} + \frac{U_2^3(t)}{\langle U_2^3 \rangle} + \frac{U_3^3(t)}{\langle U_3^3 \rangle} \right\} \qquad (3.1)$$

where the index refers to the measurement site and <> indicates temporal averaging. In principle, this series may be generated for the whole sixty years of the prediction period, but we will only use the period from 1 January 1979 to 31 July 2017, for which we also have daily values for PAR and heat flux. Daily values of this series are plotted against the day number in the left panel of Figure 3.2 and they show strong indications of pronounced equinox tides.

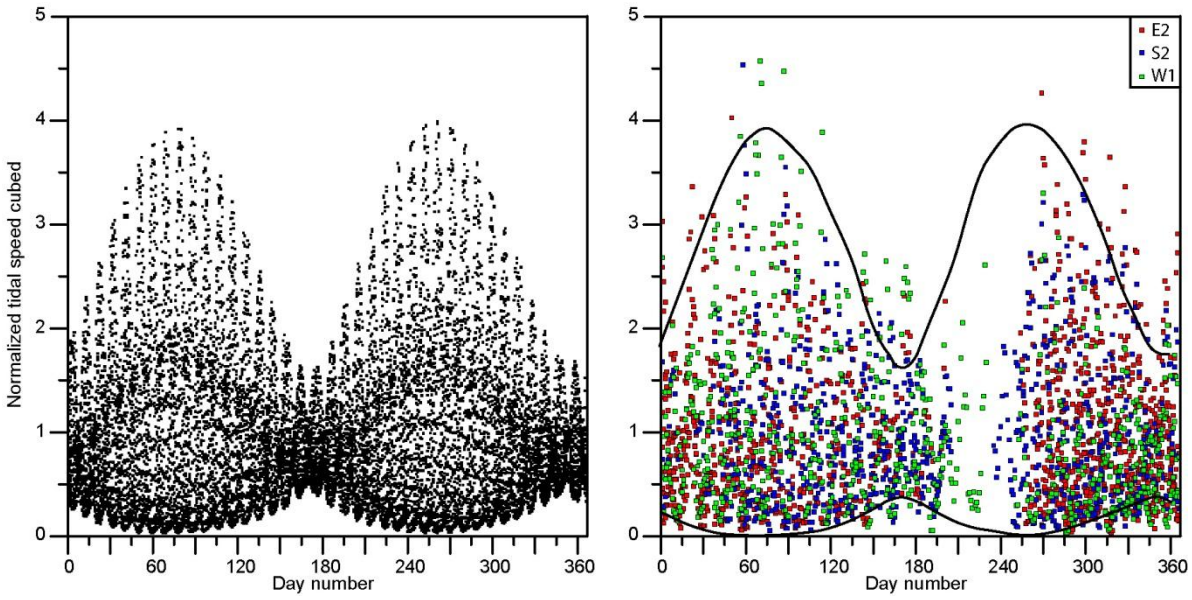

Figure 3.2. *The variation of tidal speed cubed through the year. Each square represents one-day average of tidal speed cubed normalized by the long-term average of tidal speed cubed for each series.* ***Left panel:*** *Composite time series based on predictions from three sites, Eq. (3.1).* ***Right panel:*** *Results based on measurements at three different sites, as described in the text. The black curves on the right panel are the envelopes of the squares on the left panel.*

Seeing such a strong signal as evidenced in the left panel of Figure 3.2, one may ask whether this perhaps to some extent could be due to an artifact of the prediction system. To check this, we have analyzed more closely a total of 24 current meter records from three different sites (E2, S2, and W1) from 1978 to 1988, covering a total of 3015 days with measurements of current speed and direction at hourly or semi-hourly intervals.

For each of the three sites, we generated a time series with hourly values for eastward and northward velocity components. For each day with complete measurements, the residual current was determined as the average of the 24 hourly current vectors and this residual current was then subtracted from the hourly values to give an approximate representation of the tidal current for every hour. The magnitude of this current was cubed for every hour and averaged over each day to get a time series of daily values, which were then normalized by dividing with the overall average for each of the three sites separately.

The tidal speeds determined in this way cannot be expected to give very accurate representations of the "real" tidal current, generated by the tidal forces from the moon and the sun, since any current variation generated by other forcing mechanisms on daily or shorter periods will be included. Nevertheless, the overall picture (right panel of Figure 3.2) does fit the seasonal variation of the composite series (left panel) fairly well.

From the left panel of Figure 3.2, one gets the impression that the most frequent values for the tidal speed cubed are around 0.5 and this is verified by the histogram in Figure 3.3.

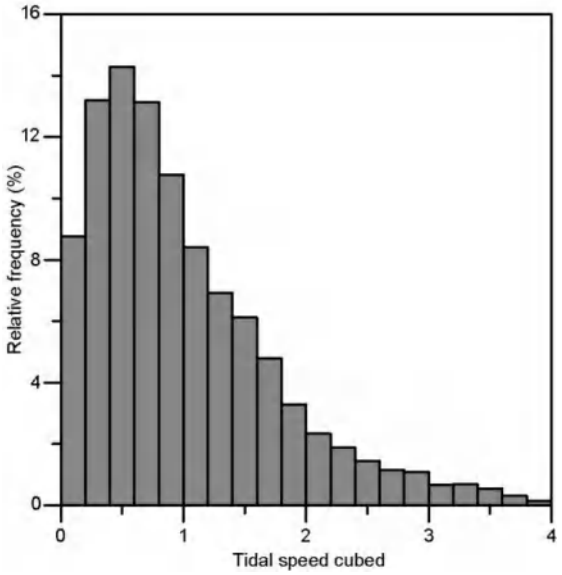

Figure 3.3. *Frequency distribution (histogram) of the tidal speed cubed*

It should be emphasized that from its definition, Eq. (3.1), the tidal speed cubed is dimensionless. It does not represent the absolute magnitude of tidal effects, but rather the temporal variation at each site.

4 Modeling results

4.1 Power spectra of near-surface temperature

To investigate the variations of near-surface temperature, power spectra of the daily averaged temperature at 15 m depth were calculated for all grid points in the model. The 15 m depth was chosen to prevent atmospheric effect to dominate too much. The power spectrum was computed from the one dimensional discrete Fourier Transform with the efficient Fast Fourier Transform (FFT) algorithm. Only the low-frequency part with periods above 8 days is considered.

Many grid points exhibit temperature spectra with clear peaks around two weeks. Such a peak would be expected if the semidiurnal tides affect the temperature since the superposition of the M_2 and the S_2 constituents varies in amplitude over a period of 14.8 days. Where diurnal tides dominate over the semidiurnal, the period should be given by the superposition of the two dominant diurnal constituents K_1 and O_1, which varies over a period of 13.6 days.

Figure 4.1 shows spatial variations of the spectral amplitudes close to these two fortnightly periods and it indicates that the near-surface temperature in some areas is affected by some process, perhaps with different relative contributions of semidiurnal and diurnal signals.

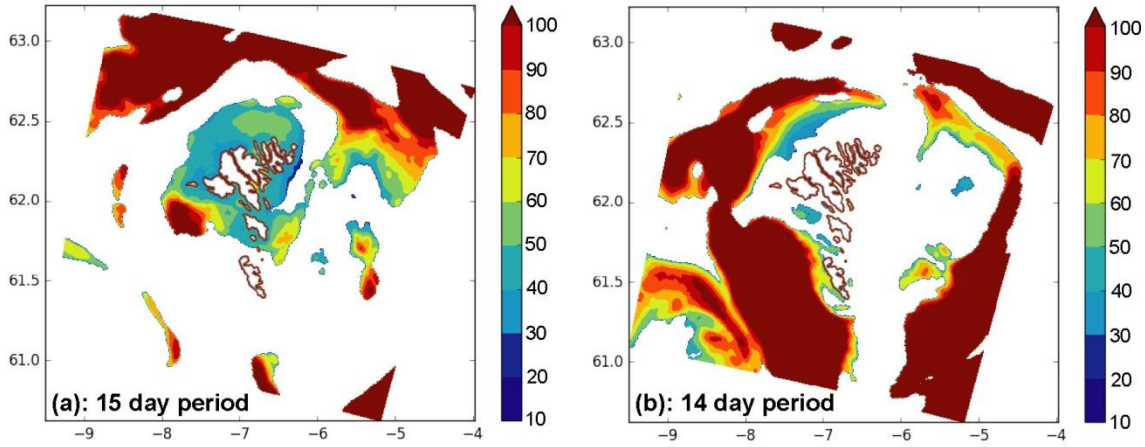

Figure 4.1. *Spatial variation of the amplitudes of spectral peaks with periods of 15* ***(a)*** *and 14* ***(b)*** *days in a relative scale with the strongest signal set to 100. White areas have signal-to-noise ratio less than 3:1 where the noise is estimated as the standard deviation of the signal.*

4.2 Stratification and tidal mixing

The most obvious explanation for a fortnightly variation of near-surface temperature would be tidal mixing acting to reduce the near-surface temperature stratification. Since the effect of tidal mixing usually is parameterized by the current speed cubed, we have correlated a measure for the temperature stratification with this mixing parameter. For stratification, we use the temperature difference, ΔT, between 5 and 50 m depth. For current speed, we use the speed of the barotropic current, $\left|u^3\right|$.

For the further analysis, we have subsampled the model simulations, considering only every 10th grid point in each direction starting at point (100, 100) and only points with bottom depth ≤ 200 m for the January to September period in 2013. Averaged over this period, both ΔT and $\left|u^3\right|$ show systematic spatial variations (Figure 4.2).

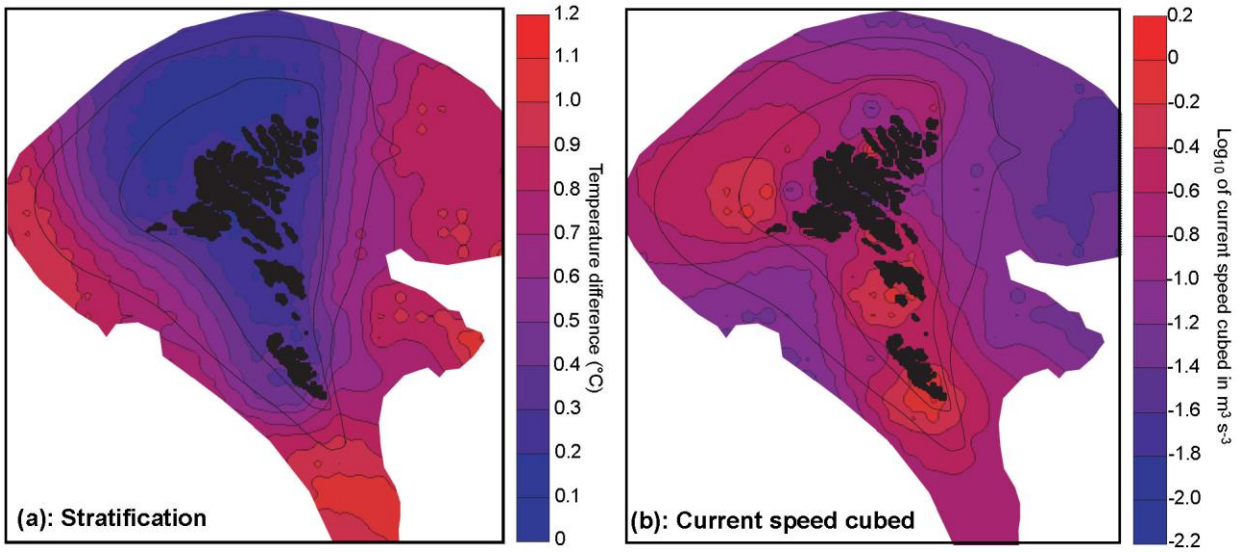

Figure 4.2. (a) *Average (Jan-Sept) stratification defined as temperature difference between 5 m and 50 m depth, ΔT.* ***(b)*** *Logarithm (base 10) of the average (Jan-Sept) current speed cubed. Thin black lines indicate the 100 and 150 m depth contours.*

As expected, the general picture in Figure 4.2 is that ΔT increases with bottom depth whereas $|u^3|$ decreases, but bottom depth only explains a part of the variations for both these parameters. Especially, the region north of the islands is characterized by relatively low average values for ΔT and high values for $|u^3|$.

This may perhaps indicate a negative relationship between ΔT and $|u^3|$. To investigate that further, we correlated daily averaged values of ΔT and $|u^3|$. No effect can be expected if the water is un-stratified initially and there is no heat input. In the correlation analysis, we therefore include only days for which $\Delta T > 0.1$ °C at the start of the day or the daily averaged net heat input from the sun and atmosphere is at least 50 W m^{-2}. In Figure 4.3a, the correlation coefficient for each grid point is plotted against the bottom depth of the grid point, but only for those points where the correlation coefficient was significantly different from zero at the 95% level ($p < 0.05$ after correcting for serial correlation).

In most conditions, tidal mixing should act to reduce stratification and the correlation coefficient should be negative. This is the case for all the points in Figure 4.3a except for a few deep grid points. This is a clear indication that tidal mixing does affect the stratification in the model simulations. Although statistically significant, most of the correlation coefficients in Figure 4.3a are not very high numerically. It has to be taken into account, however, that ΔT is a rough estimate of stratification especially when the shape of the temperature profile may change during the day. Thus, numerically high correlation coefficients should not be expected.

In Figure 4.3a, most of the significant negative correlations are seen for bottom depths between 50 and 120 m bottom depth and Figure 4.3b shows that this occurs for grid points due east of the northernmost islands and especially in the region north of the islands

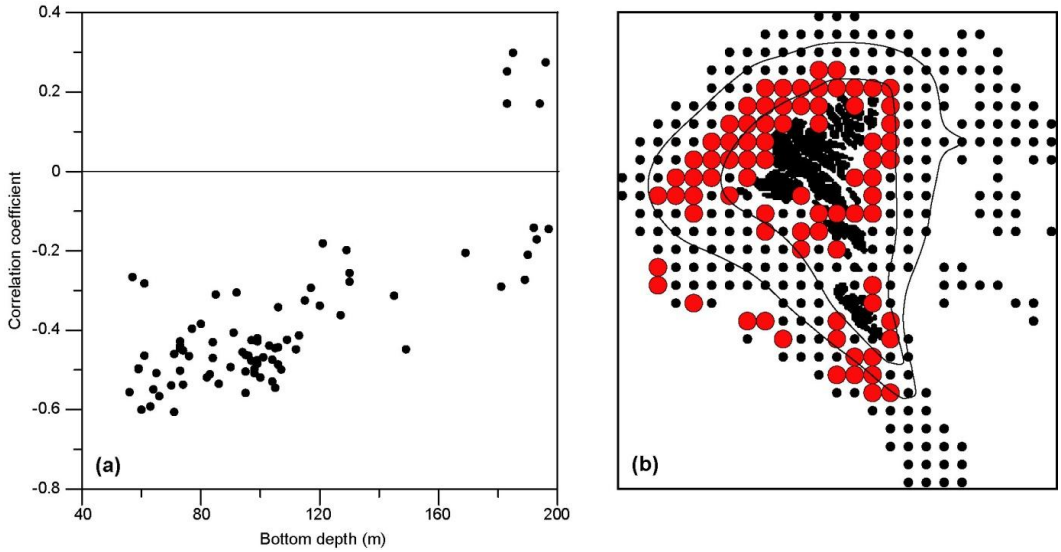

Figure 4.3. (a) *Correlation coefficient between* ***daily averaged*** ΔT *and* $|u3|$ *in each grid point plotted against bottom depth for grid points where the coefficient was significantly different from zero* ($p < 0.05$). ***(b)*** *Black circles show all grid points with bottom depth between 0 and 200 m. Red circles show grid points for which the correlation coefficient in (a) is < -0.1. Only days with initial stratification or positive heat input (see text) are included.*

An alternative way to correlate stratification and tidal mixing is not to use the daily averaged values for ΔT, but rather to use the change in ΔT from one day to the next. This is explored in Figure 4.4. Again, the area north of the islands seems to be most important, but now at larger depths.

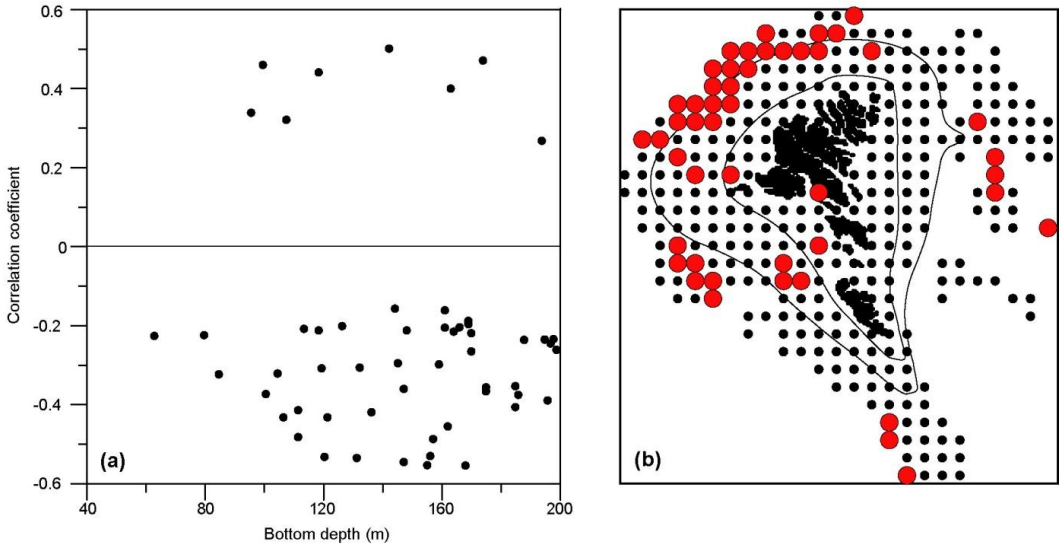

Figure 4.4. (a) *Correlation coefficient between the* ***daily change*** *in* ΔT *and* $|u3|$ *in each grid point plotted against bottom depth for grid points where the coefficient was significantly different from zero* ($p < 0.05$). ***(b)*** *Black circles show all grid points with bottom depth between 0 and 200 m. Red circles show grid points for which the correlation coefficient in (a) is < -0.1. Only days with initial stratification or positive heat input (see text) are included.*

5 Observational results

5.1 Stratification at standard stations

Stratification in a region may be controlled by temperature, by salinity, or by both. To see, which parameter dominates, we have compared the density difference between a reference depth D_{Ref} and the surface from salinity only (i.e. keeping temperature constant) with the density difference from temperature only (i.e. keeping salinity constant). For most of the sites, D_{Ref} was chosen to be 50 m, but for the shallowest site, EHB, it was 40 m in order not to exclude too many occupations that did not reach 50 m.

As seen in Figure 5.1, there was one case (red square in the figure) where salinity dominated and gave rise to a density difference exceeding 0.1 kg m^{-3} and a couple of others (blue squares) where salinity seems to have contributed together with temperature. All the rest of the stratified CTD profiles were primarily stratified by temperature, especially those with large density differences.

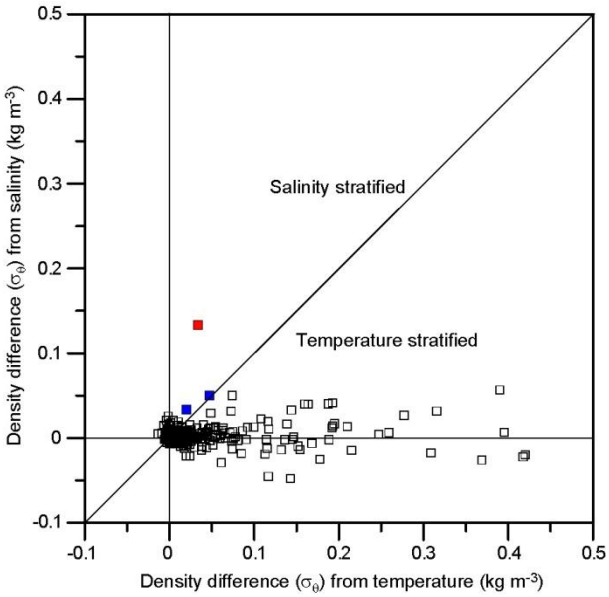

Figure 5.1. *Density differences between D_{Ref} and the surface from salinity plotted against density differences from temperature for all the CTD occupations at the six standard stations in Figure 3.1 (Table S1).*

Thus, the cases of stratification in Figure 5.1 must predominantly be generated by heat transfer from the atmosphere. This is further supported by Figure 5.2a,b where the heat content associated with stratification in the water column is plotted against the heat transferred from the atmosphere (left panels) and against the tidal speed cubed (right panels), both of them averaged over the same day as the CTD profile or the day before, if the profile was measured before noon. Here, the heat content associated with stratification, *H(t)*, is defined as the excess heat content in the water column above D_{Ref} in relation to what it would have been if the temperature was constant from D_{Ref} up to the surface:

$$H(t) = \rho \cdot c \cdot \int_0^{D_{Ref}} \left[T(t,z) - T(t,D_{Ref})\right] dz \qquad (5.1)$$

This parameter, *H(t)*, represents the integrated effect of heat flux over a certain period, which may perhaps be a few hours or many days. Also, both heat flux and tidal speed cubed vary on time scales longer than a day. We should therefore perhaps not expect very strong relationships in Figure 5.2.

Nevertheless, there is a clear indication of a positive relationship between heat flux and *H(t)* for all of the stations.

In the left panels of Figure 5.2a,b, the unit of the abscissa is the same as the unit of the ordinate divided by days, which allows us to estimate the time needed to build up the observed stratification. For V01 and EHB, the typical observed values for *H(t)* are of similar magnitudes as the typical heat gained from the atmosphere during a day (≈ 10 MJ). For these two stations, the typical duration of stratification is therefore only around one day or shorter. For stations E01 and S01, on the other hand, many days of heating from the atmosphere would be needed to build up the observed stratification for the highest values.

This difference between two of the shallowest stations and the two deepest stations is likely due to differences in the intensity of mixing from waves and tidal currents. The effects of tidal mixing are illustrated in the right panels of Figure 5.2a,b, which indicates that stratification for the shallow stations is most likely when the tidal speed cubed is weak. The interpretation of this figure is complicated by the uneven distribution of tidal speed cubed (Figure 3.3) and of the seasonal variations of tidal speed cubed (Figure 3.2) and heat flux, which imply that these two parameters are not independent.

To circumvent this problem, we defined a CTD profile to be stratified if *H(t)* was greater than 5 MJ m^{-2} and plotted tidal speed cubed against heat flux for all the CTD occupations at the six standard stations (Figure 5.3), where the colour of each square indicates whether the occupation was stratified (red square) or not (blue square). For EHB, Figure 5.3 indicates that the station does not become stratified (as defined above) if the tidal speed cubed is 1 or higher. For V01, stratification may occur for somewhat higher values of tidal speed cubed, but not if it reaches 2 or higher and a somewhat similar picture is seen for N01. Recall that the tidal speed cubed only indicates the relative temporal variations at the same site. Since EHB is shallower than the other sites, a value of 1 may well represent much stronger tidal currents for this site than the same value for other sites.

For the deep stations S01 and E01, Figure 5.3 does not indicate any clear dependence of stratification on the tidal current for the same day, consistent with the much longer periods of stratification for these stations.

Author contributions: SVE implemented the model and analyzed its results. BH analyzed the observational results. SVE and BH wrote this version of the manuscript.

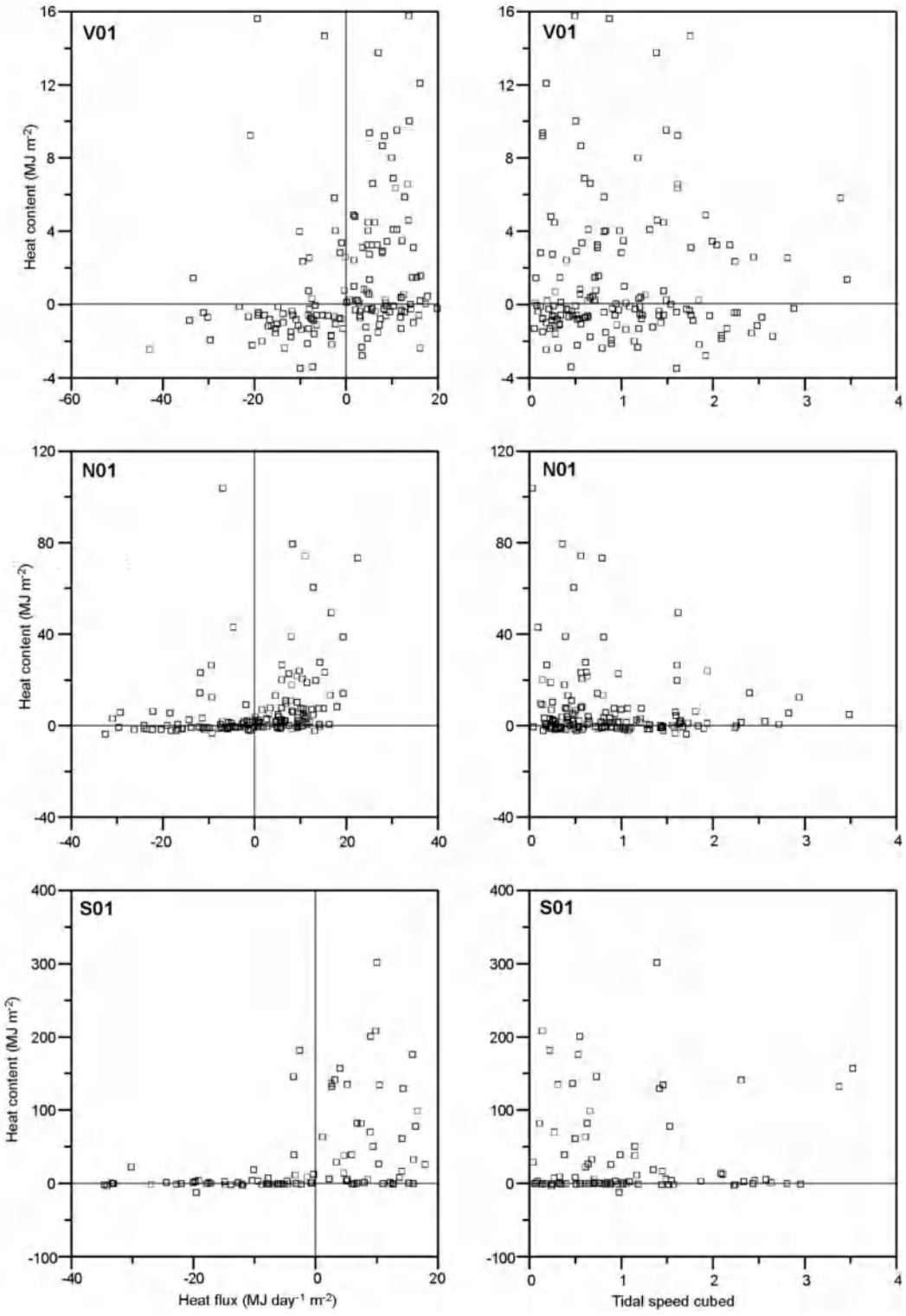

Figure 5.2a. *Heat content above 50 m depth relative to the temperature at that depth, Eq. (5.1), plotted against heat flux (left panels) and tidal speed cubed (right panels) averaged over the same day as the CTD profile or the previous day, if the station was occupied before noon for three standard stations.*

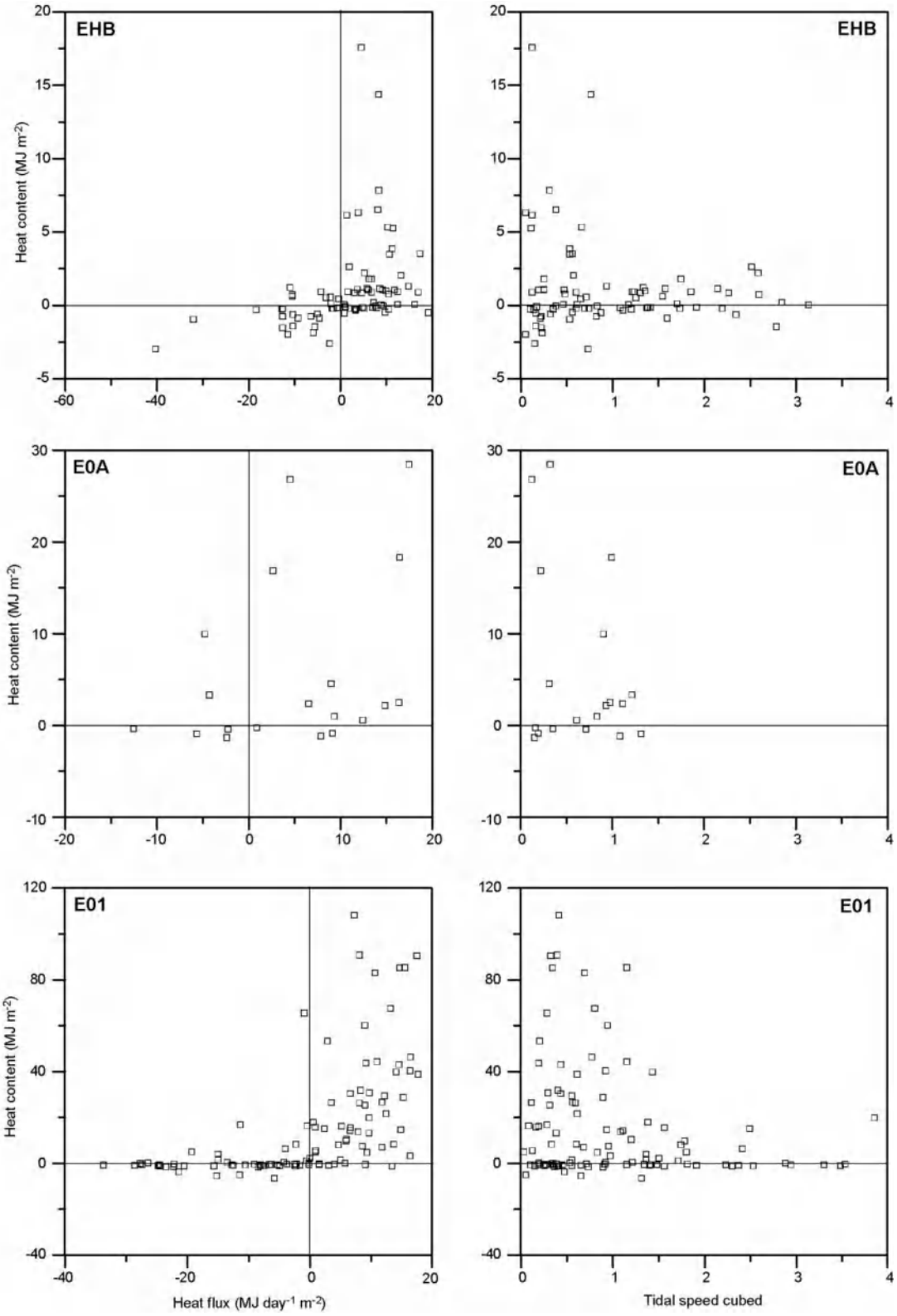

Figure 5.2b. *Heat content above 50 m depth (40 m for EHB) relative to the temperature at that depth, Eq. (5.1), plotted against heat flux (left panels) and tidal speed cubed (right panels) averaged over the same day as the CTD profile or the previous day, if the station was occupied before noon for three standard stations.*

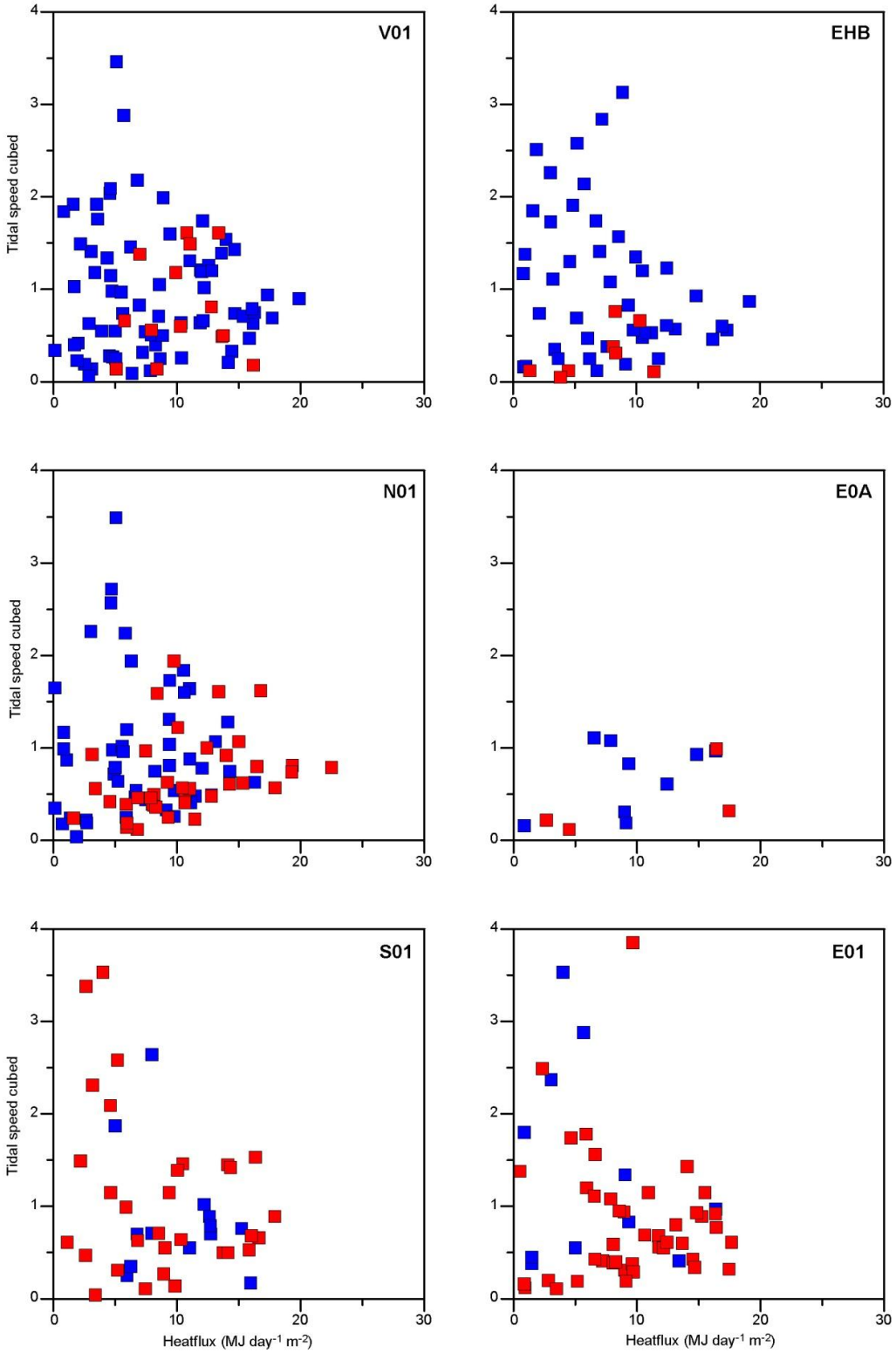

Figure 5.3. *Tidal speed cubed and heat flux for each CTD occupation at the six standard stations with positive heatflux indicated by red squares if H(t) > 5 MJ day^{-1} m^{-2} and blue squares if not. Tidal speed cubed and heat flux are averaged over the same day as the CTD profile or the previous day, if the station was occupied before noon.*